APPLICATION OF DUAL ENERGY TECHNIQUES FOR TISSUE CHARACTERIZATION IN CONVENTIONAL DIAGNOSTIC RADIOLOGY

Tewfik Baba-Hamed

UNIVERSITY COLLEGE LONDON

Submitted for
The Degree of Doctor of Philosophy
The University of London

April 1990

ABSTRACT

The aim of this thesis has been to investigate the use of detectors suitable for single projection dual energy tissue characterization during a single exposure. The advantage of these systems is that the collection and analysis of data are in real time and their size permits their use in conventional fluoroscopic procedures. In the detectors developed in this work energy discrimination was based on two methods, beam filtration (split detector) and pulse height analysis (PHA).

A narrow beam geometry computer model was used to select the optimum combination of detectors and x-ray tube energies for use in dual energy analysis. The thesis describes the construction and experimental evaluation of the optimised dual energy probes. They were used for tissue characterization and it was found that unique values of a particular dual energy coefficient exist up to Z=22 with a precision of 8% for the split detector method, and up to Z=29 with a precision of 3.5% for the semiconductor PHA method independently of patient and tissue thicknesses. The errors associated with the experimental measurements imposed a requirement on the tissue thickness of at least 1 mm for characterization.

The effect of scattered radiation on the dual energy systems was studied theoretically using a Monte Carlo model. The coherent scatter was considered and recent data on molecular atomic form factors for liquid water was used. The results from both the Monte Carlo computer model and the experimental measurements showed that scatter affects the recorded dual energy signal.

The dual energy probes were used for *in vitro* gallstone analysis. It was found that these probes were capable of differentiating between cholesterol and pigment stones, a significant factor in deciding upon the course of treatment for gallstone disease.

CONTENTS

- ABSTRACT 2
- FIGURES 6
- TABLES 8
- ACKNOWLEDGEMENTS 9

CHAPTER 1 INTRODUCTION AND BACKGROUND TO THESIS

- 1.1 INTRODUCTION 10
- 1.2 13
  - 1.2.1 Linear attenuation coefficients and the mixture rule 13
  - 1.2.2 Parametrisation of the linear attenuation coefficient 14
  - 1.2.3 Effective atomic number 18
  - 1.2.4 Effective energy and effective attenuation coefficient 21
- 1.3 DUAL ENERGY TECHNIQUES 23
  - 1.3.1 Dual kVp technique 23
  - 1.3.2 Dual filtering technique 25
  - 1.3.3 Dual detector methods 26
- 1.4 THE DESIGN OF A DUAL ENERGY PROBE 28
- 1.5 DUAL ENERGY ANALYSIS 30
- 1.6 EFFECTS OF BEAM HARDENING 35
  - 1.6.1 Non-linear equations 37
  - 1.6.2 Direct approximation method 37
  - 1.6.3 Subregion direct approximation 38
  - 1.6.4 Iso-transmission line method 39
  - 1.6.5 Iterative procedure for beam hardening correction 40
- 1.7 CLINICAL APPLICATION 45
  - 1.7.1 Gallstone disease 46
  - 1.7.2 Composition and classification of gallstones 46

CHAPTER 2 BASIC DESIGN CONSIDERATIONS AND NARROW BEAM SIMULATION

- 2.1 SPLIT DETECTOR METHOD 50
  - 2.1.1 Narrow beam attenuation computer model 51

2.1.3 Results from the narrow beam attenuation computer model 55
2.1.4 The CsI / Cu / NaI detector system 64
2.2 Pulse Height Analysis Probe 67
2.2.1 Window selection 67
2.3 Determination Of A_1 and A_2 70
2.3.1 Dependence on incident spectra 71
2.3.2 Dependence on material thickness 73
2.3.3 Effect of patient depth 76
2.4 Conclusion 79

Chapter 3 Experimental Results- Split Detector Probe And PHA Probes

3.1 The Split Detector System 81
3.1.1 Introduction 81
3.1.2 Construction of the split detector system 81
3.2 PHA Dual Energy Probe 87
3.2.1 Introduction 87
3.2.2 PHA system performance 87
3.3 The X-ray Tube, Phantoms And Mechanical Accessories 91
3.3.1 Introduction 91
3.3.2 Time variation of the x-ray tube output 91
3.3.3 Phantoms and mechanical accessories 94
3.4 Measurements And Results 97
3.4.1 Introduction 97
3.4.2 Split detector probe 98
3.4.3 PHA dual energy probes 99
3.4.4 Correction of beam hardening using the iterative procedure 100
3.4.5 Results 101
3.4.6 Comparison of the dual energy probes 109

Chapter 4 Effects Of Scatter In A Dual Energy Procedure

4.1 Principles Of Monte Carlo 115
4.1.1 Introduction 115
4.1.2 Random numbers 116
4.1.3 Sampling methods 116

4.2 APPLICATION OF MONTE CARLO TECHNIQUES 119
  4.2.1 Monte Carlo sampling of Compton scattered photons 119
  4.2.2 Monte Carlo sampling of coherent scattered photons 123
4.3 MONTE CARLO COMPUTER MODEL 130
  4.3.1 Introduction 130
  4.3.2 Photon life histories 132
4.4 RESULTS FROM THE MONTE CARLO SIMULATION 140
  4.4.1 Program output 140
  4.4.2 Multiple scatter and type of interaction 142
  4.4.3 Determination of A_1 and its dependence on examined material position 145
  4.4.4 Dependence of scattered radiation on incident spectra 152
  4.4.5 Dependence of scattered radiation on phantom and examined material thickness 154
  4.4.6 Conclusions from the Monte Carlo simulation 158
4.5 MEASUREMENTS OF A_1 IN PRESENCE OF SCATTERED RADIATION 159
  4.5.1 Experimental procedure 159
  4.5.2 Results 161
  4.5.3 Conclusion 165

CHAPTER 5 APPLICATION *IN VITRO* OF DUAL ENERGY ANALYSIS

5.1 GALLSTONE ANALYSIS *IN VITRO* 167
5.2 X-RAY DIFFRACTION ANALYSIS 172
5.3 COMPARISON OF DUAL ENERGY ANALYSIS WITH CRYSTALLOGRAPHIC METHODS 179

CHAPTER 6 CONCLUSIONS AND DISCUSSIONS

6.1 DUAL ENERGY PROCEDURES 181
6.2 EFFECTS OF SCATTERED RADIATION 183
6.3 GALLSTONE ANALYSIS 186
6.4 FUTURE WORK 188

REFERENCES 190

FIGURES

1.1 Split-filter-CT 26
1.2 Basic design of the dual energy system 29
1.3 Phantom and detector arrangement 33
1.4 Iso-transmission lines for T_h and T_l 39
1.5 Beam hardening effect for A_1 44
1.6 Beam hardening effect for A_2 44

2.1 Narrow beam attenuation computer model 52
2.2 Attenuation curve for NE102A 57
2.3 Attenuation curve for $Bi_4Ge_3O_{12}$ 58
2.4 Attenuation curve for CaF_2 59
2.5 Attenuation curve for CsI 60
2.6 Attenuation curve for NaI 61
2.7 Attenuation curve for $ZnWO_4$ 62
2.8 CsI / Cu / NaI detector system with test phantom 66
2.9 Value of A_1 for different sets of windows 68
2.10 Transmitted spectra through test phantom 70
2.11 Dependence of A_1 and A_2 on incident spectra 71
2.12 Dependence of A_1 on material thickness 74
2.13 Effect of phantom depth 77

3.1 Split detector system block diagram 82
3.2 Detector arrangement 83
3.3 Response of PM tubes 84
3.4 Multiplexer / ADC board test 86
3.5 PHA dual energy system block diagram 88
3.6 Counters test 89
3.7 Scintillation system performance 90
3.8 J&P response 90
3.9 PM tube and ionisation chamber outputs 92
3.10 Monitoring of the x-ray tube output with time 94
3.11 Set-up of dual energy probes 96
3.12 Dependence of A_1 on incident spectra 103
3.13 Dependence of A_1 on material thickness 105
3.14 Dependence of A_1 on water phantom 107

4.1 Probability distribution for Monte Carlo rejection sampling 118
4.2 Comparison of the Khan rejection technique with the Klein-Nishina distribution at 40 keV 122
4.3 Form factors for water 126
4.4 Comparison of the inversion rejection technique with the coherent angular distribution for water at 40 keV 129
4.5 Monte Carlo computer model 132
4.6 Incident radiation 133
4.7 Direction cosines 136
4.8 Opening angle correction 139
4.9 Flow chart of the Monte Carlo program 141
4.10 Effect of scatter. PHA method. Material at top surface 146
4.11 Effect of scatter. PHA method. Material at bottom surface 147
4.12 Effect of scatter.Split detector method. Material at top surface 150
4.13 Effect of scatter. Split detector method. Material at bottom surface 151
4.14 Dependence of scatter on incident polyenergetic beam 153
4.15 Dependence of scatter on patient thickness 155
4.16 Dependence of scatter on material thickness 157
4.17 Experiment set up in presence of scatter 160
4.18 Sequence of measurement with large incident x-ray field 161
4.19 Comparison of experimental and Monte Carlo results when material position is changed 163
4.20 Comparison of experimental and Monte Carlo results for various incident spectra 164

5.1 Section through the abdomen region 168
5.2 Gallstone analysis *in vitro* experiment 168
5.3 Perspex block 169
5.4 Gallstone analysis 171
5.5 Gallstone g_1 174
5.6 Gallstone g_2 175
5.7 Gallstone g_3 176
5.8 Gallstone g_5 177

TABLES

1.1 Z exponents for partial photon interaction cross-section per electron 20
1.2 Total and partial effective atomic numbers at 40 keV 20
1.3 Effective energies for three x-ray spectra 22
1.4 Methods of analysis of gallstones 47
1.5 Gallstone components 48
1.6 Composition and type of gallstone 49

2.1 Physical constants of the detector materials and filters 53
2.2 Results from the NE102A detector 56
2.3 Results from the $Bi_4Ge_3O_{12}$ detector 58
2.4 Results from the CaF_2 detector 59
2.5 Results from the CsI detector 60
2.6 Results from the NaI detector 61
2.7 Results from the $ZnWO_4$ detector 62
2.8 Dual energy calibration materials 65
2.9 Selected sets of windows 69
2.10 Effective energy variations 77
2.11 Variation of A_1 with water phantom 78

3.1 Variation of PM tubes with ionisation chamber 93
3.2 Effective energies 99
3.3 A_1 sensitivity 110
3.4 Probability of success 111
3.5 Performance of the dual energy probes measuring A_1 113

4.1 Physical properties of each medium 131
4.2 Multiple scattering compared to single scattering 143
4.3 Single coherent scattering compared to single Compton scattering 144

5.1 X-ray diffraction analysis results 173
5.2 Comparison of dual energy analysis with crystallographic methods 180

ACKNOWLEDGEMENTS

The work presented in this thesis was suggested by and performed under the supervision of Dr Robert D. Speller. It is with pleasure that I acknowledge his helpful advice, encouragement and guidance throughout the progress of this work. I wish also to thank Nia Harrison, Michael Mooney and especially Gary Royle for their patience and care in reading this thesis.

I am deeply indebted to Dr Andrew Coleman for providing the gallstones from St Thomas' Hospital London.

ERRATA

1. Page 19, from equation 1.16 to 1.18 replace $\{ \quad \}^{m-1}$ by $\{ \quad \}^{1/(m-1)}$ with $m=\alpha$, β and γ respectively.
2. Page 26, figure 1.1 : At source position B, x-ray path should go through filter R instead of L.
3. Page 39, figure 1.4: for '$T_l = mt_w + t_{al}$' read '$T_l = mt_w + nt_{al}$'.
4. Page 41, after equation 1.60: for '$s_1 = \int I_{2o}(E)$.....' read '$s_2 = \int I_{2o}(E)$.....'.
5. Page 51, line 17: for 'the the' read 'the'.
6. Page 52, line 2: for 'Ruchdshel' read 'Ruchdeshel'.
7. Page 55, line 4: for 'equation 1.18' read 'equation 1.24'.
8. Page 97, line 21: for '$D_w(E)$' read '$D_m(E)$'.
9. Page 99, line 1: for 'Table 3.3' read 'Table 3.2'.
10. Page 100, line10: delete '(table 3.4)'.
11. Page 102, line 1: for 'table 2.4' read 'table 2.5'.
12. Page 112, line 26: for 'numbers' read 'number'.
13. Page 121, line 13: for '$G_2 = \int_1^{\rho} g_1(r)\, dr$' read '$G_2 = \int_1^{\rho} g_2(r)\, dr$'.
14. Page 128, line 16: for 'ie' read 'i.e.'.
15. Page 137, line 9: for 'scattering scattering' read 'scattering'.
16. Page 141, figure 4.9: 'Coherent scattering' box should be connected to 'Determine interaction site' box.
17. Page 152, line 8: for 'on a' read 'and'.
18. Page 162, line 2: for 'figure 4.22' read 'figure 4.19'.
19. Page 167, line 19: for 'figure 4.20' read 'figure 4.17'.

CHAPTER 1 INTRODUCTION AND BACKGROUND TO THESIS

1.1 Introduction

In any x-ray examination the transmitted photon spectrum contains information relating to the physical parameters of tissues under investigation. Conventional radiography detectors respond only to the total flux of x-rays, ignoring the information present in the energy distribution of the spectrum. Thus, the detector output, which can be related to the total linear attenuation coefficient, is measured at a single average energy while the behaviour of the complete attenuation coefficient is ignored. Dual energy radiography provides a useful means for extracting energy dependent information about tissue attenuation properties, using two different x-ray beam energies. This information can be used to characterize the effective atomic number of a lesion once it has been detected, a parameter of great importance in diagnostic radiology. The information can also be used to remove the effect of overlying tissue and thus greatly enhances the probability of detection of a lesion.

The concept of utilising two photon energies to obtain information on tissue characterization was first suggested by Jacobson in 1953. The idea was extended to bone mineral analysis in the mid 60's and to video analog subtraction imaging in the early 70's. More recently it has been applied to computed tomography (CT), digital scanned projection radiography and digital subtraction angiography. As CT systems allow precise absolute measurements of the attenuation coefficient most of the dual energy work has been done on modified CT scanners. However, the high cost of a CT system makes it prohibitive for routine dual energy use. Digital scanned projection radiography promises to become a more cost effective implementation of dual energy techniques since conventional x-ray generating equipment already available in radiography departments can be utilised.

The aim of this thesis was to consider the application of dual energy techniques to pseudo-real time dual energy probes to be used in a fluoroscopic mode, in order to provide quantitative information about the chemical composition of particular regions of the examined tissues. This involved the design and construction of suitable dual energy probes and of a read-out system for quantitative measurements. In order to fully evaluate the dual energy capability of the detectors and to assist in their improvement these systems were both simulated by computer and by experimental means. The systems were based on the dual detector principle, i.e. the measured energy separation into a high energy and a low energy is obtained from a single exposure. Two types of probes were assessed; one type using beam filtration to change the effective energy of the measured spectrum (the split detector method) and the other one using pulse height analysis (PHA probe) to choose independently the two energy ranges required for dual energy work.

This thesis is organised as follows:

The remainder of chapter 1-Several terms used throughout the thesis are defined in section 1.2. A review of the current progress in dual energy is given in section 1.3 with particular emphasis on the clinical application and the usefulness of these techniques. Section 1.4 considers the basic design of the probes employed for dual energy work and section 1.5 gives detail of the analysis that was used in evaluating the signals from such probes. Section 1.6 describes some of the problems encountered in the analysis. Finally the possible clinical application of such systems are investigated in section 1.7.

Chapter 2 - The design of each type of dual energy probe for use in fluoroscopic x-ray examinations is investigated. A narrow beam computer model is used to predict the optimum system for the split detector probe and the optimised energies for the PHA probe.

Chapter 3 - The construction of the detector probes for pseudo-real time clinical use during x-ray procedures is explained. Three types of probes are considered; the split detector probe, the scintillation PHA probe and the semiconductor PHA probe. All detectors are evaluated experimentally and a comparison is made between each of the detectors and with relation to the results of the computer model.

Chapter 4 - The contribution of scattered radiation to the dual energy system is and experimental results are compared.

Chapter 5 - As a demonstration of the clinical usefulness of this technique the detector probes are applied to gallstone analysis *in vitro*.

Chapter 6 - The results are summarised and conclusions drawn.

1.2.1 Linear Attenuation Coefficients and the Mixture Rule

Any x-ray beam which traverses a tissue is attenuated. The degree of attenuation is dependent upon the type and thickness of tissue and on the energy of photons; it is described by the linear attenuation coefficient, μ, for that tissue. If we consider a narrow beam of x-rays of intensity, I, which traverses a thin slab of material of thickness ds, the small change in intensity, dI, can be described by the relation:

$$dI / I = -\mu(E)\, ds \qquad 1.1$$

From this expression μ is seen to be the fractional reduction in intensity produced by a unit thickness of material. The relation holds only when ds and dI are very small and where no scattered radiation is included in the measurement of dI. The units of μ are inverse length.

Integrating both sides of equation 1.1 over a finite length x of a given material and for an initial x-ray intensity I_o at x=0, it is found that the intensity of the beam, I, at any point x in the material can be given by:

$$I / I_o = \exp(-\mu(E)\, x) \qquad 1.2$$

This expression is valid for monochromatic radiation in the absence of scattered radiation.

The linear attenuation coefficient of an element i can be written as μ_i. Values of μ_i have been tabulated in the literature for most of the elements at various energies. For each photon energy and for each type of photon interaction it is possible to quote a probability that the photon will interact with a given atom of an element; this probability can be defined by a cross-section for the interaction which is called the atomic cross-section. For a single element the total atomic cross-section is directly related to the linear attenuation coefficient by the following expression:

$$\mu_i = \sigma_i \, n_i \qquad 1.3$$

where n_i is the number of atoms per unit volume and σ_i is the total cross-section of the individual atoms. The total atomic cross-section is dependent on both the atomic number of the element Z_i and the photon energy E, so equation 1.3 can be written as

$$\mu_i = \sigma_i(Z_i,E) \, n_i \qquad 1.4$$

For a compound it is possible to sum the individual total atomic cross-sections for each element. This is often termed as the mixture rule and is given by

$$\mu = \Sigma_i \, \sigma_i(Z_i,E) \, n_i \qquad 1.5$$

Significant departures from this rule occur when the effects of molecular bonding and chemical or crystalline environment become important (Hubbell 1969). It has been estimated that for photon energies above 10 keV and more than 1keV away from an absorption edge the errors from this approximation are generally less than a few percent (Kouris *et al* 1982).

1.2.2 Parametrisation of the Linear Attenuation Coefficient

The feasibility of characterizing tissue quantitatively by x rays depends on a representation of the linear attenuation coefficient in terms of essential physical parameters of the material. In the energy range $20<E<140$ keV three different x-ray attenuation processes are known to occur :

i) photoelectric absorption

ii) incoherent or Compton scattering

iii) coherent scattering

Each process can be described by an atomic cross-section for the interaction of a photon with a given atom. Since each of these three independent processes of attenuation has a different atomic number and energy dependence they can be used to parametrise μ. Combining equation 1.5, which describes the mixture rule, it is possible to write equation 1.6 :

$$\mu(E) = \Sigma_i n_i \sigma^{phot}(Z_i,E) + \Sigma_i n_i \sigma^{coh}(Z_i,E) + \Sigma_i n_i \sigma^{incoh}(Z_i,E) \qquad 1.6$$

where each term describes one of the three attenuation processes. It is frequently assumed that it is permissible to rewrite equation 1.6 as

$$\mu(E) = \Sigma_i n_i K^{phot}(E) Z_i^{\alpha} + \Sigma_i n_i K^{coh}(E) Z_i^{\beta} + \Sigma_i n_i K^{incoh}(E) Z_i^{\gamma} \qquad 1.7$$

where K^{phot}, K^{coh} and K^{incoh} contain the energy dependent part of the atomic cross-section and n_i and Z_i describe the dependence of these cross-sections on the element i.

Accurate fits to the data obtained using equation 1.7 show that α, β and γ must depend both on the photon energy (Hawkes and Jackson 1980) and on the composition of the material (White 1977).

Jackson and Hawkes (1981) reported that the fault in the preceding equation (1.7) lies in the assumption that each separate cross-section can be factorised into a function of E and a function of Z. In dual energy radiology however, equation 1.7 can be used as the basis for extracting information on the composition of a tissue from measurements of μ at two independent energies. The errors in the measurement can be large in comparison with errors due to the expression used for the attenuation coefficient (Kouris *et al* 1982).

The following sections consider the various representations that have been used.

i) Photoelectric / Compton Representation

A number of different expressions of equation 1.7 are found in the literature (Rutherford *et al* 1976, Brooks 1977) but the one most commonly used in dual energy radiology is that given by Alvarez and Macovski (1976) (equation 1.8), which is also known as the photoelectric / Compton representation (the dual energy analysis discussed in section 1.5 is based on this procedure) :

$$\mu(E) = \Sigma_i \, C \, E^{-3} \, n_i \, Z_i^4 + \Sigma_i \, F_{KN}(E) \, n_i \, Z_i \qquad 1.8$$

where E^{-3} is the approximate energy dependence of the photoelectric interaction at diagnostic energies, $F_{KN}(E)$ is the cross-section per free electron given by the Klein-Nishina formula and C is a constant. In fact the first term of equation 1.8 represents not only the photoelectric absorption but also includes coherent scattering and any binding energy correction due to coherent scattering from bound electrons and the deviation of incoherent scattering from free electron results (Kouris *et al* 1982).

Equation 1.8 can be written as :

$$\mu(E) = a_1 \, E^{-3} + a_2 \, F_{KN}(E) \qquad 1.9$$

where a_1 and a_2 are a set of energy independent parameters which can be used to characterize tissues.

X-ray systems fundamentally measure line integrals of the linear attenuation coefficient when a beam passes through an object, i.e. $\int \mu(x,y,z,E)\, dt$, where dt is a short section of path length. Hence

$$\int \mu(x,y,z,E)\,dt = A_1 E^{-3} + A_2 F_{KN}(E) \qquad 1.10$$

where $A_1 = \int a_1(x,y,z)dt$ and $A_2 = \int a_2(x,y,z)dt$

To obtain the parameters A_1 and A_2, intensity measurements are made with two different source spectra :

$$I_1 (A_1,A_2) = \int S_1(E) \exp\{-A_1 E^{-3} - A_2 F_{KN}(E)\}\, dE \qquad 1.11$$

$$I_2 (A_1,A_2) = \int S_2(E) \exp\{ -A_1 E^{-3} - A_2 F_{KN}(E) \}\, dE \qquad 1.12$$

where S_1 and S_2 are either photon number spectra or intensity spectra, and I_1 and I_2 are either total counts or intensities. The steps required to obtain A_1 and A_2 are described fully in section 1.5.

ii) Equivalent Thickness Representation

The attenuation coefficient of a tissue can also be represented by other specific sets of parameters such as the thickness of two materials. For example suitable thicknesses of water and aluminium can be chosen to simulate a particular thickness of soft tissue, thus, providing an equivalent thickness representation of the tissue. Several combinations have been proposed.

i) Water and bone (Chan *et al* 1976).
ii) Water and aluminium (Brody *et al* 1981).
iii) Lucite and aluminium (Lehman *et al* 1981).
iv) Water and calcium chloride (Hawkes *et al* 1986).

These representations are equivalent to each other (including photoelectric /

Compton representation) since each set completely represents the attenuation properties for a given energy. For example the water / aluminium representation of the linear attenuation coefficient $\mu(E)$ is given by

$$\mu(E) = t_w\ \mu_w(E) + t_{al}\ \mu_{al}(E) \qquad 1.13$$

where t_w, t_{al} are the equivalent thicknesses of water and aluminium respectively and μ_w, μ_{al} are the linear attenuation coefficients of water and aluminium respectively. This representation is convenient in that a soft tissue (water) only or a bone tissue (aluminium) only image can be produced in projection radiography and is therefore, useful in removing overlying bone structures.

1.2.3 Effective Atomic Number

It is often found useful to characterize a mixture or tissue by an effective atomic number. Rewriting n_i, the number of atoms of an element i, in terms of n_o, the total number of atoms in a compound per unit volume, and λ_i, the fractional volume of an element i, :

$$n_i = n_o\, \lambda_i \qquad 1.14$$

and combining equations 1.7 and 1.14 produces the following,

$$\mu(E) = n_o\, [\Sigma_i\, \lambda_i\, Z_i]\ \left\{\Sigma_i\, \lambda_i\, Z_i^{\alpha-1}\, K^{phot}(E) \ + \ \Sigma_i\, \lambda_i\, Z_i^{\beta-1}\, K^{incoh}(E) \right.$$

$$\left. + \ \Sigma_i\, \lambda_i\, Z_i^{\gamma-1}\, K^{coh}(E)\right\} \qquad 1.15$$

where the terms $\Sigma_i \lambda_i Z_i^{\alpha-1}$, $\Sigma_i \lambda_i Z_i^{\beta-1}$ and $\Sigma_i \lambda_i Z_i^{\gamma-1}$ can be used to define effective atomic numbers for *each* interaction in the tissue. Conventionally, effective atomic numbers are defined only for partial processes (White 1977). These are given by

$$Z^*_{photo} = \{ \Sigma_i \lambda_i Z_i^{\alpha-1} \}^{\alpha-1} \qquad 1.16$$

$$Z^*_{incoh} = \{ \Sigma_i \lambda_i Z_i^{\beta-1} \}^{\beta-1} \qquad 1.17$$

and

$$Z^*_{coh} = \{ \Sigma_i \lambda_i Z_i^{\gamma-1} \}^{\gamma-1} \qquad 1.18$$

The fractional volume, λ_i, of an element i is defined as

$$\lambda_i = [W_i (Z_i / A_i)] / [\Sigma_i W_i (Z_i / A_i)] \qquad 1.19$$

where W_i, Z_i and A_i are the fractional chemical composition, atomic number and atomic weight of the individual elements in the material respectively. Yang *et al* (1987) have calculated the values of the α, β and γ exponents for each energy by interpolating the photon interaction cross-section per electron of the corresponding partial process (i.e. $Z_i^{\alpha-1} K^{phot}(E)$, $Z_i^{\beta-1} K^{incoh}(E)$ and $Z_i^{\gamma-1} K^{coh}(E)$) versus the atomic number, Z_i. These values are shown in table 1.1. As an example table 1.2 shows how the partial effective atomic number can differ for the same material or tissue.

The definition of the total effective number, Z^*, employed in this thesis is given by Yang *et al* (1987) :

$$\sigma_{em} = K^{phot}(E) Z^{*(\alpha-1)} + K^{incoh}(E) Z^{*(\beta-1)} + K^{coh}(E) Z^{*(\gamma-1)} \qquad 1.20$$

where σ_{em} is the attenuation cross-section per electron of material m.

Combining equation 1.16, 1.17 and 1.18 with equation 1.20 we obtain

$$K^{phot}(E) {Z^*_{photo}}^{(\alpha-1)} + K^{incoh}(E)\, {Z^*_{incoh}}^{(\beta-1)} + K^{coh}(E)\, {Z^*_{coh}}^{(\gamma-1)} =$$

$$K^{phot}(E) Z^{*(\alpha-1)} + K^{incoh}(E)\, Z^{*(\beta-1)} + K^{coh}(E)\, Z^{*(\gamma-1)} \qquad 1.21$$

Table 1.1 Z Exponents for Partial Photon Interaction Cross-Sections per Electron.

Energy (keV)	Photoelectric effect α-1	Compton scattering β-1	Coherent scattering γ-1
10	3.52	-0.225	1.44
15	3.62	-0.164	1.51
20	3.68	-0.128	1.56
30	3.75	-0.087	1.61
40	3.80	-0.066	1.64
50	3.84	-0.051	1.67
60	3.86	-0.041	1.68
80	3.90	-0.029	1.70
100	3.93	-0.022	1.71

calculated exponents for a 10 to 100 keV energy range (Yang *et al* 1987)

Table 1.2 Total and Partial Effective Atomic Numbers at 40 keV.

	photoelectric effect	Compton scattering	coherent scattering	total*
ICRU muscle	7.73	5.18	6.96	7.55
ICRU bone	12.65	6.67	9.75	11.95
fat**	5.99	4.12	5.47	5.86

*data obtained from Yang *et al* (1987)

**chemical composition from White (1977)

In the energy range 20 to 140 keV β-1 is almost equal to zero, hence

$$K^{phot}(E)Z^*_{photo}{}^{(\alpha-1)} + K^{coh}(E)\, Z^*_{coh}{}^{(\gamma-1)} \cong$$

$$K^{phot}(E)Z^{*(\alpha-1)} + K^{coh}(E)\, Z^{*(\gamma-1)} \qquad 1.22$$

The solution of this equation, Z^* (the total effective atomic number), must satisfy the condition

$$Z^*_{coh} < Z^* < Z^*_{photo} \qquad 1.23$$

This condition is illustrated in table 1.2.

1.2.4 Effective Energy and Effective Attenuation Coefficient

The concept of an effective energy is commonly used in diagnostic radiology to characterize a polyenergetic x-ray spectrum. A single energy is used to describe the x-ray spectrum. The effective attenuation coefficient μ_{eff} of a particular material for a polyenergetic x-ray spectrum is given by :

$$\mu_{eff} = \mu\,(E_{eff}) = \left[\, {}_{o}\!\int^{Em} \mu_m(E)\, I_o(E)\, dE \,\right] / {}_{o}\!\int^{Em} I_o(E)\, dE \qquad 1.24$$

where $I_o(E)$ is the intensity distribution of the x-ray spectrum, Em is the maximum energy of the spectrum and $\mu_m(E)$ is the linear attenuation coefficient of material m at energy E.

The definition of effective energy, E_{eff}, used in this thesis is the monoenergetic photon energy at which the linear attenuation coefficient of a certain material is equal to the effective attenuation coefficient, μ_{eff}, of the material. Hence the effective energy depends on the material used to weight the spectrum. Materials with high atomic numbers will give more weight to the lower energy part of the spectrum. Table 1.3 shows however that the variation in the effective energy relative to water, ICRU muscle, ICRU bone and titanium is not large.

The mean photon energy of the spectrum is given in Table 1.3 and is defined as :

$$E_{mean} = \left[\int_0^{Em} I_0(E)\, E\, dE \right] / \int_0^{Em} I_0(E)\, dE \qquad 1.25$$

Table 1.3 Effective Energies for Three X-ray Spectra.

	Effective Energy (keV)		
Weighting Material	70 kVp	80 kVp	90 kVp
Water	32.0	34.0	35.8
ICRU muscle	32.0	33.9	35.8
ICRU bone	31.5	33.4	35.1
Titanium	31.5	33.4	35.0
Mean Energy	38.2	41.7	45.0

Spectral data taken from Birch *et al* (1979) and the attenuation data from Storm and Israel (1970).

The effective energies are used to describe transmitted and absorbed photon spectra. As a convention all effective energies quoted in this thesis have been calculated using water as the weighting material.

1.3 Dual Energy Techniques

The common feature of all dual energy techniques is to obtain dual energy information from a particular region of the examined tissue. Dual energy techniques differ in the manner by which the detector signals of the beam intensities at two different effective x-ray energies E_1 and E_2 arise, and in the type of detector used.

Dual kVp methods utilise two spectra obtained by operating the x-ray tube at two different voltages. Dual filtering provides two spectra by filtering one spectrum with two different filters. In the dual detector methods, a single spectrum gives rise to two different measurements from two detectors having different energy responses. The difference between the dual detector and the dual filtering method is that for a fixed moment in time a dual detector measures the attenuation along one ray path at two effective energies whereas a dual filtering system measures one effective energy only at a time along one ray path. However, dual filtering systems collect data from different rays at two energies simultaneously (cf. figure 1.1).

The majority of dual energy work has been applied to computerised tomography (CT) systems as they allow precise measurement of the attenuation coefficient to be made. Dual energy techniques applied to projection imaging have been also reported.

1.3.1 Dual KVp Technique

For the dual kVp technique the operating voltage of the x-ray tube is switched between two potentials thus resulting in two spectra. This technique was used by Rutherford *et al* (1976) to obtain CT projection data at two different effective energies using peak tube voltages of 100 kVp and 140 kVp, giving E1 and E2 as 62 keV and 74 keV respectively. In a phantom study using this technique a precision of 3% was obtained in the measurement of effective atomic number. However, this technique possesses a number of inherent problems and limitations as it is slow, at least twice the dose is delivered to the patient and there will be poor registration between the images due to motion artifacts. Recently, rapid kVp switching during a single scan has been proposed by Kalender *et al* (1986) and by Vetter *et al* (1986). Studies were performed to eliminate beam hardening artifacts, to quantify calcium in pulmonary nodules and to determine bone mineral content of defined skeletal portions using phantoms and patients. As an example of the last application, it has been shown (Vetter *et al* 1986) that the dual energy technique (the high and low energy images were acquired at 125 and 75 kVp) can be used to selectively measure the mineral component almost independently of variations in bone marrow. Conventional CT measurements could be inaccurate since at energies of 100-140 kVp mineral accounts for only 10%-30% of the total attenuation in trabecular bone (Weissberger *et al* 1978), the accuracy, therefore, is affected by the amount of marrow fat present. A number of other clinical applications in dual energy CT has also been reported, such as tissue characterization (Hawkes *et al* 1986). In this example scans were taken at 140 kVp and 87 kVp. Adaptation of CT to dual energy work has proved to be successful, yet the high cost of such a system represents a major disadvantage. Moreover, the long data acquisition time required will limit the number of examinations likely to make use of the facility.

The application of dual energy projection radiography (DEPR) has generally been employed in subtraction methods, removing overlying or underlying structure for enhancing features of interest. An extensively modified CT scanner for use in dual energy scanned projection radiography was reported by Brody *et al* (1981). The detector array consisted of xenon ionisation chambers. A fast pulsed dual kVp generator that alternates between 135 kVp and 85 kVp (a few ms between them) along with a synchronised rotating filter assembly was used, giving effective energies of 45 and 85 keV. Selective tissue cancellation was carried out using the equivalent thickness of aluminium / lucite representation of the attenuation coefficients. A clinical study showed the technique to be useful in abdominal radiography (removal of bowel gas shadows of the gallbladder and kidney) and in chest radiography increasing low contrast detectability. DEPR has also been reported to enhance detectability of calcifications in mammographic examinations (Johns *et al* 1985). These successful experiments were carried out using excised breast tissue samples.

As pointed out by Kelcz *et al* (1979) the major advantage of dual kVp methods is that good energy separation between the two spectra can be achieved.

1.3.2 Dual Filtering Technique

Dual filtering affects the effective energy of the x-ray beam incident on the probe. A single scan is needed to obtain the data, avoiding the problems associated with a double scan. Utilising two different filters results in the two spectra required for dual energy radiography.

Ritching and Pullan (1979) used a post-patient arrangement of a split filter system that involved only a minor hardware modification to a CT scanner. Alternate slits of the detector collimator were covered by tin foil, raising the effective energy of the x-ray spectrum entering the detectors covered by the foil. The geometry of the scanner used was such that adjacent detectors corresponded to successive scan projection angles. The projection data file stored in the computer thus consists of two interleaved sets of projection angle data, one corresponding to the usual x-ray energy (uncovered detectors) the other at a higher x-ray energy (covered detectors). The two sets of data are simply separated using computer software such that double scan projection data are obtained from a single scan. Rutt and Fenster (1980) filtered the x-ray tube prior to its incidence on the patient so that the photons stopped by the filter do not contribute to patient doses. They employed two filters naming their technique "Split- Filter-CT" (figure 1.1).The method involves filtering two halves of the x-ray fan beam differently ensuring that every path in the patient cross-section can be measured with two different beam filtrations during a 360° single scan. This split filtration geometry results in dual energy measurements of each cross-sectional path through the patient. The main objective was to correct for spectral artifacts of the acquired CT images. It was used successfully in a head phantom.

Figure 1.1 Split-Filter-CT

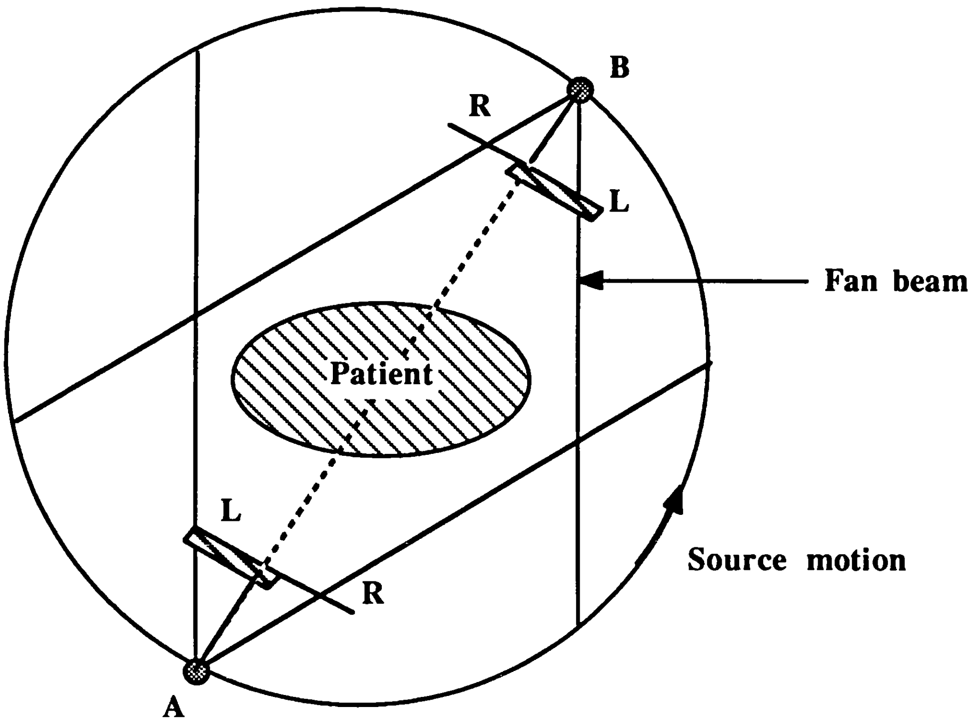

**Key : A and B are two positions of the x-ray tube.
L and R are filters of different materials or thickness.**

1.3.3 Dual Detector Methods

Dual detector methods employ an energy discrimination probe that is capable of measuring the x-ray intensity at two different effective energies simultaneously. This is achieved either by beam filtering or by designing the probe to respond to different parts of the spectrum.

A special version of a high pressure xenon detector array for application in dual energy CT has been investigated by Fenster (1978). The detector consists of two collector plates separated into two regions; a front section (4.5 cm long) responds to an x-ray beam of lower effective energy, the back section (15.5 cm long) to an x-ray beam of higher effective energy since a large amount of the low energy photons have been stopped in the first region . In a computer simulation the electron density and the effective atomic number were obtained with an accuracy better than 4%. This split septaless xenon detector has been recently modified for future dual energy chest radiography (Cardinal and Fenster 1988). An inactive segment has been incorporated between the front and rear sections, conveniently forming a beam hardening filter.

Speller *et al* (1983) developed a specially modified cassette that enables conventional dual energy radiographs to be taken during a single exposure. The cassette comprises of two film screen combinations separated by a copper filter. Digitisation of the films is achieved by local optical density readings. 86 kVp and 0.67 mm of copper were selected as an optimum pair of values. It was shown that gallstone identification was feasible with this system.

As well as scintillation detectors, split detector ionisation chambers with front and back electrodes have also been used. Horrocks and Speller (1983) have designed a dual energy ionography system which consists of two chambers separated by a copper filter. Images collected on aluminised melinex film, one from each chamber, provide additional diagnostic information in the form of chemical identification of the irradiated tissues.

Barnes *et al* (1985) reported a dual energy x-ray detector for projection radiography. The detector employed a moderately low atomic number phosphor (Y_2O_2S) coupled with a photodiode array followed by a high atomic number phosphor (Gd_2O_2S) coupled with a second photodiode array. A filter is placed between these two sections to increase the effective energy of the x-ray spectrum incident on the second part of the detector system. Bone and soft tissue images from a chest phantom were obtained. It was found that the dual energy detector images at 140 kVp when compared to the dual kVp method at 80 and 140 kVp, required a lower tube load, but resulted in higher noise levels. Recently, using a dual energy detector system, Fraser *et al* (1986) successfully applied the scanned dual energy digital radiography to the detection of calcification in pulmonary nodules. The clinical significance of such a result is that calcification in a pulmonary nodule almost excludes the possibility of malignancy.

The systems outlined above indicate that significant advances could be made in the diagnosis of disease and in the clinical management of a patient through the widespread use of dual energy techniques. One area clearly missing is the need for real time examination of small tissue regions that are seen during a fluoroscopic procedure. An alternative technique of direct discrimination using pulse height analysis is also worthy of consideration. Such devices are the subject of this thesis and their basic design is considered in the following section.

1.4 The Design of a Dual Energy Probe

The concept behind the proposed dual energy probe was to provide a technique for localised tissue characterization that could be readily available to all types of routine diagnostic screening examinations. Detectors with digital output provide the means for fast and efficient data collection as well as for rapid processing of measured raw data. Hence, digital scanned projection radiography (DSPR) follows from CT as a logical choice for efficient implementation of dual energy techniques. Cost considerations prohibit a widespread usage of dual energy CT. DSPR offers the advantage of utilising the conventional x-ray apparatus available in virtually every diagnostic x-ray department. Therefore, we took the logical step to start the design of a dual energy DSPR system comprising a dual detector probe and a mechanical scanning device. During the design the following conditions were taken into account :

i) Simultaneous production of two x-ray beam intensities at two different effective energies in order to minimise patient dose and to avoid any misregistration of x-ray paths due to patient movement.

ii) High detection efficiency in order to achieve maximum measurement precision and at the same time to minimise the dose given to the patient.

iii) Data collection, digitisation and processing of the dual energy data are to be carried out by a low cost, personal minicomputer for real time analysis.

iv) The dual detector probe should be compact with minimum weight and size to ensure that the probe can be hand held for local examination.

Figure 1.2 Basic design of the Dual Energy System.

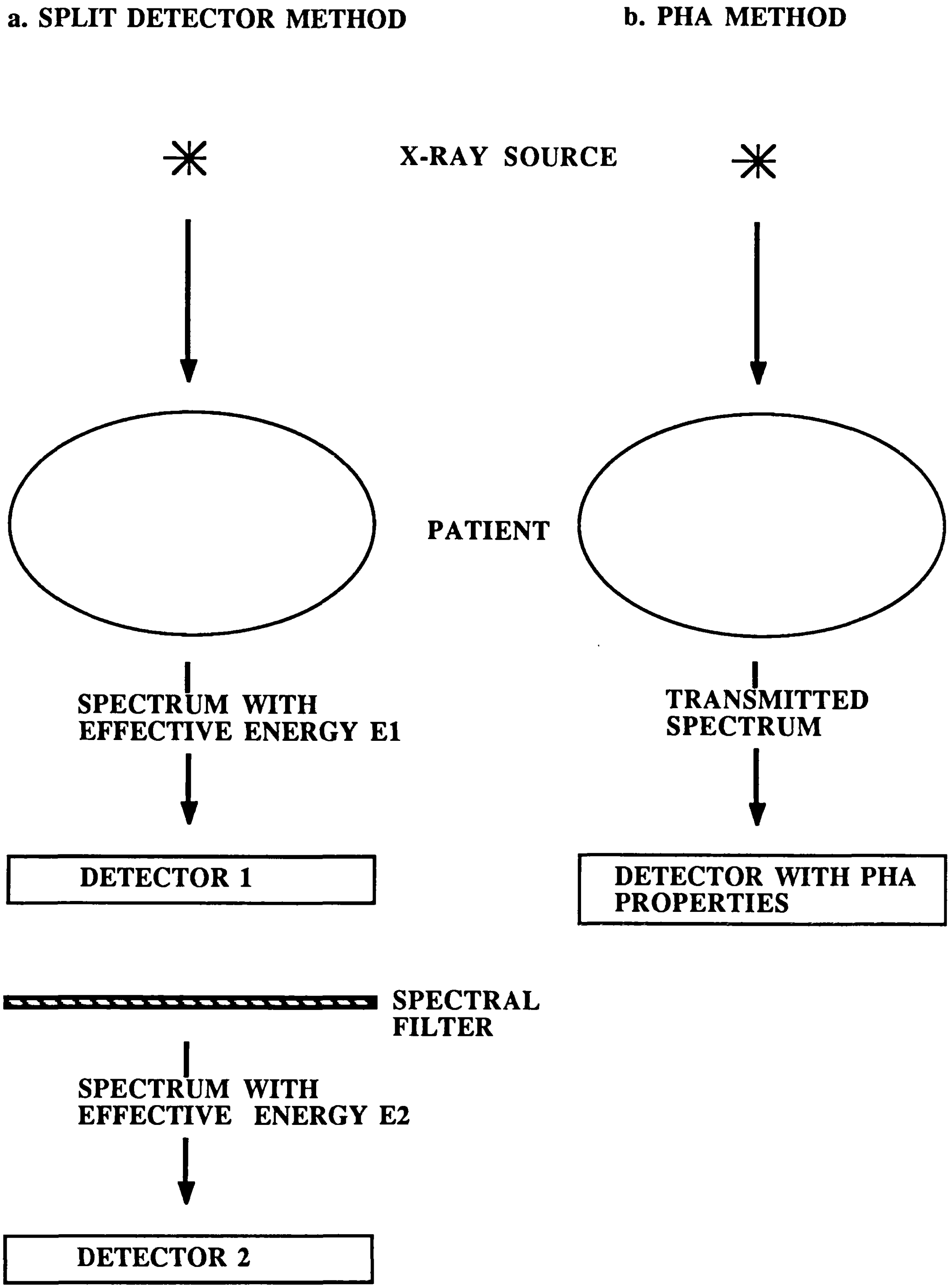

Energy discrimination from the same source spectrum was carried out using two principles; split detector system and pulse height analysis (PHA).

The split detector system has already been described by Speller *et al* (1983). This leads to the basic design of a single exposure dual energy detector, as shown in figure

1.2a. The system employs two detectors back to back in the path of the x-ray beam, they are optionally separated by a metal filter. The first detector absorbs primarily low energy photons, allowing most high energy photons to pass through. Both the first detector and the filter act together to preferentially remove the low energy photons from the incident spectrum, raising, by this process, the mean photon energy entering the second detector. This clearly leads to a difference in the effective energy of the spectrum absorbed by each detector. A mode of detection that is capable of measuring the overall energy absorbed by both detectors is sufficient to obtain energy separation since it is already provided by the physical principle of the split detector system.

Pulse height analysis systems record the energy deposited in the detector by each individual photon (figure 1.2b). Subsequent electronic signal processing counts the number of photons which lie within a defined range of energy. Hence, energy discrimination is an intrinsic characteristic of PHA systems. Since the range (usually called the window) of the x-ray energies can be selected by setting a lower and an upper threshold within the pulse processing chain, the width and position of the energy windows can be selected entirely according to the investigator's needs. Furthermore, even the number of energy windows selected can theoretically be unlimited. However, there is one price to pay for the versatility of PHA systems, and that is speed. Counting statistics limit the minimum time required to investigate one ray path in a dual energy imaging system.

1.5 Dual Energy Analysis

The analysis used in the dual energy system described in this thesis was based upon the procedure used by Alvarez and Macovski (1976) because of its direct physical analogy. For photon energies in the diagnostic range, they stated that the linear attenuation coefficient μ of a given material can be expressed as a linear combination of the photoelectric effect and Compton scattering (same equation as 1.8):

$$\mu(E) = A_1 E^{-3} + A_2 F_{KN}(E) \qquad 1.26$$

where: E is the incident energy,

$A_1 = k_1 \rho Z^4/A$ is the photoelectric contribution to μ, where k_1 is a constant, ρ is the mass density, Z is the effective atomic number and A is the atomic weight,

$A_2 = k_2 \rho \; Z/A$ is the Compton contribution to μ, where k_2 is a constant and $F_{KN}(E)$ is the Klein-Nishina cross-section for Compton scatter.

The ratio Z/A is constant for almost all materials (except hydrogen), therefore μ can be written as :

$$\mu(E) = k_3 \rho Z^3 E^{-3} + k_2 \rho F_{KN}(E) \qquad 1.27$$

with $A_1 \propto \rho Z^3$ and $A_2 \propto \rho$

For a given energy α, expressed in electron mass units, the Klein-Nishina cross-section for Compton scatter can be written as the following, (Evans 1955) :

$$F_{KN}(E) = (1+\alpha)\alpha^{-2} \left\{ 2(1+\alpha) / (1+2\alpha) - \alpha^{-1} \ln(1+2\alpha) \right\} + 0.5\,\alpha^{-1} \ln(1+2\alpha) - (1+3\alpha) / (1+2\alpha)^2 \qquad 1.28$$

with $\alpha = E / 510.975$ when E is expressed in keV units.

The dual energy problem is to determine the values of A_1 and A_2, where A_1 is proportional to the cube of the atomic number, Z, and A_2 is proportional to the physical density ρ of the material under consideration. Since two unknowns can be computed out of two equations, only dual measurement at two different energies leading to two independent equations for A_1 and A_2 is sufficient to solve the problem.

In the following discussion, a water phantom containing a small piece of material is being considered, as shown in figure 1.3. Two different photon paths through the phantom and detector arrangement are considered for the dual energy measurement.

i) photon path number 1 (including the material under investigation)

$$\int I_{1a}(E)\,dE = \int I_o(E)\exp(-\mu_m(E)\,t-\mu_w(E)\,x)\,dE \qquad 1.29$$

$$\int I_{1b}(E)\,dE = \int I_{1a}(E)\exp(-\mu_d(E)\,d)\,dE)\,dE \qquad 1.30$$

where I_o, I_{1a} and I_{1b} are the total transmitted photon counts (or intensities) at energy E.

The number of photons absorbed by the detector is $D_m(E)$;

$$D_m(E) = \int (I_{1a}(E) - I_{1b}(E))\,dE \qquad 1.31$$

$$D_m(E) = \int (I_o(E)\exp(-\mu_m(E)\,t-\mu_w(E)\,x)\left\{1-\exp(-\mu_d(E)\,d)\right\}dE \qquad 1.32$$

ii) photon path number 2 (background)

$$\int I_{2a}(E) = \int I_o(E)\exp(-\mu_w(E)\,x)\,dE \qquad 1.33$$

$$\int I_{2b}(E) = \int I_{2a}(E)\exp(-\mu_d(E)\,d)\,dE \qquad 1.34$$

The number of photons absorbed by the detector is :

$$D_w(E) = \int (I_{2a}(E) - I_{2b}(E))\,dE \qquad 1.35$$

$$D_w(E) = \int I_o(E) \exp(- \mu_w(E)\, x) \left\{ 1 - \exp(- \mu_d(E)\, d) \right\} dE \qquad 1.36$$

Figure 1.3 Phantom and Detector Arrangement

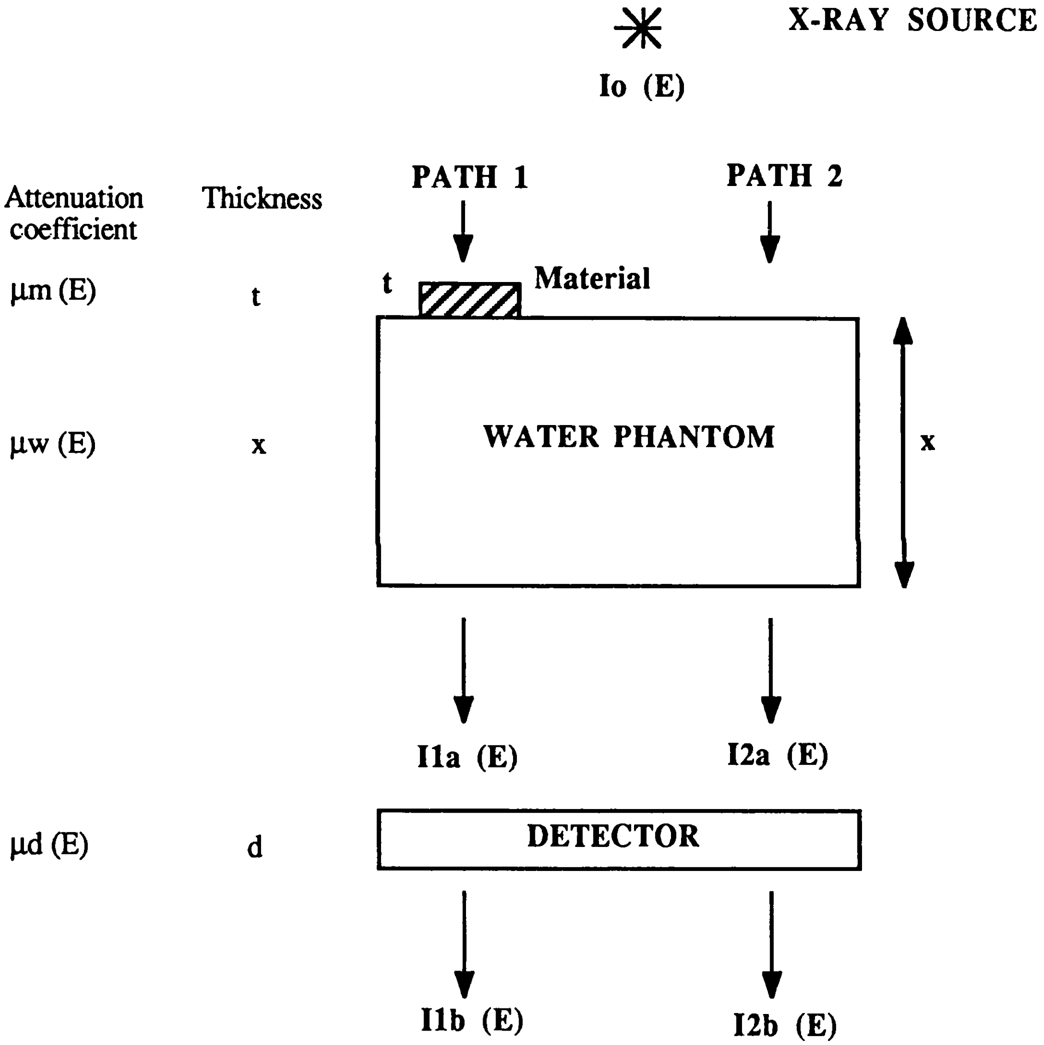

$D_m(E)$ and $D_w(E)$ will be related to the output signal, T(E), from the detector. In a linear system the absorbed energy will be proportional to the output signal from the detector. For a scintillation detector system it is assumed that $T(E) = k\, D(E)$ with no energy loss due to characteristic x rays or imperfection in the scintillation and photomultiplier tube combination. If the measurement made for the material is normalised to the background measurement then

$$T_w(E) / T_m(E) = D_w(E) / D_m(E) \qquad 1.37$$

For highly monochromatic sources at energies E_1 and E_2 :

$$D_m(E_1) / D_w(E_1) = \exp(- \mu_m(E_1)\, t) \qquad 1.38$$

$$D_m(E_2) / D_w(E_2) = \exp(- \mu_m(E_2)\, t) \qquad 1.39$$

Combining equations 1.38 and 1.39 with equation 1.26, the numbers of photons absorbed by the detector at energies E_1 and E_2 are given by the following equations

$$D_m(E_1) = D_w(E_1) \exp \left\{ (- A_1 / E_1^3 - A_2\, F_{KN}(E_1))\, t \right\} \qquad 1.40$$

$$D_m(E_2) = D_w(E_2) \exp \left\{ (- A_1 / E_2^3 - A_2\, F_{KN}(E_2))\, t \right\} \qquad 1.41$$

Finally, the value of A_1 and A_2 are obtained from equation 1.40 and equation 1.41:

$$A_1 = \left\{ F_{KN}(E_1) \ln [D_m(E_2) / D_w(E_2)] - F_{KN}(E_2) \ln [D_m(E_1) / D_w(E_1)] \right\}$$

$$\times\ E_1^3\, E_2^3 / R \qquad 1.42$$

$$A_2 = E_1^3 \ln [D_m(E_1) / D_w(E_1)] - E_2^3 \ln [D_m(E_2) / D_w(E_2)] / R \qquad 1.43$$

where $R = \left\{ F_{KN}(E_2)\, E_2^3 - F_{KN}(E_1)\, E_1^3 \right\} t$

This analysis is correct if E_1 and E_2 are monoenergetic photon energies and no scatter is detected. In practice, however, x-ray beams with associated effective energies E_1 and E_2 are more preferable than monochromatic sources since the polyenergetic x-ray spectra provide large intensities leading to short examination times. Another advantage is that the x-ray generating equipment is widely available in radiography departments. When considering x-ray beams as a source of energy, it is assumed that the effect of beam hardening, caused by introducing the material, is small and, therefore, E_1 and E_2 are not significantly changed as they pass through either the material (path 1) or the background (path 2).

If the material has sufficient attenuating properties, such that the effect is no longer negligible, equation 1.40 and equation 1.41 become :

$$D_m(E_{1m}) = D_w(E_{1w}) \exp \left\{ \left(- A_1 / E_{1m}^3 - A_2 F_{KN}(E_{1m}) \right) t \right\} \qquad 1.44$$

$$D_m(E_{2m}) = D_w(E_{2w}) \exp \left\{ \left(-A_1 / E_{2m}^3 - A_2 F_{KN}(E_{2m}) \right) t \right\} \qquad 1.45$$

where $E_m > E_w$ and the effective energies depend upon the material under examination. The magnitude of this effect is investigated by the computer simulation described in the second chapter. Methods of correcting for this effect are discussed in the following section.

1.6 Effects of Beam Hardening

The major problem in dual energy radiology, as seen in the previous section, is that while the dual energy analysis is based on the treatment of monoenergetic beam energies, in practice the measurements are made with two different polyenergetic x-ray spectra. The effective energy of the x-ray spectrum does not remain constant throughout the patient / detector system due to beam hardening effects which results in a non-linear relationship between the line integral of the linear attenuation coefficient and the absorber thickness (Brooks and Di Chiro 1976).

Various algorithms have been developed, in particular for dual energy subtraction imaging, in order to account for the beam hardening effect. To investigate this effect the factorisation of the attenuation coefficient is best selected so that simple materials can be introduced for calibration. Thus, rather than use the photoelectric / Compton representation, the water / aluminium equivalent thickness method (section 1.2.2) is preferred in the following analysis. Equations 1.11 and 1.12 have been rewritten using the water / aluminium representation :

$$I_1 = \int S_1(E) \exp\{- t_w \ \mu_w(E) - t_{al} \ \mu_{al}(E)\} \, dE \qquad 1.46$$

$$I_2 = \int S_2(E) \exp\{- t_w \ \mu_w(E) - t_{al} \ \mu_{al}(E)\} \, dE \qquad 1.47$$

For monoenergetic sources at energies E_1 and E_2, equations 1.46 and 1.47 can be then simplified as two first order equations :

$$T_l = - \ln I_1 = t_w \mu_w(E_1) + t_{al} \mu_{al}(E_1) \qquad 1.48$$

$$T_h = - \ln I_2 = t_w \mu_w(E_2) + t_{al} \mu_{al}(E_2) \qquad 1.49$$

These equations can be solved directly for t_w and t_{al}. For polyenergetic sources used in diagnostic radiology, equations 1.48 and 1.49 should include higher order terms (a non-linear relationship exists between t_w, t_{al} and $\ln I_1$, $\ln I_2$) to compensate for the beam hardening effect. Four types of algorithms are known to solve equations 1.46 and 1.47. These are discussed in the following subsections.

1.6.1 Non-Linear Equations

Alvarez and Macovski (1976) approximated the high and low energy transmission (T_h and T_l) by a second order series of the two variables t_w and t_{al},

$$T_h = b_o + b_1 t_w + b_2 t_{al} + b_3 t_w t_{al} + b_4 t_w^2 + b_5 t_{al}^2 \qquad 1.50$$

$$T_l = c_o + c_1 t_w + c_2 t_{al} + c_3 t_w t_{al} + c_4 t_w^2 + c_5 t_{al}^2 \qquad 1.51$$

A calibration procedure is used to determine the coefficients b_i and c_i, $i=0,....,5$, by measuring T_h and T_l for a combination of various thicknesses of aluminium and water (Lehmann *et al* 1981). After the coefficients b_i and c_i are determined, equations 1.50 and 1.51 are solved using the Newton-Raphson method.

There are two major drawbacks in using the Newton-Raphson method to determine t_w and t_{al}. Firstly, one has to start with a solution close to the root of the equations, which may be difficult to achieve in practice to ensure convergence. Secondly, the necessity of calculating the Jacobian matrix and its inversion requires considerable computational effort.

1.6.2 Direct Approximation Method

Instead of using the Newton-Raphson iteration procedure, the results can be obtained by direct approximation (Brody *et al* 1981). The values t_w and t_{al} are expressed as a power series in T_h and T_l respectively :

$$t_w = d_o + d_1 T_h + d_2 T_l + d_3 T_h T_l + d_4 T_h^2 + d_5 T_l^2 + d_6 (T_h T_l)^2 + d_7 T_h^3 + d_8 T_l^3 \qquad 1.52$$

$$t_{al} = e_o + e_1T_h + e_2T_l + e_3T_hT_l + e_4T_h^2 + e_5T_l^2 + e_6(T_hT_l)^2 + e_7T_h^3 + e_8\,T_l^3 \qquad 1.53$$

As in the previous method, the coefficients d_i and e_i, i=0,1,....,8, are determined by a calibration procedure. Then t_w and t_{al} can be calculated directly from equations 1.52 and 1.53. This method allows a faster computation time but its accuracy requires further improvement (Chuang and Huang 1988).

1.6.3 Subregion Direct Approximation

The method described by Chuang and Huang (1988) divides the range of T_h and T_l into a number of subregions, each having its own beam hardening correction factors. So, for each paired data set (T_h,T_l) there corresponds a high energy subregion and a low energy subregion. Hence, t_w and t_{al} can be approximated by :

$$t_w = d_o + d_1T_h + d_2T_l + d_3T_hT_l + d_4T_h^2 + d_5T_l^2 \qquad 1.54$$

$$t_{al} = e_o + e_1T_h + e_2T_l + e_3T_hT_l + e_4T_h^2 + e_5T_l^2 \qquad 1.55$$

The set of coefficients (d_i and e_i) are computed using a least square fitting algorithm for all possible high and low energy subregion combinations and stored in computer memory.

The procedure of this method is : (i) determine which subregions T_h and T_l belong to, (ii) the corresponding set of coefficients is retrieved from computer memory, (iii) the values of t_w and t_{al} are calculated from equations 1.54 and 1.55 using these coefficients.

However, because only a discrete number of subregions are used, a discontinuity in t_w and t_{al} would exist between two adjacent subregions and therefore some sort of smoothing correction has to be made.

1.6.4 Iso-transmission Line Method

A given value of T_l corresponds to many possible thickness combinations of aluminium and water (t_w,t_{al}) (Chuang and Huang 1987). Thus, T_l can be represented by a linear equation of two variables t_w and t_{al} :

$$T_l = m\ t_w + n\ t_{al} \qquad 1.56$$

where m and n are the regression coefficients and are proportional to the total attenuation coefficients of water and aluminium at energy E_l, respectively. Similarly, T_h can be expressed as

$$T_h = r\ t_w + s\ t_{al} \qquad 1.57$$

where r and s are the regression coefficients.

Figure 1.4 Iso-transmission Lines for T_h and T_l.

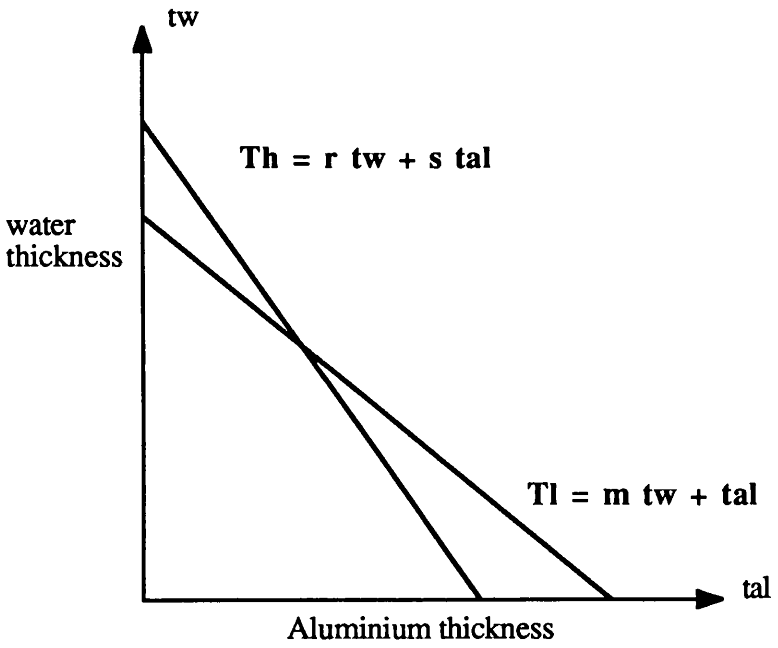

The desired water and aluminium thickness (t_w, t_{al}) for the pair (T_h, T_l) is at the intersection of the two iso-transmission lines (shown in figure 1.4), and can be calculated by solving equations 1.56 and 1.57.

Lookup tables can be constructed and stored in computer memory by assigning each value pair (T_h, T_l) the corresponding ordered pair (t_w, t_{al}). However, if the value of T_h or T_l is not already predefined, a correction which results in an interpolation to the closest predefined values has to be made.

Chuang and Huang (1988) showed that the subregion direct approximation and iso-transmission line method are computationally more efficient and more accurate than the non-linear and direct methods. However, these methods are more sensitive to quantum noise.

All of the methods mentioned so far require some kind of calibration procedure. This is time consuming and can easily lead to errors. Christ (1984) outlined an iterative procedure to take account of the changes to an x-ray spectrum as it is attenuated by an absorber for use in dual energy analysis. The only requirement of this procedure is the knowledge of the incident spectrum. The beam hardening correction method adopted during the dual energy analysis was based on this procedure. Full details of this method are given in the following section.

1.6.5 Iterative Procedure for Beam Hardening Correction

By combining equation 1.24 (definition of effective attenuation coefficient) and equation 1.26 (Alvarez and Macovski photoelectric / Compton representation) the effective linear attenuation μ_{eff} of a material can be expressed as :

$$\mu_{eff} = \int A_1 E^{-3} I_o(E)\, dE \Big/ \int I_o(E)\, dE \;+\; \int A_2\, F_{KN}(E)\, I_o(E)\, dE \Big/ \int I_o(E)\, dE \qquad 1.58$$

μ_{eff} can be used to describe the spectra absorbed by two detectors with different attenuation properties (cf. section 1.4), arising from a single x-ray spectrum, therefore

$$\mu_{1eff} = A_1\, p_1 + A_2\, s_1 \tag{1.59}$$

and

$$\mu_{2eff} = A_1\, p_2 + A_2\, s_2 \tag{1.60}$$

where

$$p_1 = \int I_{1o}(E)\, E^{-3}\, dE \,/ \int I_{1o}(E)\, dE, \quad s_1 = \int I_{1o}(E)\, F_{KN}(E)\, dE \,/ \int I_{1o}(E)\, dE$$

$$p_2 = \int I_{2o}(E)\, E^{-3}\, dE \,/ \int I_{2o}(E)\, dE, \quad s_1 = \int I_{2o}(E)\, F_{KN}(E)\, dE \,/ \int I_{2o}(E)\, dE$$

$I_{1o}(E)$ and $I_{2o}(E)$ can be either the absorbed spectra by detector 1 and detector 2 respectively as shown in figure 1.2a or the absorbed spectra arising from a single detector with pulse height analysis properties (figure 1.2b).

Combining equation 1.59 and equation 1.60 gives

$$A_1 = (\mu_{2eff}\, s_1 - \mu_{1eff}\, s_2) \,/\, (s_1\, p_2 - s_2\, p_1) \tag{1.61}$$

and

$$A_2 = (\mu_{1eff}\, p_2 - \mu_{2eff}\, p_1) \,/\, (s_1\, p_2 - s_2\, p_1) \tag{1.62}$$

If A_1 and A_2, for which the four constants p_1, p_2, s_1 and s_2 are known (assuming that the energy spectrum of the incident radiation is known), could be measured without beam hardening, then the correct value of A_1 and A_2 could be obtained. However, due to the beam hardening effect, μ_{eff} can only be accurately measured for a very small thickness of material x_m, as expressed in the following equation :

$$\mu_{eff} = \lim_{x_m \to o} \; 1 / x_m \;\; \ln \left\{ \int I_o(E)\, dE / [\, I_o(E) \exp(-\mu_m(E)\, x_m)\, dE \,] \right\}$$

$$\mu_{eff} = \int \mu_m(E)\, I_o(E) / \int I_o(E)\, dE \qquad 1.63$$

In the realistic case of a finite material thickness, equation 1.63 is no longer valid. In order to correct for beam hardening an iterative procedure, as described by Christ (1984), was used to determine the "true" values of the dual energy coefficients A_1 and A_2 of this material. The procedure is as follows (for ease of discussion the superscript i will indicate the number of the iteration step) :

i) The measured effective attenuation coefficient $\mu_{1eff}{}^o$ and $\mu_{2eff}{}^o$ are obtained using equation 1.38 and equation 1.39 respectively (section 1.5) from the dual energy analysis. From these values the first approximations of $A_1{}^o$ and $A_2{}^o$ are obtained using equations 1.61 and 1.62.

ii) The first approximation values of $A_1{}^o$ and $A_2{}^o$ are now used to calculate $\mu_{eff}{}^o(E)$ according to

$$\mu_{eff}{}^o(E) = A_1{}^o\, E^{-3} + A_2{}^o\, F_{KN}(E) \qquad 1.64$$

and from there a first calculated approximation for

$$\mu_{cal}{}^1(E) = 1 / x_m \;\; \ln \left\{ \int I_o(E)\, dE / [\, I_o(E) \exp(-\mu_{eff}{}^o(E)\, x_m)\, dE \,] \right\} \qquad 1.65$$

is obtained .

iii) As a first correction, the difference between the measured and calculated values is added to the measured values, i.e.

$$\mu_{eff}{}^1 = \mu_{eff}{}^o + (\mu_{eff}{}^o - \mu_{cal}{}^1) = 2\mu_{eff}{}^o - \mu_{cal}{}^1 \qquad 1.66$$

When μ_{1eff}^1 and μ_{2eff}^1 are substituted into equations 1.61 and 1.62 the second approximations A_1^1 and A_2^1 are obtained. These are then substituted into equations 1.64 and 1.65 to calculate μ_{cal}^2.

iv) This procedure is then repeated starting from

$$\mu_{eff}^2 = 2\mu_{eff}^1 - \mu_{cal}^2 \qquad 1.67$$

until a difference no longer exists between the measured μ_{eff}^o and calculated μ_{cal}^i of step number i. This indicates that the correct values of A_1 and A_2 have now been used in equation 1.64. The convergence of this iteration is provided by the fact that the correction of the linear attenuation coefficient diminishes as the calculated μ_{cal}^i values come close to the measured values.

In order to assess the validity of the above procedure, the effect of material thickness upon the measurement of the dual energy coefficients A_1 and A_2 was considered using aluminium as the test material. Aluminium was chosen because it is in the upper range of atomic numbers found in the human body and will show the greatest effect. The change in A_1 and A_2 for Aluminium, computed for an 80 kVp spectrum as given by Birch *et al* (1979) and a 10 cm water phantom, are plotted in figures 1.5 and 1.6 over a range of aluminium thicknesses from 10 to 20 mm. Values are plotted for uncorrected and corrected procedures where the corrections used are based on equations 1.64 to 1.67. These figures show that when the non-linearities introduced by beam hardening are not corrected for, the system appears to be sensitive to the material thickness; there is a 20% change in A_1 and about 7% change in A_2 across the aluminium thickness range. When the correction of beam hardening using the iterative procedure is employed the variation in A_1 and A_2 are reduced to about 5% and 3% respectively.

Figure 1.5 Beam Hardening Effect for A_1

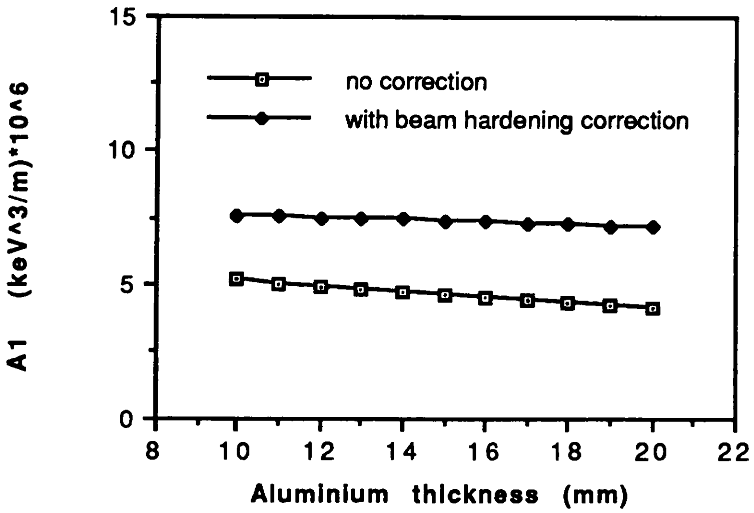

Figure 1.6 Beam Hardening Effect for A_2

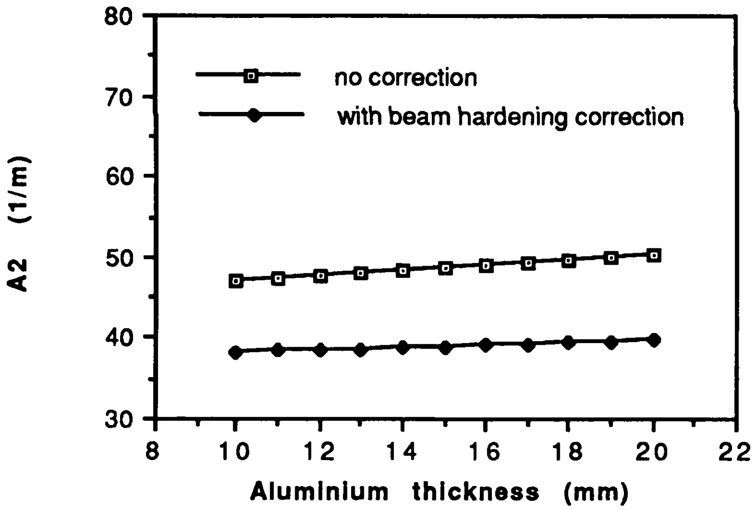

The "no correction" method shows that not only is the value of A_1 underestimated (or overestimated in the case of A_2) but also its non-linear property will reduce the sensitivity of dual energy analysis as it will not allow materials to be uniquely characterized. However, the magnitude of this effect will decrease for lower atomic numbers.

1.7 Clinical application

A wide range of clinical applications of dual energy systems are already being investigated or are in the process of being introduced into clinical routine. Some examples were given in section 1.3.

Clinical examinations require fast results. Limited availability of specialised medical examiners as well as the patients' convenience prohibit frequent recall for further tests. Consequently, the decision whether to continue or repeat a current examination has to be taken immediately. Digital techniques provide the means for fast, efficient data collection and rapid processing of measured raw data. Therefore, the need for a dual energy system capable of real time examination is the answer to the problem.

The dual energy probes described in section 1.6 could be used for real-time localised tissue characterization during a fluoroscopic procedure. In this case, probe positioning could be achieved simply by watching the movement of the dual energy probe across the patient's body on the TV-monitor of the image intensifier system. The dual energy probes will provide quantitative measurements related to the atomic number and density of the material under consideration. This information can easily be digitised, fed to a computer for rapid dual energy analysis and visualised on a display unit almost immediately.

The focus of this thesis is based upon the potential clinical application of dual energy probes to gallstone analysis. Our aim was to consider this analysis *in vitro* as a first step towards a future study with patients. The phantoms used in this study represent an anatomical cross-section of the body in the region of the gallbladder. Two types of phantoms with different thicknesses were used to simulate the diversity of tissues in the human body and their shapes; 10 to 20 cm of water (chapter 2 and 3) and 10 to 15 cm of perspex (chapter 4 and 5). Perspex was chosen because of its solid state that enabled certain practical measurement to be made.

Section 1.7.1 gives a brief introduction to gallstone disease in order to gain a better understanding of why its analysis is important. The composition and classification of gallstones are discussed in section 1.7.2.

1.7.1 Gallstone Disease

Gallstones are a common medical problem worldwide. They occur in about 8 to 10% of the world's population, and roughly one quarter of these people will eventually develop symptoms at some point in their lives (Siemens Review 5/88). Gallstone surgery has been the traditional treatment. But for most people, surgery is an undesirable solution, expensive, and it can result in a variety of complications especially as patients grow older. Non surgical treatments include pharmacologic or chemical dissolution, and more recently lithotripsy combined with dissolution therapy. However, the chemical therapy lasts for months, and in addition does not work on salted based gallstones (with calcium). Therefore, distinguishing between different type of gallstones could prove extremely useful. Furthermore, even the newly developed lithotripters have only been successful in 90% of patients when the dissolution agents are given for one year, resulting in 10% of patients undergoing subsequent surgery. In conclusion, a method which can identify the type of gallstone before hand, could prove essential to determine the choice of the treatment course. For this reason, an investigation using dual energy probes for gallstone analysis was carried out.

1.7.2 Composition and Classification of Gallstones

The analysis and classification of gallstones present special problems as gallstones contain major amounts of noncrystalline bile pigment, which has been difficult to study. The presence of pigment obscures important features of crystalline components on both gross and microscopic examination.

Table 1.4 lists the common analytical methods with their advantages, disadvantages and sensitivities (Edwin and Prien 1989). It should be noticed that most are not *in vivo* methods. The crystallographic methods have greatly improved gallstone analysis. X-ray diffraction and infrared spectroscopy utilise the same starting material, namely crushed but otherwise unaltered stone.

X-ray diffraction measures the interplanar spacings between like atoms in the crystalline array and provides a unique result for every crystalline substance. However, since some pigments are calcium bilirubinate which are sometimes noncrystalline, they might not be detected.

Table 1.4 Methods of Analysis of Gallstones.

Methods of analysis	Advantages	Disadvantages	Sensitivity
Morphological inspection	Simple : cholesterol stones are white or tan and pigment stones are dark brown or black	Overestimates pigment cannot see calcium	-
Radiograph	Widely available	Both cholesterol and pigment are radiolucent and not appreciated without contrast	-
Chemical	"Historical"	Insoluble residue. In pigmentstones as much as 66% of the dry weight remains insoluble	-
X-ray diffractometry	Very specific	Requires crystallinity. Very expensive	5-10%
Infrared spectroscopy	Specific	Mixture of similar compounds a problem. Expensive	5-10%

In infrared spectroscopy, the sample is irradiated with a spectrum of infrared that induce the molecular bonds to vibrate at characteristic frequencies. The result is presented as elemental information rather than in compounds. According to Edwin and Prien (1989) however, this method suffers from the study of mixtures of similar compounds. If the component is dispersed throughout the stone below the 10% level, it will not be detected.

In table 1.5, the common gallstone components are shown in order of decreasing abundance (Edwin and Prien 1989). Also comment on the radiodensity of each component as seen on a radiograph is made.

Table 1.5 Gallstone Components

	OPAQUE / LUCENT
Cholesterol monohydrate	L
Pigment : calcium bilirubinate (brown)	L
bilirubinate polymers (black)	L
Calcium carbonate : vaterite	O
calcite	O
aragonite	O
Calcium phosphate : apatite	O
Calcium palmitate	L
Others : e.g. bilirubin, bile pigments	L

The nomenclature defines the gallstone types into three major categories, namely cholesterol, black pigment and brown pigment. Each type may be further subdivided according to the presence or absence of the radiopaque calcium salts. As an example, table 1.6 shows the composition and type of gallstones (Trotman *et al* 1977) provided by a study of 72 sets collected over several years from the gallbladder of patients in the United States and Japan. The main conclusion drawn from this table is that cholesterol stones contain very little pigment, and black pigment stones contain little cholesterol.

Table 1.6 Composition and Type of Gallstone

	Gallbladder		
	Cholesterol (USA n*=31)	Black pigment (USA n*=25)	Brown pigment (JAPAN n*=16)
Cholesterol	85.2 ± 1.9	2.1 ± 1.0	10.9 ± 1.8
Pigment	0.5 ± 0.07	34.4 ± 3.1	62.8 ± 6.8
Total calcium	1.5 ± 0.6	9.4 ± 1.3	5.9 ± 0.3
Total measured	89.4 ± 1.5	63.7 ± 3.6	103.0 ± 3.9

*n - number of patients

The background to the work carried out for this thesis has been described. Dual detector systems are to be investigated, both theoretically and experimentally, for use in tissue characterization of small regions that are seen during a fluoroscopic procedure. A simplified dual energy analysis is used and corrected for beam hardening using an iterative procedure. The theoretical simulation of the system is described in chapter 2 and the experimental work in chapter 3. The effect of scattered radiation on the dual energy system is simulated both theoretically and experimentally in chapter 4. Finally, chapter 5 considers the *in vitro* analysis of gallstones.

CHAPTER 2 DUAL ENERGY DETECTORS- Basic Design Considerations and Narrow Beam Simulation

The design of the dual energy probe considered in section 1.5 offers two types of probes; the split detector probe and pulse height analysis (PHA) probe. In the following, each type is carefully studied in an attempt to find the optimum system for the split detector probe and the optimised energies for the PHA probe.

2.1 Split Detector Method

Having decided on the basic design of the split detector probe, as shown in figure 1.2a, a computer simulation of the dual energy system was carried out. This design offers three degrees of freedom :

i) the choice of material for scintillators 1 and 2 and for the filter.
ii) the choice of thickness of scintillators 1 and 2 and for the filter.
iii) the choice of the incident x-ray spectrum.

The choice of scintillation and filter materials is determined by their beam hardening properties and commercial availability. The thicknesses of the materials are governed by intensity considerations, efficiency and total energy peak Compton ratio. The x-ray spectra available are limited to a useful clinical range of 70 to 90 kVp.

In order to optimise these parameters a narrow beam attenuation computer model, described fully in section 2.2.1, was used; transmitted and absorbed spectra were computed at selected points in the detector system for a range of detector and examination parameters and from these the absorption efficiency and tissue characterization sensitivity were calculated. This program was run on an Apple IIe minicomputer. The limitation of this model is that it assumes narrow beam attenuation and good geometry and therefore the effect of scattered radiation is not taken into account. Experimental verification of this model was carried out in chapter 3 and the effect of scattered radiation was studied using a Monte Carlo model described in chapter 4.

2.1.1 Narrow Beam Attenuation Computer Model

A diagram of the model used to describe the split detector system is shown in figure 2.1. A similar model has been used by Horrocks (1987) for the design of a dual energy ionography detector system. The theory is given in the remainder of this section and section 2.1.2. Throughout the whole system narrow beam attenuation of the x-ray spectrum incident on the detector was assumed. The transmitted x-ray spectrum was then computed at different parts of the detector system as represented in figure 2.1 using the exponential relation :

$$N_e(E) = N_i(E) \exp(- \mu_m(E)\, x_m)$$

where $N_i(E)$ is the number of incident photons of energy E, $N_e(E)$ is the number of emerging photons of energy E, $\mu_m(E)$ is the linear attenuation coefficient of respective material m and x_m is the the thickness of respective material m. Each material in the detector system is described by its total mass attenuation coefficients, its physical density and its thickness.

Six different commercially available scintillation detectors were considered: a plastic scintillator, NE102A, and five types of inorganic crystalline scintillators; sodium iodide (NaI), caesium iodide (CsI), zinc tungstate ($ZnWO_4$), calcium fluoride (CaF_2) and bismuth germanate ($Bi_4Ge_3O_{12}$). Copper, zinc and tin were investigated as filter materials. Attenuation data for the elements were obtained from Storm and Israel (1970), and tabulated at intervals between 10-150 keV. Curves were fitted to the data using a computerised least square fitting procedure published by Ruckdshel (1981). Absorption edges were included in the fitting procedure. Materials that had an absorption edge in the

Figure 2.1 Narrow Beam Attenuation Computer Model

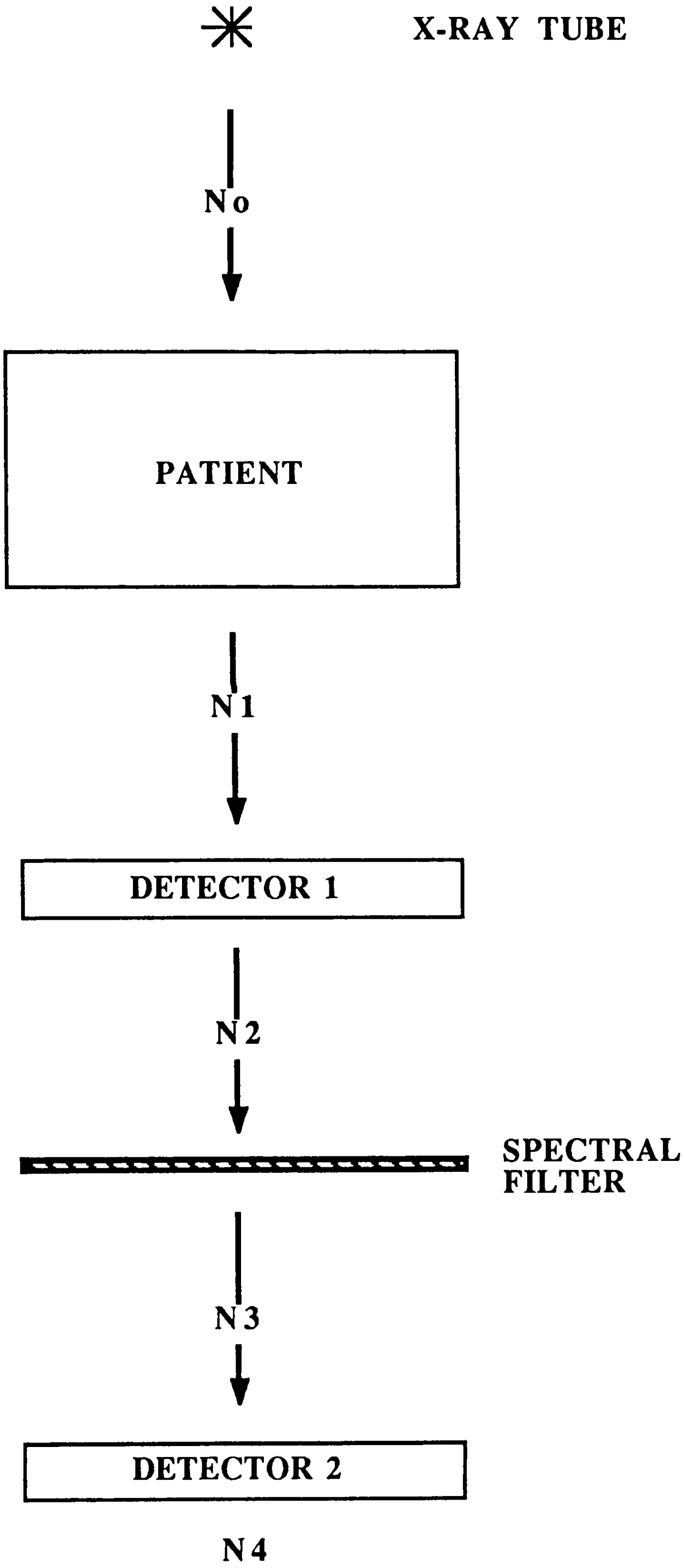

relevant energy range were fitted separately above and below the absorption edge. Values of the attenuation coefficient were taken from the fitted curve at 1 keV intervals from 10 to 90 keV. The attenuation coefficients for compounds were computed from elemental data using the mixture rule (equation 1.5). Data for the x-ray spectra were obtained from Birch *et al* (1979) for peak kilovoltages of 70, 80 and 90 kVp for an x-ray tube with a tungsten target at 17° and an inherent filtration of 2 mm Al. The input spectrum was in the form of numbers of photons in energy intervals of 1 keV from 10 keV to the maximum energy. Some physical constants of detector materials and filters are given in table 2.1.

Table 2.1 Physical Constants of the Detector Materials and Filters

Material	Density (kg/m^3)	L- edge (keV)*	K-edge (keV)*
NEA102A	1032	-	-
NaI	3670	-	33.0
CsI	4510	-	33.0, 36.0
CaF_2	3170	-	-
$ZnWO_4$	7620	10.2, 11.5, 12.1	69.5
$Bi_4Ge_3O_{12}$	7130	13.4, 15.7, 16.4	11.1, 90.5
Cu	8960	-	9.0
Sn	7310	-	29.2
Zn	7140	-	-

*between ~10 keV and ~90 keV

2.1.2 Criteria to Decide Best Combinations for Split Detector System

The optimum combinations of scintillators and filters were selected by considering the absorption efficiencies of the two detectors and the dual energy sensitivity of the system. These parameters are described below.

i) Absorption Efficiency

The efficiency of each individual detector element was defined as the ratio of the energy deposited in the active detecting material to the incident spectrum on the split detector probe (figure 2.1) :

$$\eta_1(\%) = \{ \Sigma N_1(E) - N_2(E) \} \ / \ \Sigma N_1(E) \qquad 2.1$$

$$\eta_2(\%) = \{ \Sigma N_3(E) - N_4(E) \} \ / \ \Sigma N_1(E) \qquad 2.2$$

where η_1 and η_2 are the absorption efficiencies of detector 1 and detector 2 respectively. The absorption efficiency of the second detector is calculated by dividing the energy absorbed in detector 2 over the spectrum incident upon the dual energy probe rather then the spectrum directly incident on detector 2. For detector 2, this is not the conventional definition of detector efficiency, however, such a definition enables the correct comparison of the two detector efficiencies when considered as a dual energy detector.

For a given intensity the absorption efficiency dictates the signal noise. As the system will be dominated by the noisiest detector, the absorption efficiencies of both detectors should be matched in order to minimise the total noise present in the split detector system.

ii) Dual Energy Sensitivity

A more careful study of the dual energy analysis discussed in section 1.5 will show that the detectability of the material under investigation will depend strongly on the photoelectric effect whereas the change in the Compton coefficient over the energy considered would be relatively small in comparison. As the incident x-ray beam passes through the detector system, the photon energy spectrum is significantly altered. If the effective energy of the absorbed spectrum, E_{eff}, in both detector elements is computed using equation 1.18, the energy separation between the two detector elements can be found. A wider separation between these effective energies would be reflected by a greater sensitivity in differentiating between atomic numbers. The dual energy sensitivity (DES) was defined as :

$$DES = E_{eff2} - E_{eff1} \qquad 2.3$$

where E_{eff1} and E_{eff2} are the effective energies of the spectra absorbed by detector 1 and detector 2 respectively. Thus, the DES of a particular system is governed by the type and dimension of detectors and filters, the incident spectrum and the phantom thickness.

2.1.3 Results from the Narrow Beam Attenuation Computer Model

Two main groups of split detector combinations were considered; plastic scintillators and inorganic crystalline detectors. The plastic scintillator consisted of NEA102A as first and second detector. The various crystalline combinations always comprised a 25.4 mm NaI scintillator as second detector. The second detector should attempt to stop all remaining photons otherwise information could be lost.

Only restricted results will be presented but they have been chosen as optimum dimensions in that category. The features that dictate optimum performance are;

i) commercial availability of material in the required thickness,

ii) compactness of the dual detector probe to ensure minimum weight and so allow ease of movement,

iii) position of absorption edges so that the desired energy separation caused by beam hardening effect is obtained, and;

iv) the absorption efficiency and dual energy sensitivity of the dual energy system.

a) The Plastic Scintillator NE102A

Plastic scintillators are easy to machine to almost any shape desired and can be purchased cheaply. These features make plastic preferable where high efficiency and high light output are not essential. In the diagnostic x-ray energy range the plastic scintillator's efficiency is sufficient and its low light output can be increased by the use of high gain photomultiplier tubes. It is therefore a detector worth of consideration.

The flat shape of the NE102A's attenuation curve from figure 2.2 proves that the plastic scintillator is not capable of hardening a spectrum sufficiently by the split detector method. In fact the effective energy of the absorbed and transmitted spectra for a 20 mm NE102A differ by only 1.25 keV. Consequently, a filter between the two scintillators is essential. The optimised results for the selection of the scintillator / filter / scintillator system are presented in table 2.2.

Table 2.2 Results from the NE102A Detector

1^{st} detector = 7.0 mm NE102A
2^{nd} detector = 50.0 mm NE102A
water phantom = 10 cm

filter	kVp	η_1(%)	η_2(%)	E_{eff1} (keV)	E_{eff2} (keV)	DES (keV)
1.0 mm Cu	70	14.0	5.1	42.26	54.61	12.35
	80	13.6	7.9	45.21	59.32	14.10
	90	13.3	10.2	47.71	63.27	15.60
1.0 mm Zn	70	14.0	7.0	42.26	53.68	11.42
	80	13.6	10.0	45.21	58.10	12.90
	90	13.3	12.6	47.71	61.65	13.90
0.3 mm Sn	70	14.0	5.3	42.26	51.85	9.60
	80	13.6	8.1	45.21	57.70	12.50
	90	13.3	10.5	47.71	61.90	14.20

Figure 2.2 Attenuation Curve for NE102A

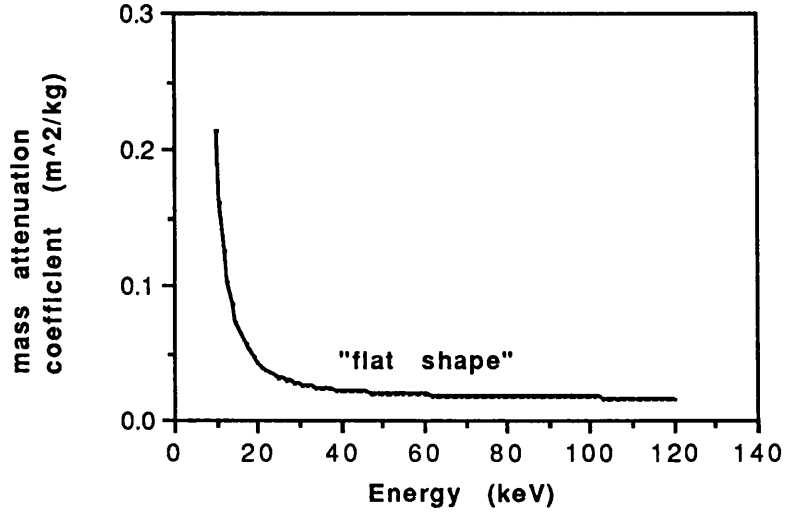

b) The Crystal Scintillator Bismuth Germanate $Bi_4Ge_3O_{12}$

The high attenuation properties of the $Bi_4Ge_3O_{12}$ scintillator prohibit the use of an additional filter due to most of the incident photons being stopped before reaching the second detector. The location of the L-absorption edge (figure 2.3) of $Bi_4Ge_3O_{12}$ favoured the attenuation of the low energy part of the spectrum. This fact results in reasonable beam hardening at 70, 80 and 90 kVp. However the high K-absorption edge at about 90 keV opposes the beam hardening effect at higher kVp values. Results for $Bi_4Ge_3O_{12}$ are presented in table 2.3.

Table 2.3 Results from the $Bi_4Ge_3O_{12}$ Detector

1^{st} detector = 0.5 mm $Bi_4Ge_3O_{12}$

2^{nd} detector = 25.4 mm NaI

water phantom = 10 cm

filter	kVp	η_1(%)	η_2(%)	E_{eff1} (keV)	E_{eff2} (keV)	DES (keV)
none	70	89.4	10.6	42.5	54.2	11.7
	80	84.1	15.9	45.0	58.7	13.7
	90	79.5	20.5	47.0	63.0	16.0

Figure 2.3 Attenuation curve for $Bi_4Ge_3O_{12}$

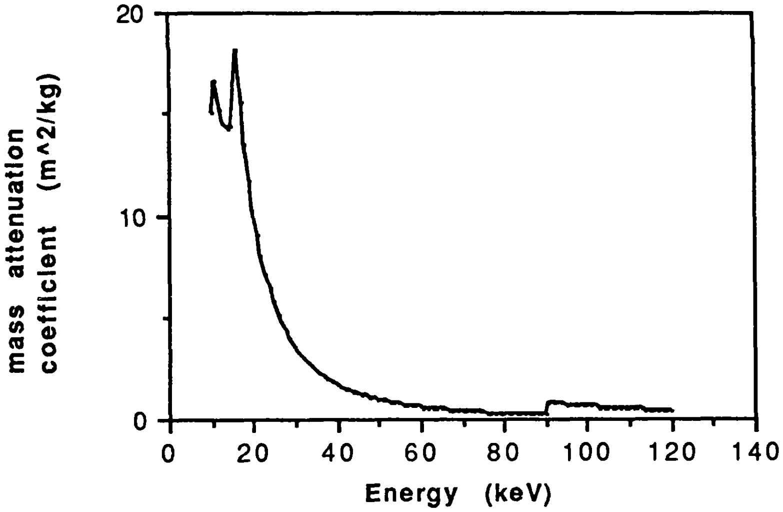

c) The Crystal Scintillator Calcium Fluoride CaF_2

The smooth shape of the CaF_2 attenuation curve (figure 2.4) without intervening absorption edges and the relatively high attenuation at low energies result in good beam hardening properties. The low effective atomic number of CaF_2 requires a relatively large thickness for the optimised crystal. The use of a filter is not required in these combinations. CaF_2 has already been used successfully in Brook's dual energy CT system (Brooks 1981). Results for CaF_2 are given in table 2.4.

Table 2.4 Results from the CaF_2 Detector

1st detector = 5.0 mm CaF_2
2nd detector = 25.4 mm NaI
water phantom = 10 cm

filter	kVp	η_1(%)	η_2(%)	E_{eff1} (keV)	E_{eff2} (keV)	DES (keV)
none	70	69.0	31.0	41.4	49.5	8.1
	80	63.1	36.9	43.7	56.5	9.8
	90	58.8	41.2	45.6	56.5	10.9

Figure 2.4 Attenuation curve for CaF_2

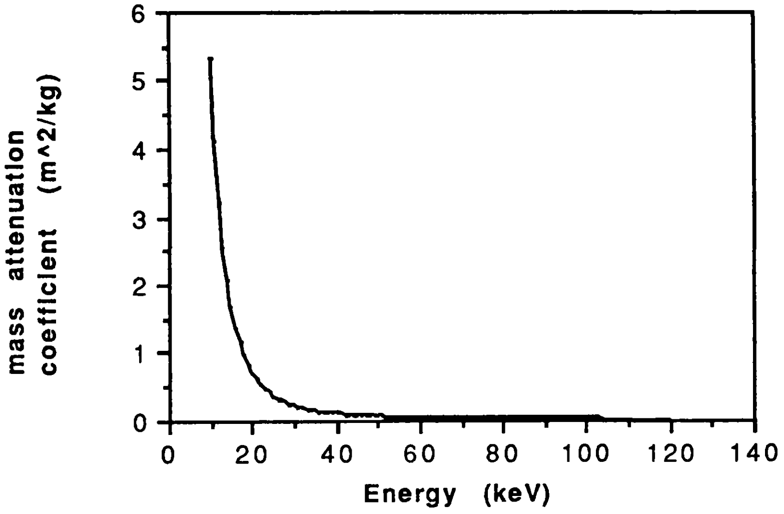

d) The Crystal Scintillator Caesium Iodide CsI

The relatively high absorption edges between 30 keV and 40 keV of CsI imply superior beam hardening properties. However, the high attenuation coefficient of CsI requires a very thin layer of crystal to allow most of the high energy photons to be transmitted. Results for CsI are given in table 2.5. A copper filter is added to the dual energy probe to increase the effective energy of the absorbed spectrum by the NaI detector.

Table 2.5 Results from the CsI Detector

1st detector = 0.25 mm CsI
2nd detector = 25.4 mm NaI
water phantom = 10 cm

filter	kVp	η_1(%)	η_2(%)	E_{eff1} (keV)	E_{eff2} (keV)	DES (keV)
0.3 mm Cu	70	77.2	11.1	42.6	53.3	10.6
	80	71.3	16.6	44.9	58.2	13.3
	90	66.4	21.3	46.7	62.3	15.6

Figure 2.5 Attenuation curve for CsI

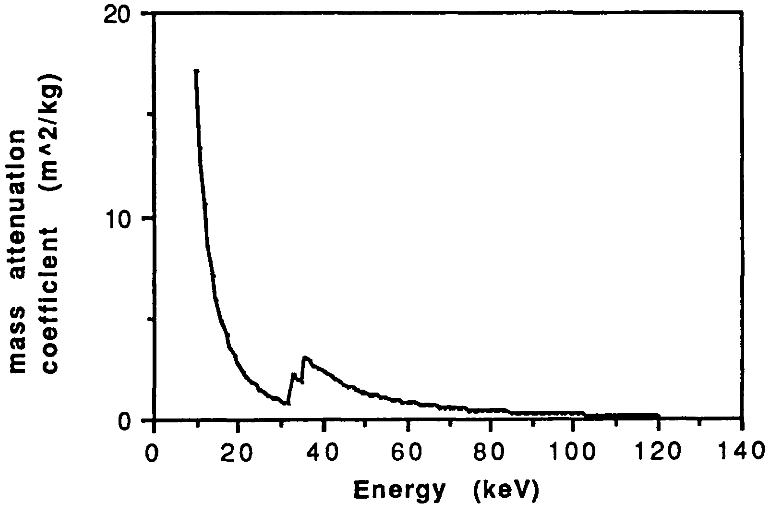

e) The Crystal Scintillator Sodium Iodide NaI

High quantum efficiency, high light output and low costs make NaI the most popular scintillator detector. The attenuation coefficient of NaI is just slightly lower than that of CsI. Overall both scintillators show similar attenuation properties. The fragile mechanical properties of a NaI crystal, however, prevent its production in very thin layers as would be required for the first detector of the split detector system. The results of the simulation are shown in table 2.6

Table 2.6 Results from the NaI Detector

1st detector = 1.0 mm NaI
2nd detector = 25.4 mm NaI
water phantom = 10 cm

filter	kVp	η_1(%)	η_2(%)	E_{eff1} (keV)	E_{eff2} (keV)	DES (keV)
none	70	96.6	3.4	43.2	49.3	6.1
	80	93.9	6.1	46.0	57.7	11.6
	90	91.0	9.0	48.4	63.5	15.2

Figure 2.6 Attenuation Curve for NaI

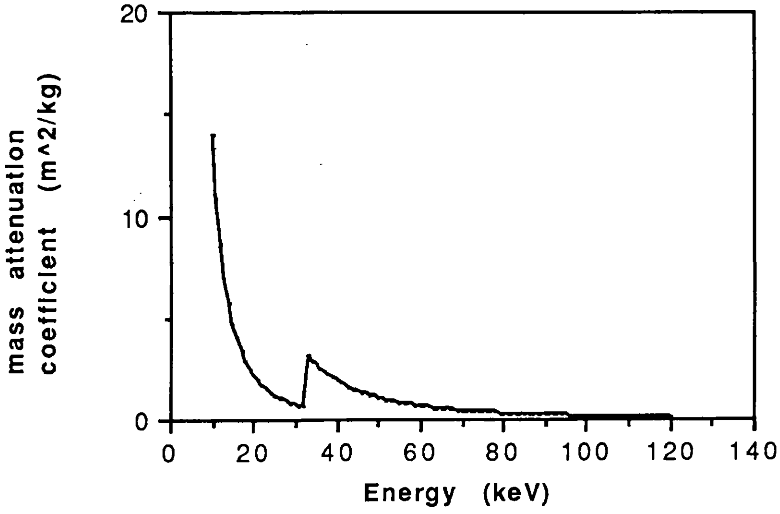

f) The Crystal Scintillator Zinc Tungstate $ZnWO_4$

$ZnWO_4$ shows similar attenuation properties as $Bi_4Ge_3O_{12}$. However, since its absorption edges (~70 keV) lie lower than those of $Bi_4Ge_3O_{12}$ a reduction of the desired beam hardening effect at high kVps will result. Results for $ZnWO_4$ are given in table 2.7.

Table 2.7 Results from the $ZnWO_4$ Detector

1st detector = 0.5 mm ZnWO4
2nd detector = 25.4 mm NaI
water phantom = 10 cm

filter	kVp	η_1(%)	η_2(%)	E_{eff1} (keV)	E_{eff2} (keV)	DES (keV)
none	70	81.7	18.3	42.0	52.2	10.2
	80	78.3	21.6	44.8	55.0	10.1
	90	77.2	22.8	47.5	57.3	9.8

Figure 2.7 Attenuation curve for $ZnWO_4$

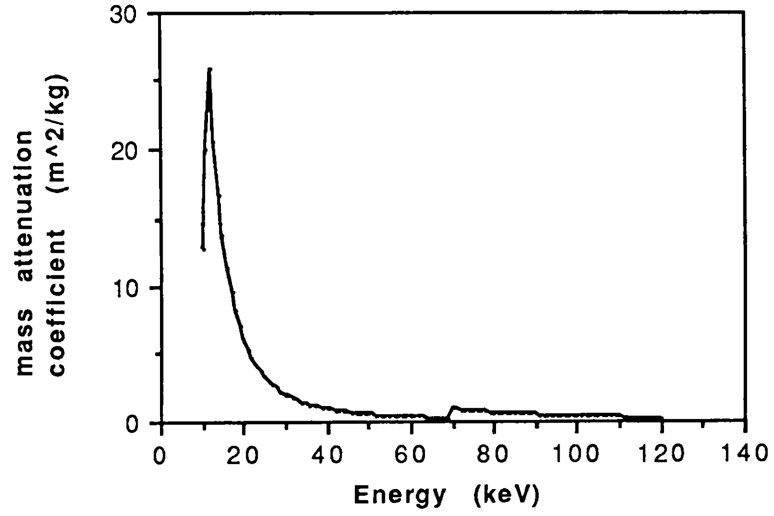

g) Conclusion

The results from the narrow beam attenuation simulation for nine different detector / filter / detector combinations were presented considering the absorption efficiencies and the DES. These conclusions refer to the results in tables 2.2 to 2.7.

i) Absorption efficiency of detector 1 .

Ideally the thickness of detector 1 should be determined such that its efficiency is approximately 50%. In this way both detector efficiencies could be matched. Unfortunately, in most instances the choice in practice is limited by the commercial availability of the desired size of the scintillator and its attenuation properties. As expected with a plastic scintillator, the NE102A efficiency is very low, being about 14% at 70 kVp and decreasing with higher kVp. Apart from the plastic scintillator, the efficiency of detector 1 is well above 50%. For an experimental implementation of the split detector probe the use of $Bi_4Ge_3O_{12}$ or $ZnWO_4$ as the first detector has to be ruled out because of the cut-off of the high energy part of the transmitted spectrum caused by high K-absorption edges. The efficiency of both $Bi_4Ge_3O_{12}$ and $ZnWO_4$ are well above 80%. The mechanical properties of NaI prohibits a very thin layer from being used. Even a 1 mm thick NaI crystal has an efficiency in excess of 96% thus stopping most of the transmitted spectrum. The nearest possible combination of all the scintillators considered to the ideal case is provided by CaF_2 and CsI detectors.

ii) Absorption efficiency of detector 2.

In all the combinations considered for the split detector method, the absorption efficiency of detector 2 drops due to the beam hardening effect caused by the reduction of the total intensity incident on detector 2 and by the eventual insertion of a filter. The plastic scintillator split detector probe shows similar performance with each of the combinations tested. Its absorption efficiency (detector 2) was very poor, being below 10.5% in all cases. Any inadequacy in the efficiency of detector 2 could be overcome by increasing its depth.

iii) Dual energy sensitivity.

The DES has a value of 8 to 16 keV and in most cases increases when the kVp changes from 70 to 90, except for the case of the $ZnWO_4$/NaI combination where the DES decreases due to the high absorption edge of $ZnWO_4$. The plastic dual energy probe, the $BiGe_3O_{12}$/NaI and the CsI/Cu/NaI combinations show very similar sensitivity, whilst the CaF_2/NaI, NaI/NaI and $ZnWO_4$/NaI combinations are shown to have lower DES at almost all kVps considered.

In summary, the plastic scintillator combination has limited application due to the very low absorption efficiency of both detectors. Of the crystal scintillator combinations only CaF_2/NaI and CsI/Cu/NaI have efficiencies that are sufficiently well matched. Furthermore CaF_2 and CsI are commercially available at the required thicknesses. However, the larger DES shown by the CsI/Cu/NaI dual energy probe selects this combination to be the final choice for experimental evaluation.

2.1.4 The CsI/Cu/NaI Detector System

A dual energy calibration was simulated using the narrow beam attenuation computer model described in section 2.1.1. The purpose of this investigation was to give an indication of the dual energy response for different values of atomic number and also to form a theoretical data base for future comparison with an experimental study.

A test phantom was simulated by adding known materials of different thicknesses (0.1 mm, 0.4 mm, 0.7 mm, 1.0 mm) to a water phantom (figure 2.8). The atomic numbers of the calibration materials ranged from 6 to 30 and are given in table 2.8. Attenuation data for these materials were obtained from Storm and Israel (1970).

The absorbed spectrum in both detector 1 and detector 2 (i.e. CsI and NaI) was then computed for :

i) the x-ray path through the water phantom only - (for a measurement of background). This corresponds to $D_w(E_1)$ and $D_w(E_2)$, the absorbed integrated photon spectra at the respective effective energies E_1 and E_2, given by equation 1.36 (cf. section 1.5)

ii) the x-ray path through the water phantom and calibration material. This corresponds to $D_m(E_1)$ and $D_m(E_2)$, the intensities given in equation 1.32 at effective energies E_1 and E_2 respectively.

Table 2.8 Dual Energy Calibration Materials

Material	Z	density (kg/m^3)
Carbon	6	2250
Magnesium	12	1740
Aluminium	13	2700
Titanium	22	4500
Iron	26	7860
Copper	29	8920
Zinc	30	7140

In all cases the water phantom includes a fixed perspex thickness equal to 22.3 mm. This includes the thickness of both the perspex container and the perspex holder of the calibration materials. The perspex was added to simulate a more realistic approach to the experimental set up (cf. chapter 3). Therefore for :

i) detector 1

$$D_w(E_1) = \Sigma N_o(E) \exp(- \mu_w(E) x_w - \mu_p(E) x_p) \left\{1- \exp(- \mu_{d1}(E) x_{d1}) \right\}$$

$$D_m(E_1) = \Sigma N_o(E) \exp(- \mu_w(E) x_w - \mu_p(E) x_p - \mu_m(E) x_m)$$

$$\times \left\{1- \exp(- \mu_{d1}(E) x_{d1}) \right\}$$

Figure 2.8 CsI/Cu/NaI Detector System with Test Phantom

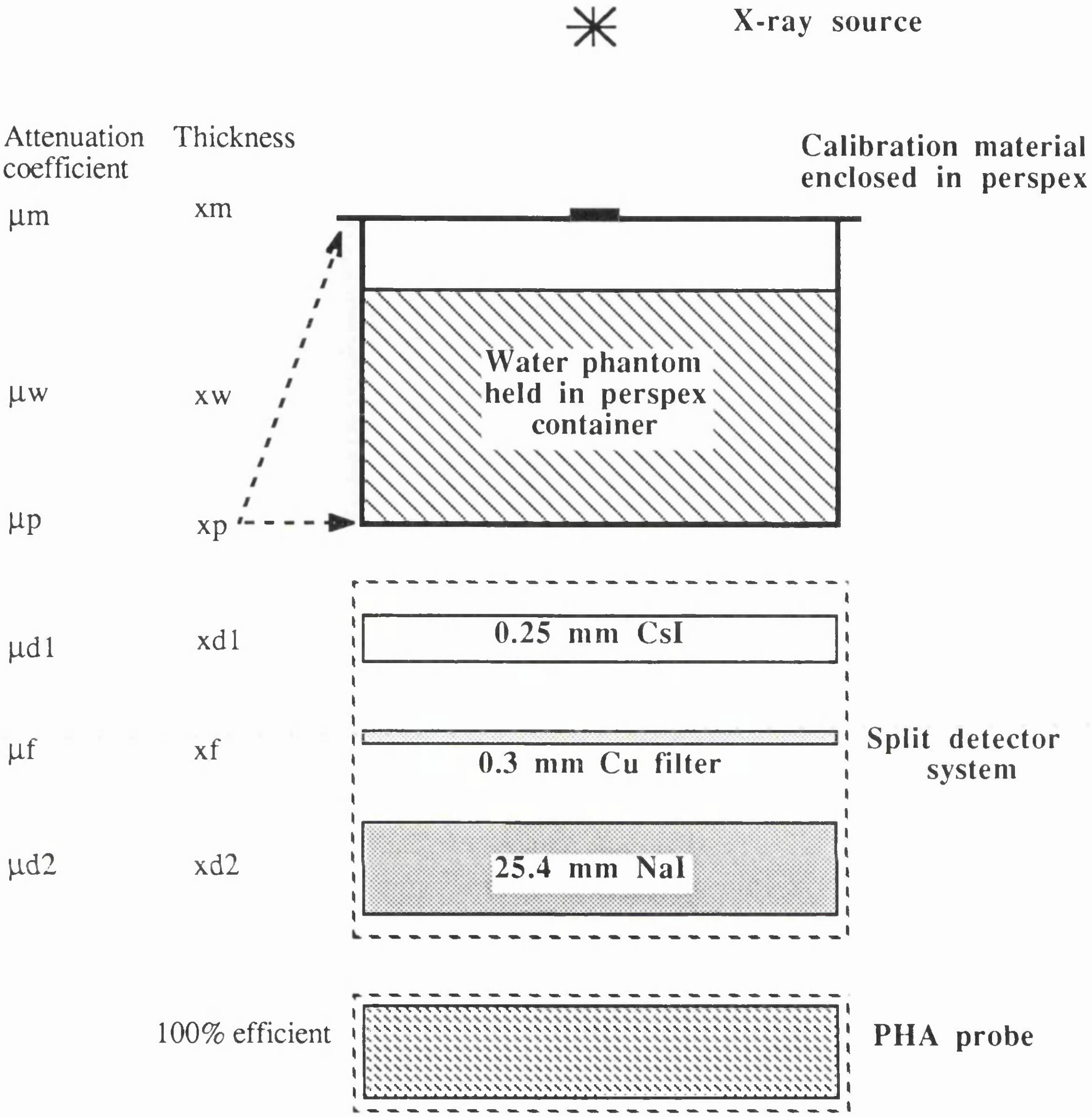

ii) detector 2

$$D_w(E_2) = \Sigma\, N_o(E) \exp(- \mu_w(E)\, x_w - \mu_p(E)\, x_p - \mu_m(E)\, x_m - \mu_{d1}(E)\, x_{d1} - \mu_f(E)\, x_f)\left\{ 1 - \exp(- \mu_{d2}(E)\, x_{d2}) \right\}$$

$$D_m(E_2) = \Sigma\, N_o(E) \exp(- \mu_w(E)\, x_w - \mu_p(E)\, x_p - \mu_m(E)\, x_m - \mu_{d1}(E)\, x_{d1} - \mu_f(E)\, x_f - \mu_m(E)\, x_m)\left\{ 1 - \exp(- \mu_{d2}(E)\, x_{d2}) \right\}$$

Then, using equations 1.42 and 1.43 (cf. section 1.5), the dual energy numbers A_1 and A_2 were determined. The results are shown in section 2.3.

2.2 Pulse Height Analysis Probe

Section 1.4 indicated that dual energy pulse height analysis (PHA) probes are regarded as dual detector probes even though they only utilise one physical detector. This is due to the fact that they are capable of measuring attenuation along one ray-path at two energies simultaneously. However, due to the versatility of PHA systems, a careful study has to be undertaken of the selection of energy windows in order to determine the optimum response to the dual energy system. In the following section different sets of windows (low and high energy) with 10 keV width are selected arbitrarily within a given range.

2.2.1 Window Selection

Different sets of windows were selected according to table 2.9. The effective energies E_1 and E_2 correspond to the mean value of the energy range of the selected low and high energy window respectively. Basically, the analysis is the same as in section 2.1.4 except for the following:

i) For background measurements, $D_w(E_1)$ and $D_w(E_2)$ correspond to the number of photons detected for a low and a high energy window respectively

ii) For mesurements including material, $D_m(E_1)$ and $D_m(E_2)$ correspond to the number of photons collected in the low and high energy windows respectively.

The results from this analysis are shown in figure 2.9. The value of A_1 was computed for a 10 cm water phantom, a 0.1 mm material thickness and a 70 kVp incident spectrum. A_1 was calculated according to the selected set of windows in table 2.9 for calibration materials ranging from Carbon (Z=6) to Zinc (Z=30). From figure 2.9 it can be seen that the combination of windows that gives the largest value of A_1 is the 10th set which corresponds to windows of 30-40 keV and 50-60 keV.

Figure 2.9 Values of A_1 for different sets of windows

a) A1 for C, Mg and Al

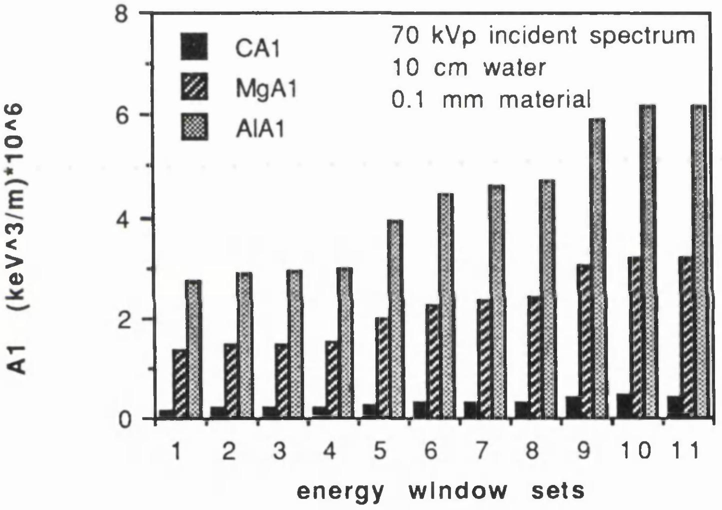

b) A1 for Ti, Fe, Cu and Zn

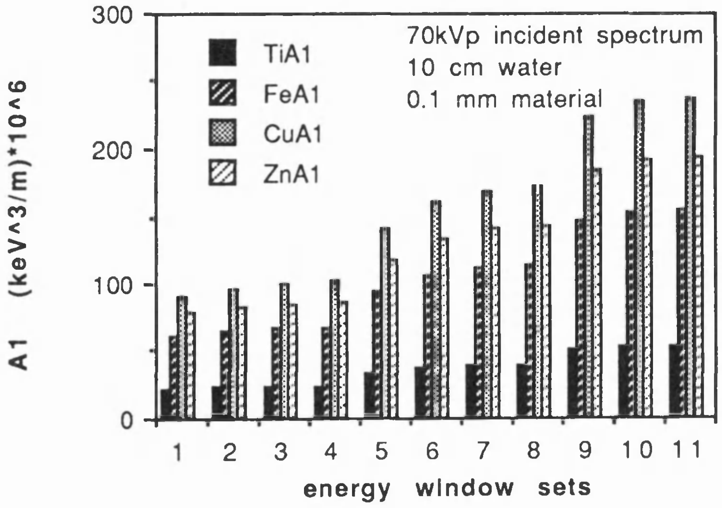

Table 2.9 Selected Sets of Windows

set	low energy window (keV)	high energy window (keV)
1	10-20	30-40
2	10-20	40-50
3	10-20	50-60
4	10-20	60-70
5	20-30	30-40
6	20-30	40-50
7	20-30	50-60
8	20-30	60-70
9	30-40	40-50
10	30-40	50-60
11	30-40	60-70

Although the 11th set (30-40 keV and 60-70 keV) shows similar behaviour to the one selected (figure 2.9), the decrease in the number of photons at high energies will lead to poor counting statistics and, therefore, will considerably increase the counting time in an experimental situation. This result might at first appear confusing. As the dual energy analysis is based on the strong material dependence of the photoelectric effect, one would believe that increasing the separation of energy windows would increase the senstivity of the dual energy probe. However, the spectral energy density must be considered. Figure 2.10 shows the transmitted spectra. It can be seen that a very low energy window has to be ruled out since most low energy photons are stopped by the water phantom. A very high energy window will not only have a poor counting statistic due to lack of photons but will also contribute little improvement to the atomic number separation (figure 2.9).

In the same manner, it was found that for 80 kVp and 90 kVp incident spectra the best window sets in both cases were 40-50 keV and 50-60 keV.

The results of calculations of A_1 and A_2 for the PHA probe using these windows are given in the following section.

Figure 2.10 Transmitted Spectra through Test Phantom

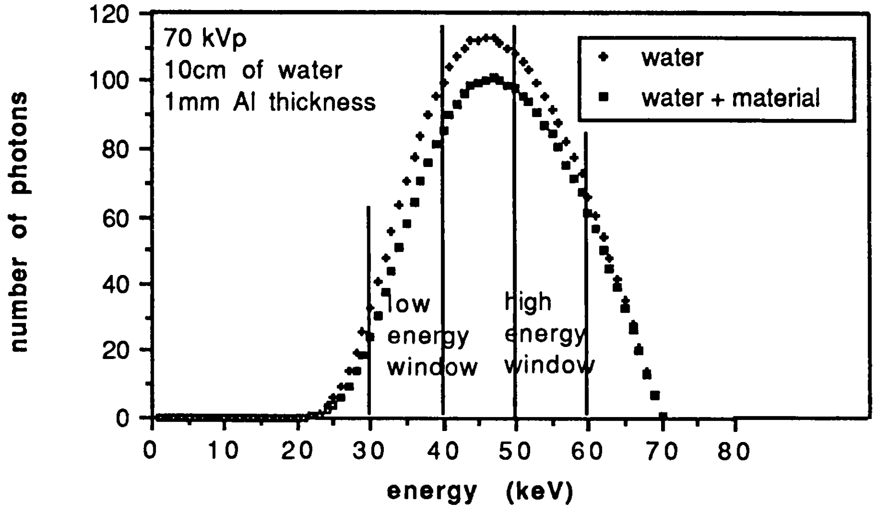

2.3 Determination of A_1 and A_2

Using equations 1.42 and 1.43, the dual energy coefficients A_1 and A_2 were determined for both the split detector probe and PHA probe for the following conditions:

i) Three different incident spectra, 70, 80 and 90 kVp;

ii) a range of calibration material thickness 0.1 mm, 0.4 mm, 0.5 mm, 0.7 mm and 1.0 mm

iii) a range of water phantom thickness 10, 15 and 20 cm.

2.3.1 Dependence on Incident Spectra

In figure 2.11 the values of the dual energy coefficients A_1 and A_2, corrected for beam hardening using the iterative procedure (cf. section 1.6.5), are computed for all calibration materials (table 2.8) for both types of dual energy probes. From figure 2.11a and figure 2.11b, it can be seen that the values of A_1 for the split detector probe are less

Figure 2.11 Dependence of A_1 and A_2 on Incident Spectra

a) Split detector method for A1

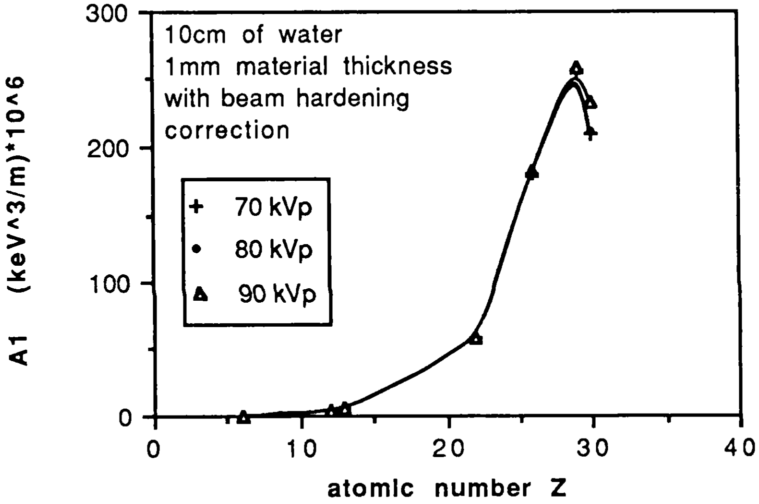

b) PHA method for A1

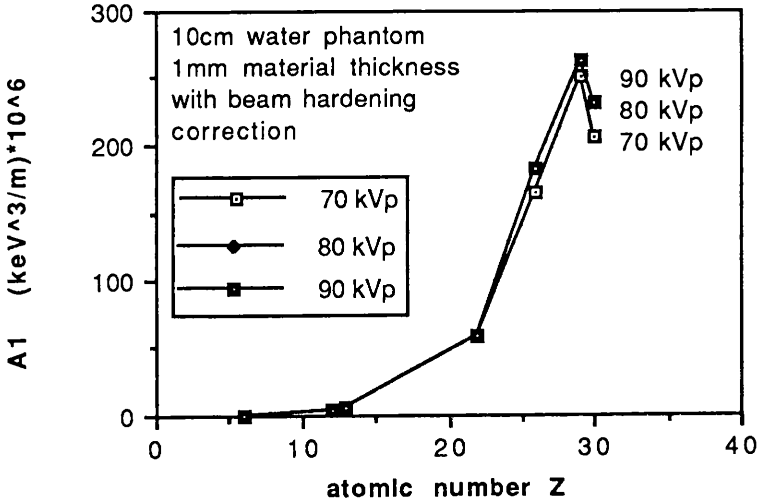

energy dependent at high atomic numbers (Fe, Cu, Zn) than the PHA probe. This is due to the fact that the PHA method uses different energy windows for the incident energy spectra considered. In both methods A_1 increases with the atomic number of each of the calibration materials except for zinc. This is due to copper having a higher density than zinc even though the difference in atomic number would suggest an increase in A_1. The value of A_1 is proportional not only to the atomic number cubed but also to the density of the material under consideration (equation 1.27).

Figure 2.11

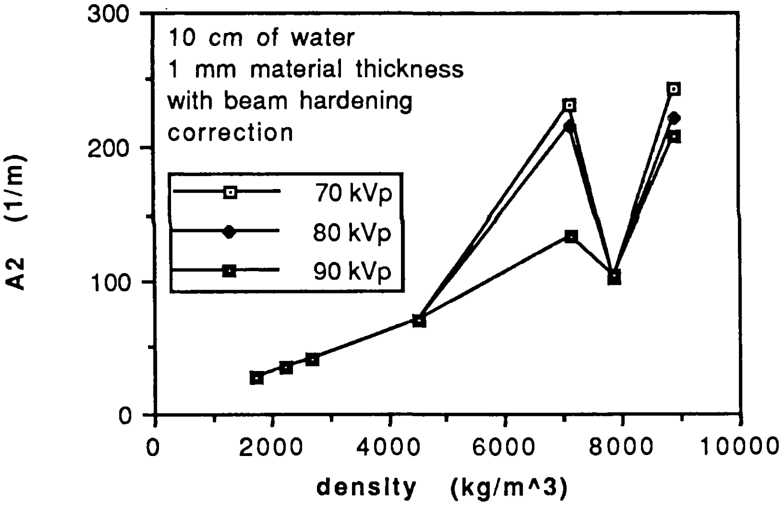

c) split detector method for A2

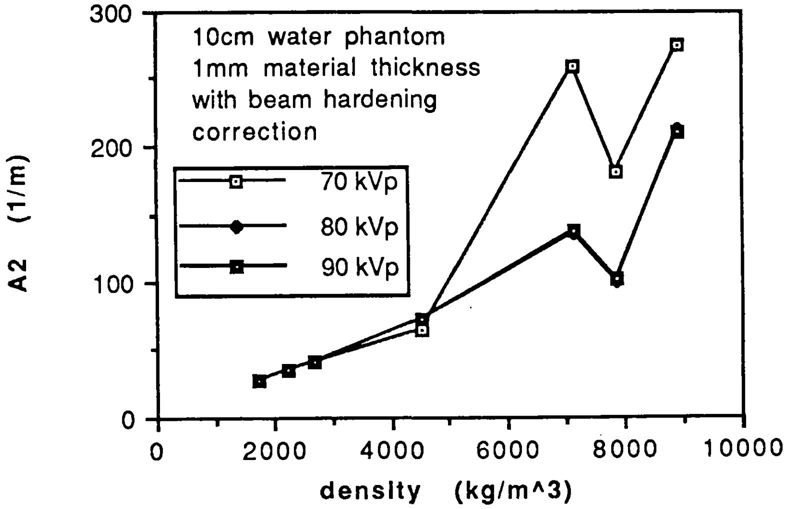

d) PHA method for A2

A_2 is proportional to the material density and shows little energy dependence over the range 70-90 kVp for low densities (figures 2.11c and 2.11d). However, for Zn, Fe and Cu, whose densities are larger, there is evidence of energy dependence of the order that A_2 increases as kVp decreases. This is due to the fact that the dual energy sensitivity increases with higher incident spectra (table 2.5) which manifests itself as an increase in A_1 and a decrease in A_2. Although A_2 increases with higher densities, a sharp drop is observed from Zn to Fe, which corresponds to an increase of density from 7140 to 7860 kg/m^3. The reason for this could be that at high atomic numbers the photoelectric absorption coefficient becomes significant and in the process the contribution from Compton scattered radiation and, hence, A_2 diminishes to the point where the dual energy analysis is no longer capable of distinguishing differences at high densities.

2.3.2 Dependence on Material Thickness

In figure 2.12 the dual energy coefficients for the corresponding calibration materials were calculated for a 10 cm water phantom and an 80 kVp incident spectrum for both types of probes. In Figures 2.12a and 2.12c A_1 is plotted against the thicknesses of carbon, magnesium and aluminium, both with and without the beam hardening correction. The variation in A_1 is almost constant for both probes at the thickness range considered.

The effect of material thickness becomes quite significant at higher atomic numbers, particularly for the split detector method, as can be seen in figures 2.12b and 2.12d. When the split detector probe is considered, there is a 20% decrease in A_1 for Ti and as much as 50% decrease for Cu over the range of 0.1 mm to 1 mm. This is due to the beam hardening effect. Using the iterative procedure for beam hardening correction this variation in A_1 is reduced to 8% for Ti and ~17% for Cu. Similarly, the PHA probe shows a decrease in A_1 at high atomic numbers. However, this variation is small in comparison with the split detector probe. As an example, the variation in A_1 for Fe and

Figure 2.12 Dependence of A_1 on Material Thickness*

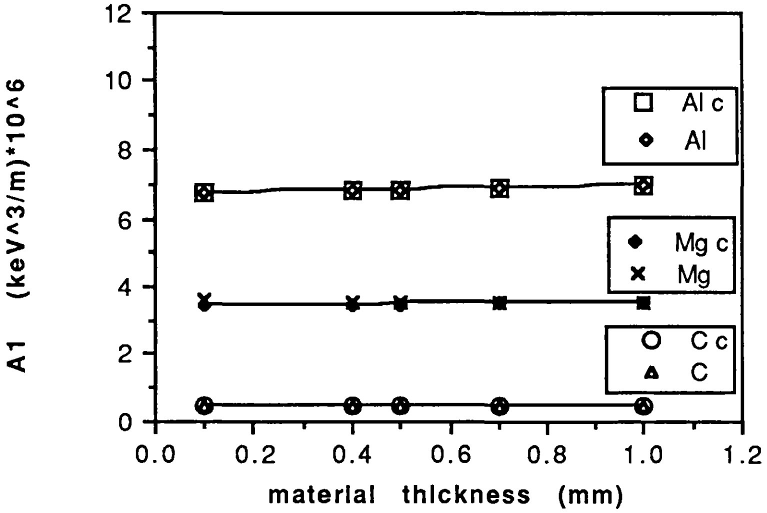
a) Split detector method for A1

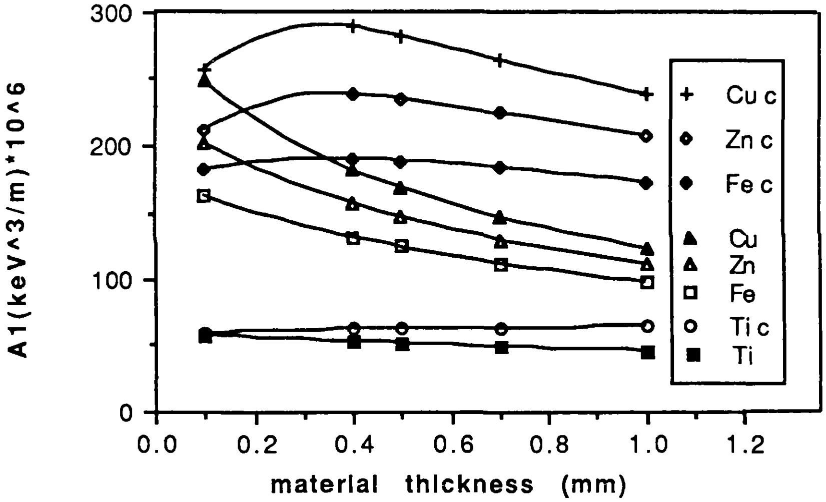
b) Split detector method for A1

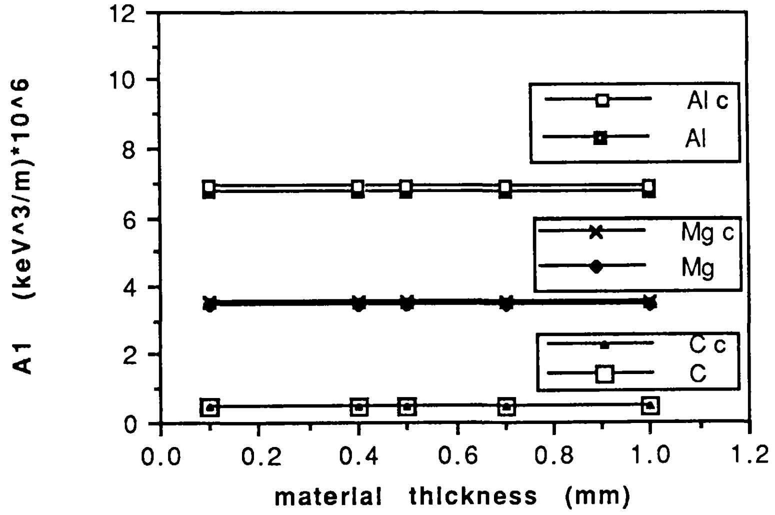
c) PHA method for A1

* c - beam hardening correction

Figure 2.12*

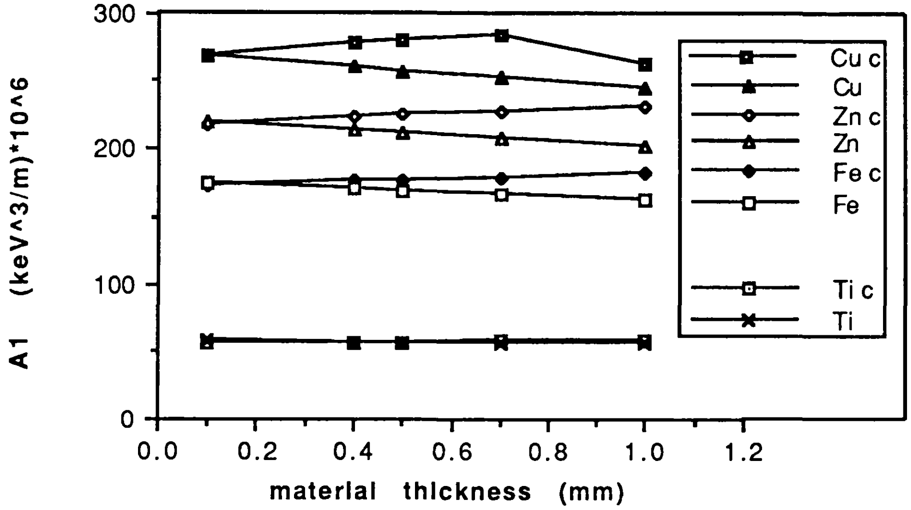
d) PHA method for A1

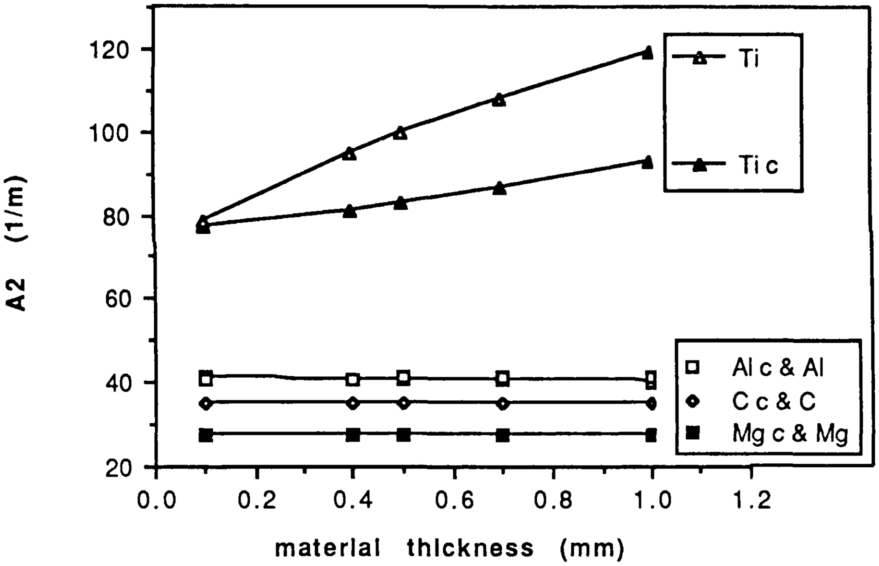
e) Split detector method for A2

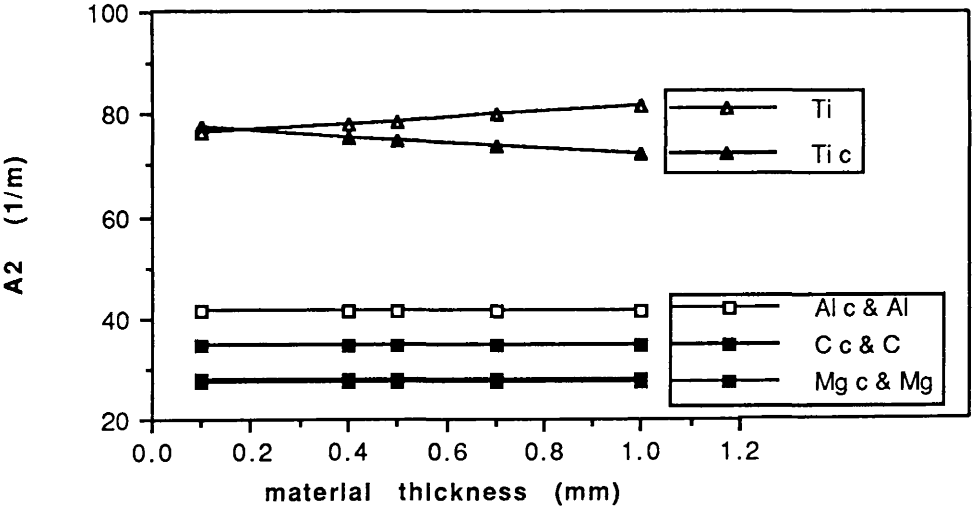
f) PHA method for A2

Zn is reduced from 6% and 8% to about 3% and 4% respectively when the beam hardening correction is employed. The split detector method appears to be more sensitive to the high atomic number material thickness than the PHA probe. This is due to the use of a single effective energy to represent a broad absorbed spectrum unlike the PHA analysis where relatively narrow bands of energy are used.

It has been shown in section 2.3.1 that beyond $\rho = 4500$ kg/m^3 the value of A_2 loses its proportionality with the material density. So in figure 2.12e and figure 2.12f, the effect of material thickness upon this study was restricted to four calibration materials only. For low atomic numbers both methods are independent of calibration material thickness (with and without beam hardening correction). In contrast to A_1, the value of A_2 for Ti increases with calibration material thickness. When the iterative procedure is employed the variation in A_2 is dramatically reduced, especially for the split detector method (figure 2.12e).

2.3.3 Effect of Patient Depth

The dependence of A_1 and A_2 on the phantom thickness is shown in figure 2.13. The values of A_1 and A_2 were computed for an 80 kVp spectrum. The calculation of the effective energies E_{eff1} and E_{eff2} (equation 2.3) of the spectrum absorbed by the CsI and NaI detectors respectively depends on the water phantom filtration as shown in table 2.10. The effective energies of the absorbed spectra increase with water thickness because of the beam hardening effect.

Figures 2.13a and 2.13b show how omitting the beam hardening correction causes the value of A_1 to decrease with increasing water phantom thickness for the same calibration material. This occurs because of the increase in the effective energies of the whole absorbed spectra (table 2.10) or in the selected windows. This leads to a smaller separation between E_1 and E_2 and hence to less sensitivity in A_1. Table 2.11

Table 2.10 Effective Energy Variations

water thickness (cm)	E_{eff1} (keV)	E_{eff2} (keV)	DES (keV)
10	44.91	58.21	13.30
15	47.35	59.24	11.89
20	49.49	60.30	10.81

Figure 2.13 Effect of Phantom Depth*

a) Split detector method for A1

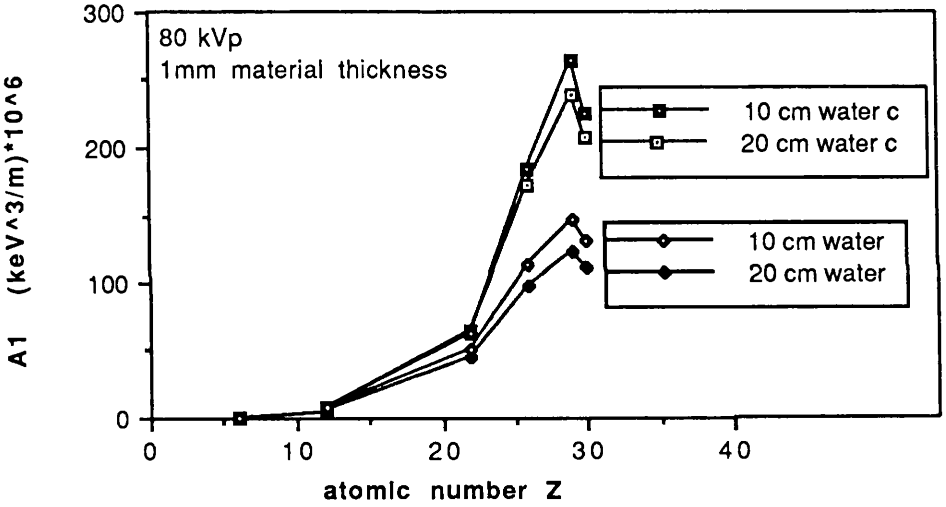

b) PHA method for A1

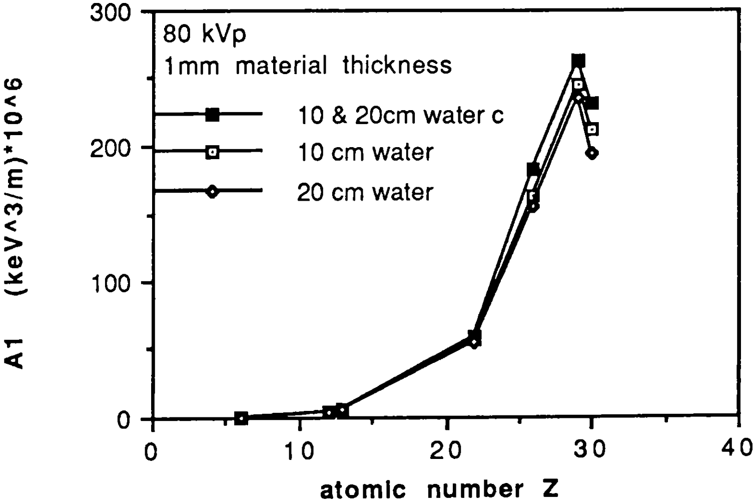

* c - beam hardening correction

demonstrates how this variation increases with higher atomic numbers, reaching 14% for Cu for the CsI/Cu/NaI probe and 3% for the PHA probe. The effect of beam hardening is more apparent for the split detector probe because of the assumption that two broad spectra can be represented by two effective energies.

When the iterative procedure for beam hardening correction is employed, figures 2.13a and 2.13b show two facts. Firstly, the value of A_1 becomes independent of the water thickness for low atomic numbers and its variation is dramatically reduced for high atomic numbers. Secondly, the value of A_1 for high atomic numbers are underestimated when the correction is omitted.

Table 2.11 Variation of A_1 with Water Phantom

variation of A_1(%) from 10 to 20 cm of water

80 kVp		C	Mg	Al	Ti	Fe	Cu	Zn
no correction :	SDM*	0	1.7	2.2	5.8	11.2	14.2	12.9
	PHA	0	0	0	2.5	1.7	5.0	3.0
with correction :	SDM*	0	0	0	1.5	1.4	4.0	3.0
	PHA	0	0	0	0	0.1	0.3	0.2

* SDM - split detector method

In Figure 2.13c and figure 2.13d the values of A_2 are considered. It can be seen that the value for Ti ($\rho = 4500$ kg/m^3) increases as the water thickness increases from 10 to 20 cm unlike the behaviour of A_1. For low densities, the value of A_2 is independent of water thickness for both probes.When A_2 is corrected for beam hardening, there is almost a linear response of A_2 as a function of density (up to Ti) regardless of the water thickness.

Figure 2.13*

c) Split detector method for A2

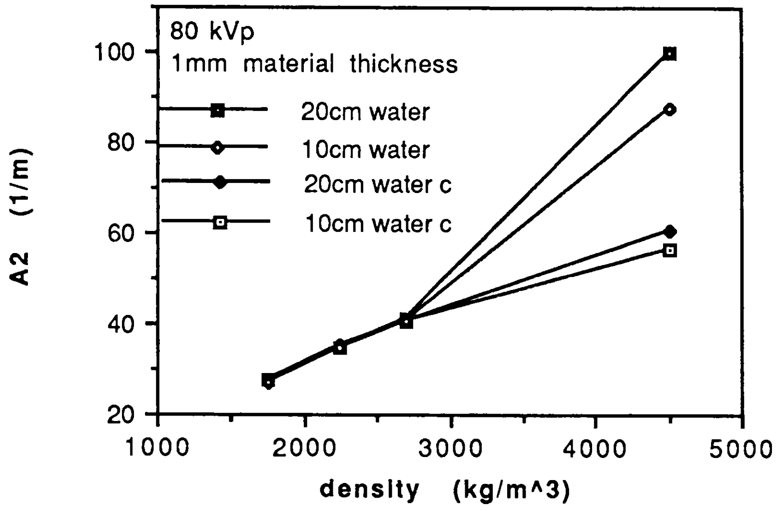

d) PHA method for A2

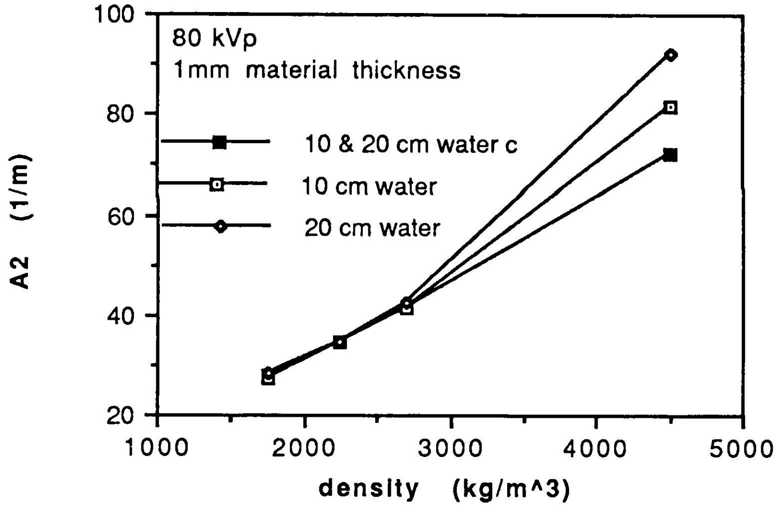

c* - beam hardening correction

2.4 Conclusion

The following conclusions can be drawn :

1. The iterative procedure for the beam hardening correction was very successful at correcting for the variation in phantom thickness. The PHA method showed no

significant variation in A_1 with water thickness and the split detector method showed less than 4% variation. The same is true for A_2 where the iterative procedure has restored the linearity between A_2 and density for a high atomic number material like Ti.

2. Although the beam hardening correction managed to considerably reduce the variation in A_1 with material thickness for high atomic numbers, there is still a relatively significant variation, especially for the split detector method. Depending on the accuracy required, unique values of A_1 exist for atomic numbers up to Z = 22 for the split detector method ($\sim$ 8% variation) and up to Z= 29 for PHA method ($\sim$ 3%) over a material thickness range of 0.1 to 1mm.

3. The dual energy analysis is not sensitive enough to pick up differences between materials of high densities. If Z exceeds 22, the proportionality between A_2 and material density is lost in both dual energy probes.

4. In general terms, the PHA method proved to be affected less by material and phantom thickness than the split detector method.

In the next chapter the construction of dual detector probes is undertaken. Although the PHA method showed better performance, the split detector probe is still considered because it is easy to manufacture, cheaper to construct, as it does not required sophisticated electronics, and faster to obtain dual energy measurements. Two types of PHA probes are considered; the scintillation probe and the semiconductor probe. All three detectors are evaluated experimentally and compared to the computer results.

In chapter 4, the contribution of scattered radiation to the dual energy system is simulated both theoretically using a Monte Carlo model and experimentally. As a clinical application of the dual energy probes, *in vitro* gallstone analysis is investigated in chapter 5.

CHAPTER 3 EXPERIMENTAL RESULTS- SPLIT DETECTOR PROBE AND PHA PROBES

3.1 The Split Detector System

3.1.1 Introduction

The principles behind the design of the split detector were discussed in section 1.4. The selection of the optimum system and its expected performance were presented in chapter 2. The practical dual energy system should comprise two scintillation detectors with associated lightguides and photomultiplier (PM) tubes, a simple two channel DC amplifier, an analog to digital converter (ADC) coupled with an analog multiplexer, an interface to connect the ADC to a computer and the computer. An Apple IIe personal computer was used as the data collection and data processing device.

Two 9924B PM tubes from Thorn EMI provide the main amplification to the dual energy system. They were chosen for their excellent gain stability which makes them ideal for direct current mode operation and also for their low dark current production. Two high voltage supplies (Canberra series 3105 NIM and 3102 series NIM) were used to ensure separate gain control. The rest of the equipment was built at the University College and Middlesex School of Medicine (UCMSM). A block diagram of the split detector system is given in figure 3.1.

3.1.2 Construction of The Split Detector System

i) The Detector, Lightguide and PM Tube Assembly

The crystalline scintillators, which were a 0.25 mm CsI (25.4 mm diameter) and a 25.4 mm NaI detector (25.4 mm diameter), were obtained from HILGER Analytical.

Figure 3.1 Split Detector System Block Diagram

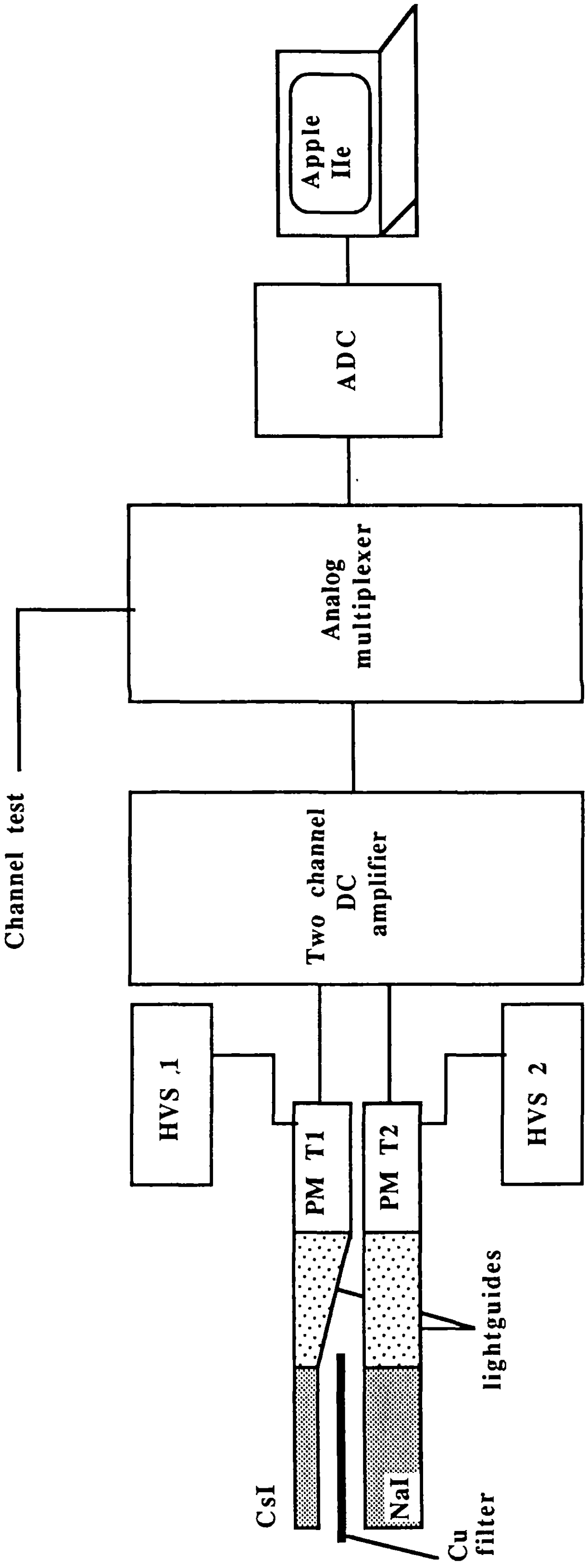

Lightguides, made out of perspex, were machined to the specified size to physically couple the scintillators to the PM tube (figure 3.2). Silicon oil was used as the coupling agent between the crystals and lightguides. Both assemblies were painted with aluminium oxide reflective coating, then coupled to the PM tubes by silicon oil. The whole assembly was then wrapped in black Scotch tape to shield the detector system from ambient room light.

Figure 3.2 Detector Arrangement

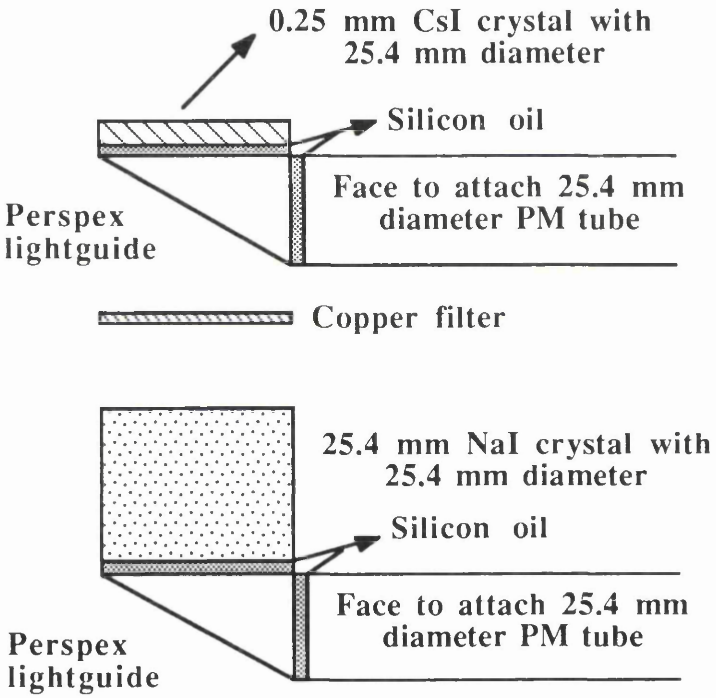

In order to operate the PM tubes in DC mode the anode is fixed at ground potential. Thus, negative high voltage supplies are used.

ii) The DC amplifier

The two channel DC amplifier changes the PM tube output current into a voltage of several volts (a maximum of about 8 Volts). The two PM tubes with their respective crystals were monitored by varying the x-ray intensity to ensure PM tube linearity. Ideally the two detectors should have the same sensitivity so that the dual energy analysis would not be limited by the bad response of one detector. The high voltage supplies were set such that both PM tubes have linear response and are matched as closely as possible. In figure 3.3, the DC amplifier output was plotted against the output of a 35 cm^3 ionisation chamber. These values were obtained by varying the current of the x-ray tube generator. For each value of kilovoltage considered, the high voltage supplies for the two PM tubes were selected not only to obtain maximum linearity of the DC amplifier output from the two detectors but also to match the two detector responses.

Figure 3.3 Response of PM Tubes

a) 70 kVp

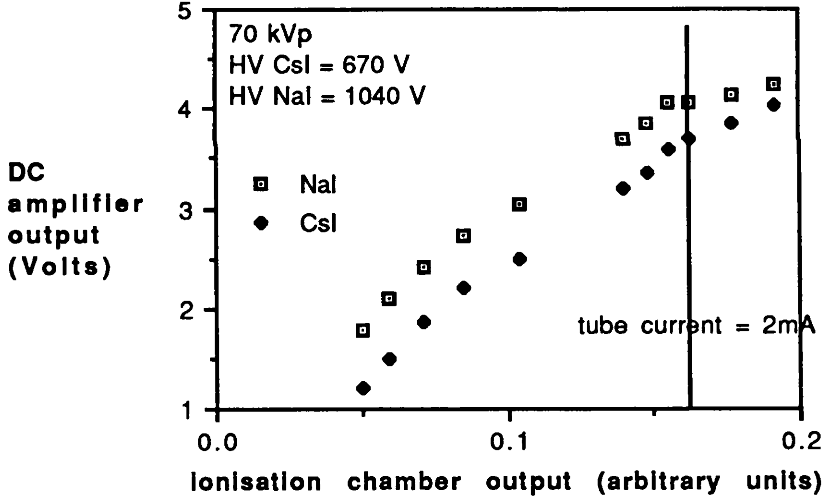

b) 80 kVp

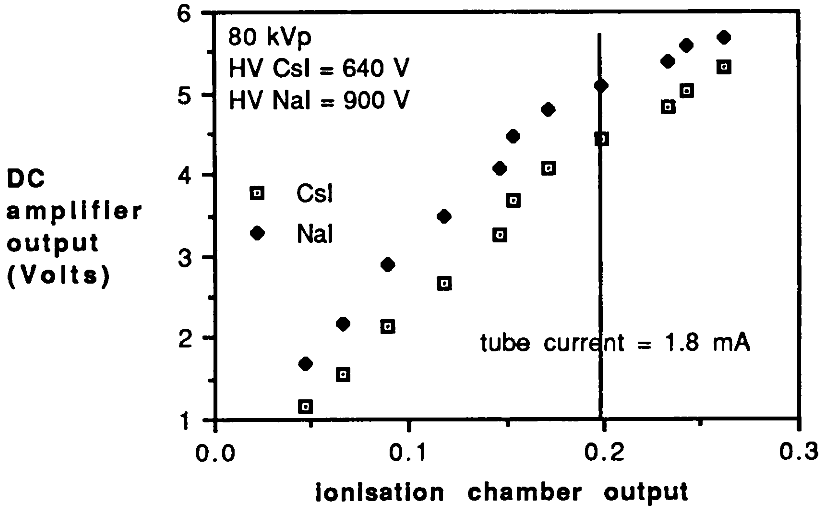

Figure 3.3

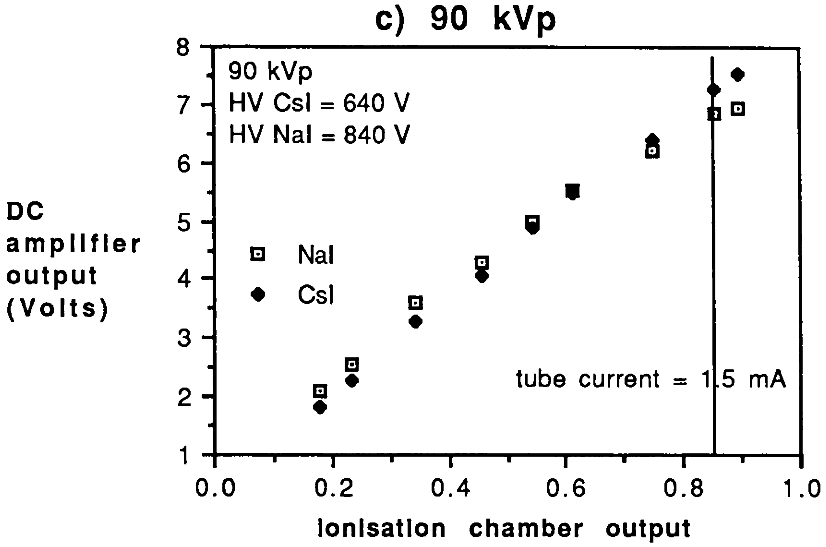

iii) Analog Multiplexer, A/D Converter and Computer Interface

The analog multiplexer ensures fast, multiple data collection and prepares data for digitisation. The analog multiplexer built at UCMSM features three channels in common current summation configuration, two of which are for both PM tube signals and an additional one that was used as a channel to monitor the x-ray tube output. The architecture of the Apple IIe personal computer provides several peripheral connectors, the required interfacing circuitry for the analog multiplexer and the A/D converter were already located inside it. The A/D converter was an ADC AD574A from Analog Devices. To use the multiplexer/ADC board, suitable software is essential. The sequence of measurements carried out with the multiplexer/ADC board was determined by an assembler subroutine written with the Apple Editor Assembler EDASM as follows :

i) switch the analog multiplexer to channel 1 (PM tube 1 for CsI), take measurement, start A/D conversion and then read result. Repeat the measurements 100 times, sum them and divide by 100. Display the result.

ii) switch the analog multiplexer to channel 2 (PM tube 2 for NaI) and repeat the measurements as in channel 1.

iii) switch the analog multiplexer to channel 3 (a test channel). Repeat the same procedure as channel 1 and channel 2.

The whole process (300 measurements) takes approximately 70 ms.

One hundred measurements were taken in order to improve the quality of the raw data. The linearity and channel separation of the multiplexer/ADC board was tested by replacing alternately the PM tube inputs of the board with an output voltage of a laboratory power supply. The measured values, displayed on the Apple IIe computer, were compared with the reading of a digital voltmeter. The results are shown in figure 3.4.

Figure 3.4 Multiplexer/ADC Board Test

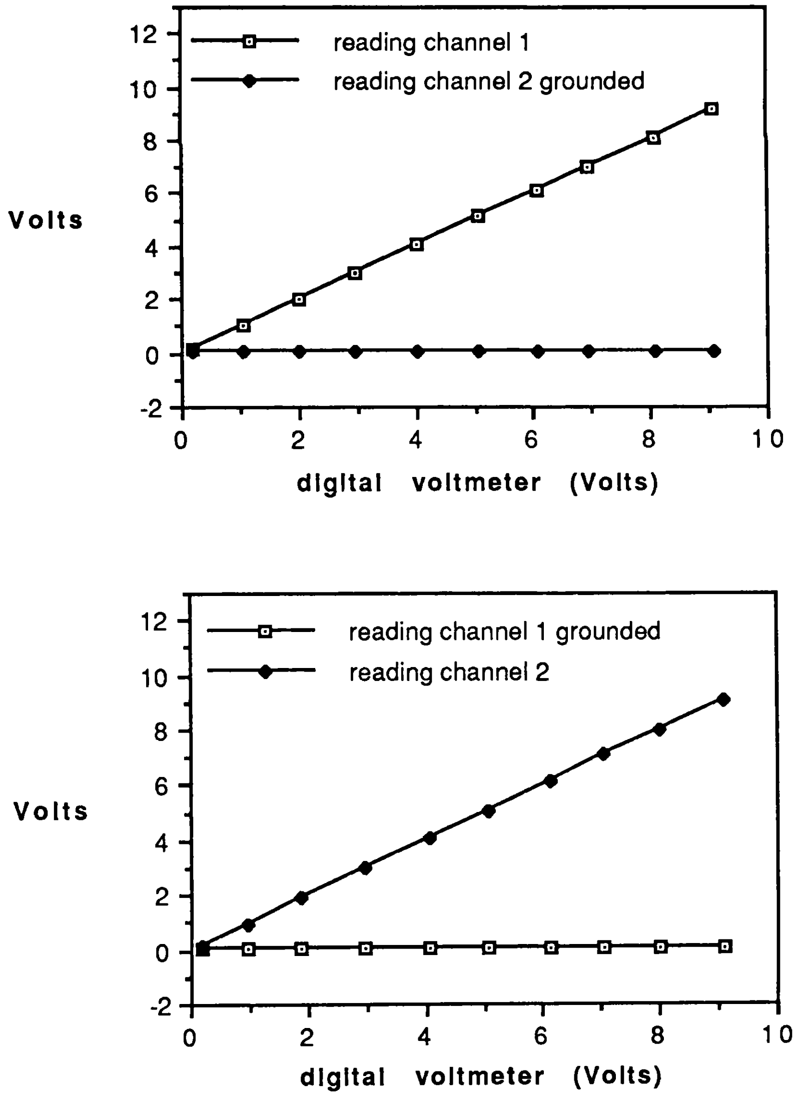

3.2 PHA Dual Energy Probe

3.2.1 Introduction

PHA systems measure the pulses produced by the absorption of individual photons in a detector. Two types of PHA detectors are considered in the experimental evaluation of the dual energy analysis; a 25.4 mm NaI scintillation detector and a high purity germanium (HPGe) solid state detector with an active area of 25 mm^2 and 5 mm thickness.

The scintillation detectors are characterized by a very good quantum efficiency but with low intrinsic resolution (>> 10% for diagnostic x-rays). The semiconductor detectors have moderate quantum efficiency (though still excellent for diagnostic x-ray energies) and high intrinsic resolution. However, the semiconductor's superior resolution is opposed by

i) equipment costs. Very small detector signal currents require a spectroscopy amplifier with very low noise properties.

ii) higher maintenance costs. It is essential the detector is cooled by liquid nitrogen.

iii) a much bulkier detector housing. The liquid nitrogen is contained in a 25 litre dewar.

3.2.2 PHA System Performance

The basic scintillation counting system consisted of a 25.4 mm NaI scintillation detector, used in pulse counting mode, together with a PM tube, a J&P amplifier NM112 and a J&P high voltage supply NM120. The semiconductor detector employed was a high purity, planar germanium detector (HPGe) in a vertical dipstick configuration (type 7500 from Canberra). The HPGe has an active area of 25 mm^2 and 5 mm

Figure 3.5 PHA Dual Energy System Block Diagram

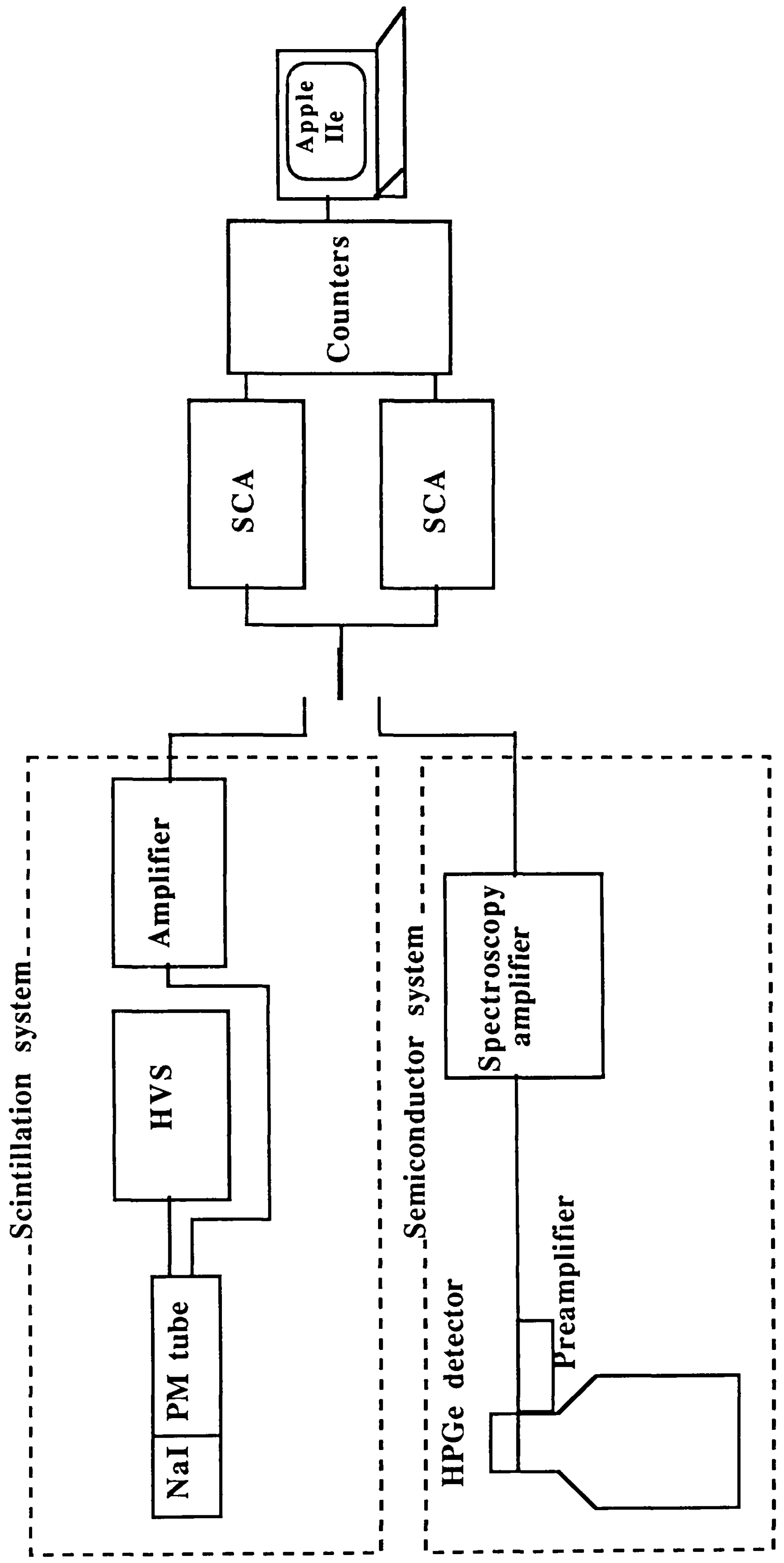

thickness. Its resolution defined at the full width half maximum is 196 eV at 5.9 keV and 484 eV at 122 keV. The efficiency is above 80% for the 10-90 keV energy range. The semiconductor detection system also included a high voltage supply (model 3012 from Canberra), a Canberra model 2005 preamplifier and a Canberra 2020 spectroscopy amplifier. Each system is fed into two single channel analysers (SCA) (Canberra 2031 series). The logic output pulses from the SCAs were recorded by two independent counters of a 6840 LSI timer/counter interfaced to the Apple IIe computer. The block diagram of both systems is shown in figure 3.5

i) 6840 LSI Counters

The counters are interfaced to the Apple IIe and run using suitable software, similar to the split detector method . The counters were set such that they can count up to 25 s for any single measurement. An Americium-241 calibration source was used to test the linearity of the 6840 LSI counters by comparing the signal output from the NaI detector obtained by these counters to that obtained from an additional dual counter timer (2017A from Canberra). The results are shown in figure 3.6.

Figure 3.6 Counters Test

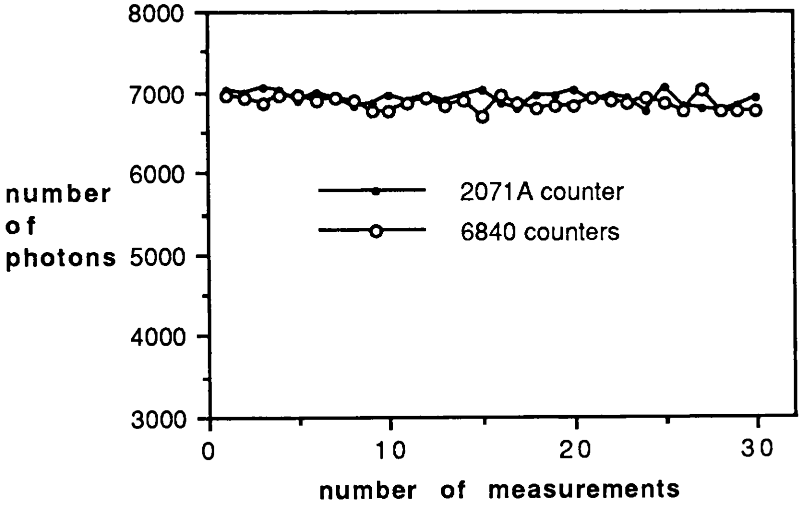

ii) J&P Amplifier NM112

The J&P amplifier used for the scintillation detector system was monitored by varying the intensity of the x-ray tube to ensure linearity of the amplification. The signal from the J&P amplifier was fed to a SCA (with its window set to detect the whole spectrum) and the number of photons were counted, for each intensity, using an additional dual counter (figure 3.7).

Figure 3.7 Scintillation System Performance

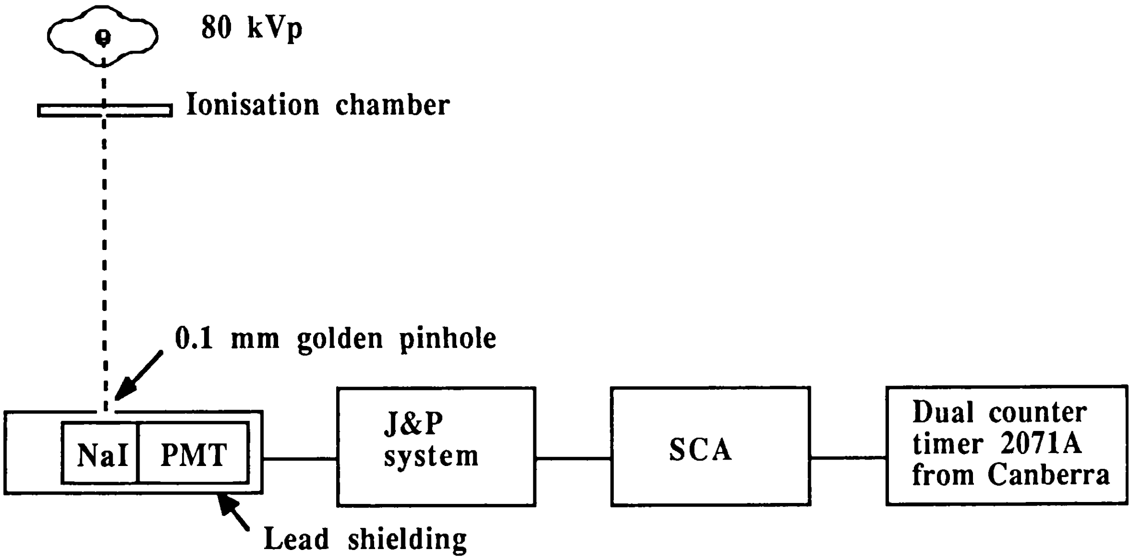

Figure 3.8 J&P Response

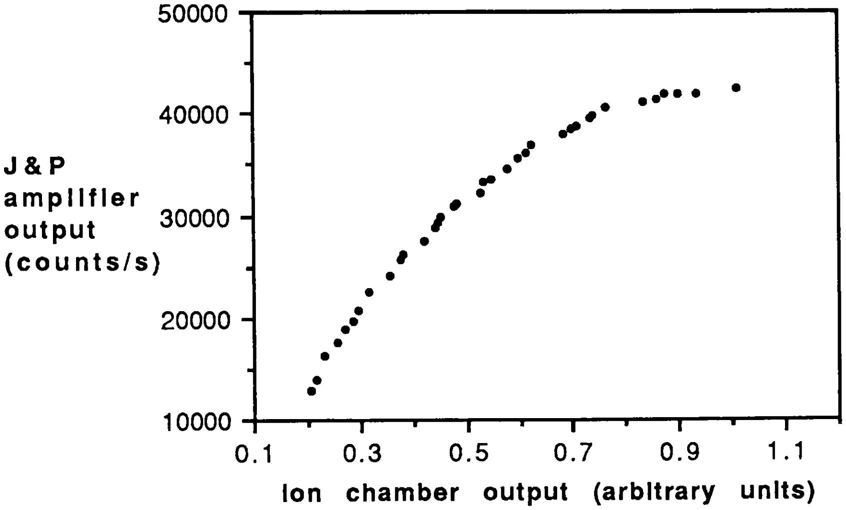

At the same time the x-ray output was monitored by the 35 cm^3 ionisation chamber. Figure 3.8 shows that the J&P amplifier can cope reasonably well up to 40,000 counts per second (100 ms constant time). At higher count rates it loses its linearity with the x-ray output.

3.3 The X-ray Tube, Phantoms and Mechanical Accessories

3.3.1 Introduction

Conventional diagnostic x-ray apparatus (a Siemens Ergophos 4 with an RG-125/100 x-ray tube) was used to test the dual energy probes. Fluoroscopic mode was selected for the x-ray unit. It is proposed that in a clinical application the position of the probe would be visualised on the TV monitor of the image intensifier system. Thus, digitally controlled scanning of the area of interest for localised tissue characterization could be undertaken. The development of the probe has reached the stage where such a proposal is possible. However, the complete investigation takes several seconds which means that the stability and time variation of the x-ray tube output must be known.

A brief description of the tests carried out on the x-ray apparatus and of the design of phantoms, beam collimators and mechanical accessories of the test system is given in the following sections.

3.3.2 Time Variation of the X-ray Tube Output

The time variation of the x-ray tube output was considered for two cases

i) long time variations during one continuous run (sampling period of about 2 s)

ii) output variations between subsequent switching on and off of the x-ray tube (sampling period of about 15 s).

All these tests were carried out using the split detector system.

The long time variations of detector signals were investigated in order to decide whether it is justifiable to use the output of the ionisation chamber as a correction for the scintillator (or semiconductor) signals. Examination of one continuous exposure revealed a large variation in the intensity shortly after switching on the x-ray tube. A typical example of an output versus time signal is given in figure 3.9. It will be noticed that the PM tube signal exhibits an overshot of 53% shortly after switching on in comparison to a flat signal area which starts about 8 s after switching on. The ionisation chamber signal rises to less than 20% above its final level. Hence, the ionisation chamber cannot be used to provide corrections for the variation in output of the PM tube in the period immediately following switching on the x-ray tube. Consequentlly, all measurements were started after the tube had been running for 10 seconds or more.

Figure 3.9 PM Tube and Ionisation Chamber Outputs

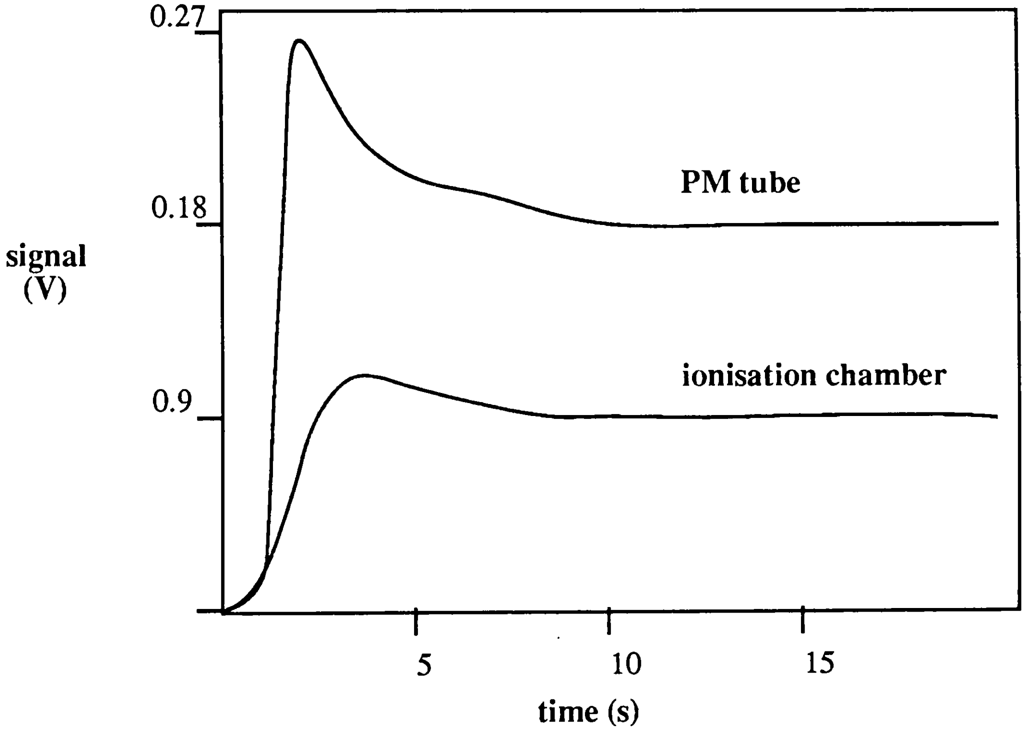

One hundred measurements were taken of the signals from the PM tube and ionisation chamber separated by 2 seconds intervals. Table 3.1 shows the variation of individual detector signals and the correlation of PM tube and ionisation chamber output. The results suggest that although some stability is observed, there is virtually no correlation between the variation of the PM tube signals and the ionisation chamber output. The missing correlation completely prohibits the use of the ionisation chamber as a monitor for the x-ray tube during one continuous exposure.

Fourty separate exposures accounting for an overall time of 10 min were undertaken for the second case. Results in table 3.1 show a relatively strong correlation and because of this a correction of measured intensities with the ionisation chamber for subsequent single exposures could prove to be useful. However, the x-ray tube output variations during one single exposure are smaller than those during switching on and off the x-ray tube.

Table 3.1 Variation of PM Tubes with Ionisation Chamber

case	variation of PM tube 1	variation of PM tube 2	correlation PM tube 1 vs IC*	correlation PM tube 2 vs IC*
1**	1.12%	1.37%	0.089	0.026
2†	1.94%	1.90%	0.937	0.901

* IC - ionisation chamber

** single continuous exposure

† switching on and off the x-ray tube

As the ionisation chamber cannot be employed to monitor the x-ray tube during a single continuous exposure, an alternative was investigated. Using the PHA probe, an 80 kVp incident spectrum was monitored by taking 250 measurements at two selected windows starting 10 s after switching on the x-ray tube. Each measurement was taken for 1 second.

Figure 3.10 Monitoring of the X-ray Tube Output with Time

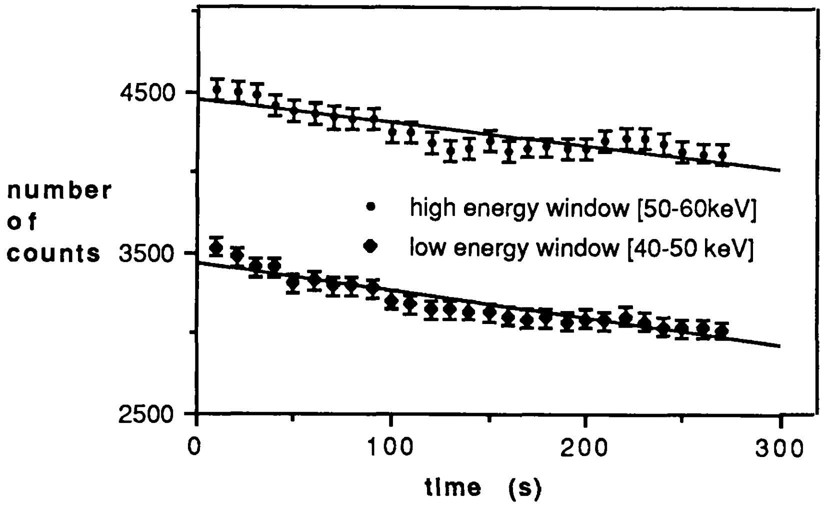

Figure 3.10 shows that the x-ray tube output has a linear decrease with time within the experimental error. Thus, this fact can be used to correct for the x-ray tube changes during a single exposure (cf. 3.4.1).

3.3.3 Phantoms and Mechanical Accessories

The basic phantom used was a water filled perspex container. Average patient thickness was represented by 15 cm of water but some experiments were carried out at water depths of 10 cm and 20 cm to investigate the effect of variation of soft tissue thickness. The materials examined were the same as the calibration materials used for the computer simulation in chapter 2 (cf. table 2.7). They were used in the form of thin foils of 0.1 mm, 0.5 mm and 1.0 mm thickness. The purity of all foils exceeded 98% (Goodfellow catalogue 1988). The delicate foils were placed between two perspex discs of 12 mm overall thickness to avoid any deformation. The soft tissue thickness was thus increased by an equivalent value of 12 mm of perspex. The thickness of the perspex container causes the same effect. Section 2.1.4 included these additional materials for the computer model.

Due to variations in x-ray output when the generator is switched on and off an automatic system was developed for the changing of the material under investigation. A stepping motor together with a suitable driver and interfacing circuitry was included in the measurement system. The stepping motor was employed to turn the disc with calibration materials so that each one was positioned below the x-ray field. This guaranteed easy and rapid changing of the calibration materials even during an uninterrupted exposure. Furthermore gaps between neighbouring materials in the disc enable frequent recalibration of the x-ray intensity.

Beam collimation was provided underneath the source and directly in front of the detectors. All collimators consisted of 2 mm lead sheets with pinholes of different diameters depending on the mode of energy separation. Photomultipliers and lightguides were wrapped in 1 mm lead sheet to shield the detector system from scattered radiation. The complete arrangement of the experimental set up is illustrated in figure 3.11.

Figure 3.11 Set-Up of Dual Energy Probes

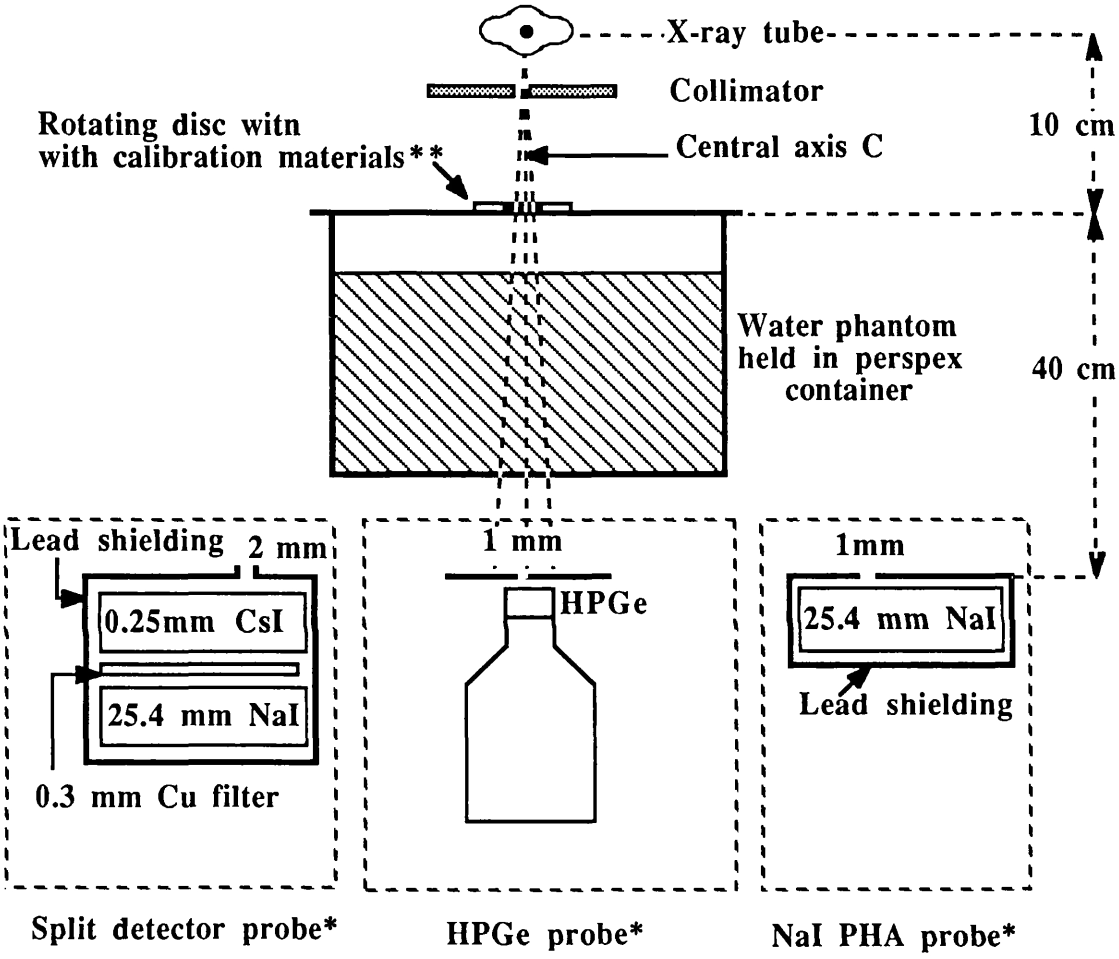

* Each dual energy detector probe was placed in turn underneath the water phantom
** disc was driven by a stepper motor

3.4 Measurements and Results

3.4.1 Introduction

All measurements that were made observed the difference in signal variation of the high energy and the low energy detector of a dual energy detector system when a calibration material was placed in the collimated beam. Thus, the variation of attenuation properties with energy of a certain material was measured at two energies. The objective of this investigation was to assess the sensitivity of the dual energy detection system and thus its capability of distinguishing different materials.

The disc containing the material tabulated in table 2.8 were used to carry out calibration measurements. The sequence of measurements followed those governing the theoretical consideration of the dual energy analysis using equations 1.42 and 1.43 :

$$A_1 = \left\{ F_{KN}(E_1) \ln \left[D_m(E_2)/D_w(E_2)\right] - F_{KN}(E_2) \ln \left[D_m(E_1)/D_w(E_1)\right] \right\} \times E_1^3 E_2^3 / R \qquad 3.1$$

$$A_2 = E_1^3 \ln \left[D_m(E_1)/D_w(E_1)\right] - E_2^3 \ln \left[D_m(E_2)/D_w(E_2)\right] / R \qquad 3.2$$

where $R = \left\{F_{KN}(E_2) E_2^3 - F_{KN}(E_1) E_1^3 \right\} t$

The required signals $D_m(E)$ and $D_w(E)$ can be obtained from two measurements only since low and high energy photons are observed simultaneously by the dual energy detection system. However, two measurements, one with and one without calibration material, have to be made. The signals arising when no calibration material was present were conducted by taking two measurements of soft tissue background, one before and one after measuring the calibration material signal $D_w(E)$. Subsequent interpolation between the two values acquired resulted in the desired background intensity. This process was adopted as the most direct method of correcting for x-ray output changes during a single exposure. The x-ray tube output decreases linearly with time, as shown in figure 3.10, thus the above process is equivalent to recalibration of the x-ray tube intensity.

In all the following experiments, measurements have been repeated at least five times and the errors calculated using the standard deviation of these measurements. In this way the switching inaccuracy of the x-ray tube operating voltage should be included in the acquired standard deviations.

3.4.2 Split Detector Probe

The calibration materials were moved into the collimated beam using the stepping motor. The signal from the CsI and NaI detectors was collected such that the required intensities in equation 3.1 and equation 3.2 are obtained from two measurements taken in one continuous exposure; the first without calibration material in order to measure the average background signals $D_w(E_1)$ (signal from CsI) and $D_w(E_2)$ (signal from NaI), and the second measurement with calibration material to measure $D_m(E_1)$ and $D_m(E_2)$, the transmitted photons reaching the CsI and NaI detectors respectively. E_1 and E_2 in equation 3.1 and 3.2 represent the effective energies of the absorbed spectrum by the CsI and NaI detector respectively. The effective energies were determined theoretically by using the narrow beam geometry computer model to simulate the experimental set up and by using the definition of the effective energy which can be expressed as :

$$\mu_{eff}(E_{eff}) = \left\{ \Sigma\, \mu_w(E)\, N(E) \right\} / \Sigma\, N(E) \qquad 3.3$$

where $\mu_w(E)$ is the linear attenuation coefficient of water and Σ N(E) is the absorbed spectrum by either the CsI scintillator or the NaI scintillator. Table 3.2 shows the calculated effective energies for different incident spectra on the 10 cm water phantom.

Table 3.3 Effective Energies

Incident spectrum	E_{eff1} (keV)	E_{eff2} (keV)
70 kVp	42.64	53.27
80 kVp	44.91	58.21
90 kVp	46.68	62.29

3.4.3 PHA Dual Energy Probes

The pulse height analysis approach was used to produce two energy dependent signals simultaneously arising from the same source spectrum and by using a single detector, either the 25.4 mm NaI or the 5 mm HPGe solid state detector. This enables two separate energy regions of the spectrum to be analysed independently and should allow better energy separation than the split detector region.

The disadvantage of this method however is that there is considerable dead time and pulse pile up due to the high photon count rate that is available during a diagnostic examination. To overcome this problem the active area of the PHA probe must be finely collimated, thus leading to longer counting times if high statistical precision is to be maintained.

A typical experimental set-up uses a 1 mm pinhole (figure 3.11). In equations 3.1 and 3.2, $D_w(E_1)$ and $D_w(E_2)$ may either be intensities with $D_m(E_1)$, $D_m(E_2)$ transmitted intensities or $D_w(E_1)$ and $D_w(E_2)$ may be photon number with $D_m(E_1)$, $D_m(E_2)$ total counts. The latter is used with this method. The parameters A_1 and A_2 are obtained by making the following sequence of measurements :

i) First measurement taken without calibration material for a period of 10 seconds. This corresponds to background measurement.

ii) Second measurement taken for 20 s, this time with the calibration material present.

iii) Third and final measurement of the background again for 10 s.

In all the total measurement time is 40 s; 20 s for background measurement (linear interpolation between the first and last measurement results in the desired background counts) and 20 s for calibration material measurement.

$D_m(E_1)$ and $D_m(E_2)$ ($D_w(E_1)$ and $D_w(E_2)$) represent the number of photons collected in the lower energy window and higher energy window, with (without) calibration material respectively. E_1 and E_2 are the effective energies of the two selected windows (table 3.4).

3.4.4 Correction of Beam Hardening Using the Iterative Procedure

The experimentally measured values of A_1 and A_2 correspond to the first approximation values of the dual energy numbers A_1 and A_2. These values are then used to determine the first calculated approximation of the effective attenuation coefficient $\mu_{cal}(E)$ according to

$$\mu_{cal}(E) = 1 / x_m \ \ln \left\{ \int I_o(E)\, dE \,/ \int I_o(E) \exp\left(- \mu_{eff}(E)\, x_m \right) dE \right\} \qquad 3.4$$

where $\mu_{eff}(E) = A_1E^{-3} + A_2F_{KN}(E)$ and $\int I_o(E)\, dE$ corresponds to the number of photons absorbed by each detector (split detector probe) or at each energy window in the case of the PHA probe and x_m is the material thickness.

The integral, $\int I_o(E)\, dE$, was determined theoretically using the narrow beam geometry computer model. The spectrum of the incident radiation was taken from tabulated data (70, 80 and 90 kVp for an x-ray tube with a 17° tungsten target and an inherent filtration of 2 mm Al) from Birch *et al* (1979) and was assumed to match the experimental incident spectrum.

The procedure as described in section 1.6.5 was adopted until the difference between the measured and calculated effective attenuation coefficients is less than 1%, an indication that the corrected values of A_1 and A_2 for beam hardening had been reached.

3.4.5 Results

As in the narrow beam geometry computer model, the dual energy numbers A_1 and A_2 are determined for the three dual energy probes, namely the split detector probe, the PHA scintillation probe and the PHA semiconductor probe, for the following :

i) Three different incident spectra, 70, 80 and 90 kVp
ii) a range of calibration material thickness, 0.1 , 0.5 and 1 mm
iii) a range of water thickness, 10, 15 and 20 cm.

i) Dependence on Incident Spectra

In figure 3.12 the values of the dual energy number A_1 are measured for a 10 cm water phantom and for 1 mm material thickness and plotted against the calibration material number Z for various peak kilovoltages. The three dual energy probes are used. Both theoretical and experimental values of A_1, corrected for beam hardening, are presented. In all cases A_1 increases with increasing atomic number Z except for zinc due to its low density.

Figure 3.12a shows that the highest sensitivity for the experimental value of A_1 is obtained at 70 kVp. This result might seem confusing. As the dual energy sensitivity increases with increasing kVp value (cf. table 2.4), one would believe that the highest sensitivity would be obtained at 90 kVp. However, the rise of the effective energy of the spectrum absorbed by the CsI detector must be considered. This fact explains the behaviour of figure 3.12a.

The experimental values of A_1 are less than that predicted by the theory (figure 3.12a). This is due to the fact that the theoretical values of A_1 were calculated using the narrow beam geometry computer model which does not take into account the loss of energy in lightguides and PM tubes and to some extent the contribution of scattered radiation within the split detector probe.

Figure 3.12b shows rather a surprising result where at 80 kVp incident spectrum, the experimental value of A_1 is the highest leading to a better separation between different calibration materials. This is probably due to the choice of energy window sets selected during the dual energy analysis. In case of the PHA semiconductor probe, the experimental values of A_1 at 80 kVp incident spectrum are very close to that at 90 kVp. These values are not shown in figure 3.12c for sake of clarity.

If figure 3.12b and 3.12c are compared, the PHA semiconductor probe experimental results are more in agreement with the theory than are those obtained using the PHA scintillator detector. This difference is due mainly to the better energy resolution of the solid state detector which enables a more accurate energy separation of the two selected windows.

The experimental errors associated with the values of A_2 (using any of the three probes) were so large that any distinction between materials of low densities could not be made. This is due to the fact that the variation of the Compton component of the attenuation coefficient from which the value of A_2 is derived is small in comparison to that caused by the experimental error of the method. Furthermore, similar to the computer model a sharp drop of A_2 is observed in going from the titanium to zinc material. Thus, for the rest of this study only the dual energy coefficient A_1 will be considered.

Figure 3.12 Dependence of A_1 on Incident Spectra*

a) split detector probe

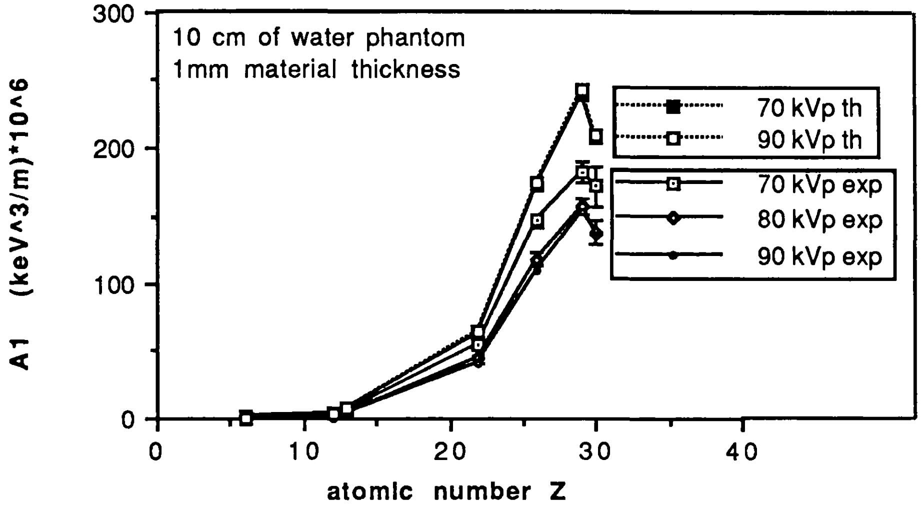

b) PHA scintillator probe

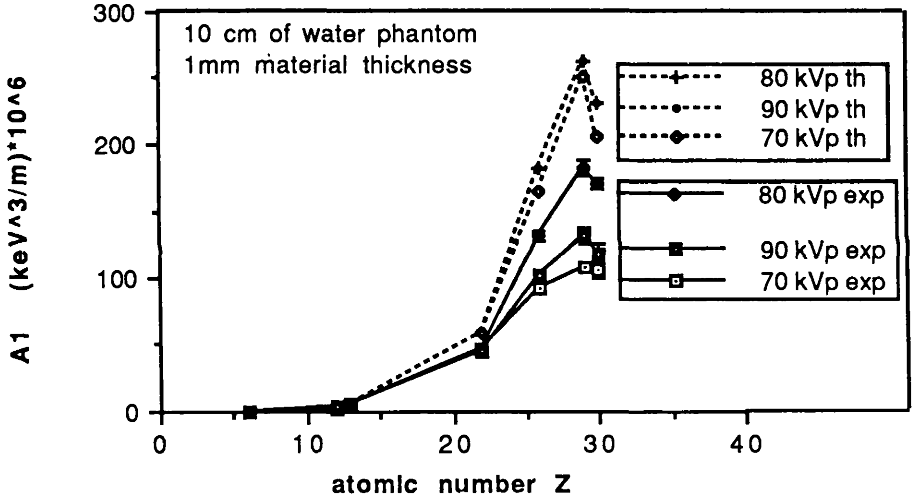

c) PHA semiconductor probe

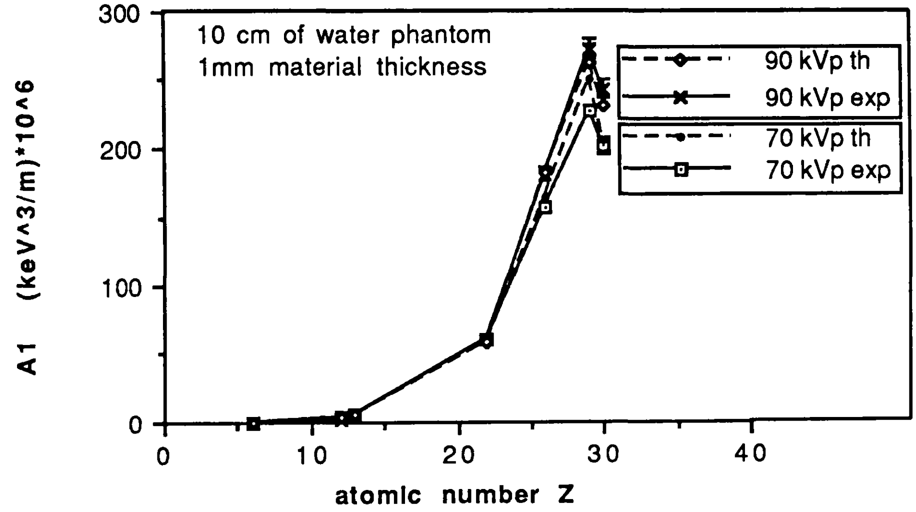

* th - theoretical ; exp - experimental

ii) Material Thickness Effect

In figure 3.13, the dual energy coefficient A_1 for an 80 kVp incident spectrum and 10 cm water phantom is plotted as a function of the calibration material thickness. All values of A_1 are corrected for beam hardening.

Identification of particular calibration materials with atomic numbers less than 13 could not be achieved using the thin foils of 0.1 mm and 0.5 mm (figures 3.13a, 3.13c and 3.13e). This is true for all the dual energy probes considered. However a distinct decrease in experimental errors is seen with increasing calibration material thickness, due to the increasing importance of the photoelectric interaction, to the point where, for the PHA semiconductor probe, the calibration materials C, Mg and Al are separated at 1 mm thickness. Clearly this imposes a limit in the detection of low atomic number tissues of about 1 mm in thickness. In practice many pathological details exceed 1 mm and we believe that if the material thickness is increased further, any of these dual energy probes would be capable of differentiating materials of low atomic number. This fact is investigated in chapter 5 where gallstones ranging from 4.5 to 7 mm thickness are considered.

The effect of beam hardening is still present for the PHA methods because relatively wide energy windows are used to achieve reasonable count rates. Figure 3.13d shows that the variation in A_1 when corrected for beam hardening is about 11% for Cu and about 4% for Fe across the thickness range considered. For lower atomic numbers however, this variation is small in comparison to the experimental error. In figure 3.13f, A_1 is almost independent of the material thickness (0.1-1.0 mm range) when the beam hardening correction is applied. This is due to the superior energy discrimination of the HPGe detector.

One of the major assumptions during the iterative procedure for beam hardening correction is the fact that the experimental incident spectrum matches the tabulated x-ray spectrum given by Birch *et al* (1979). This assumption is justified by figures 3.13b, 3.13d and 3.13f where the iterative procedure was relatively successful in carrying out the correction.

Figure 3.13 Dependence of A_1 on Material Thickness

a) split detector probe

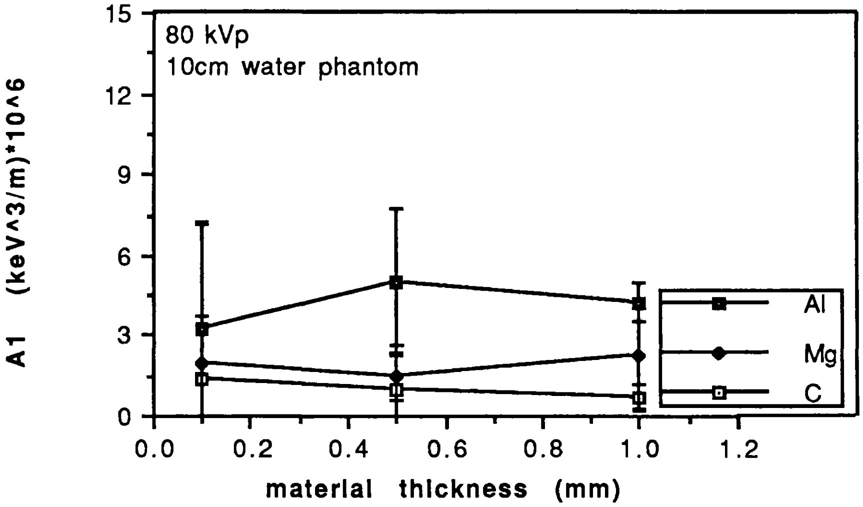

b) Split detector probe

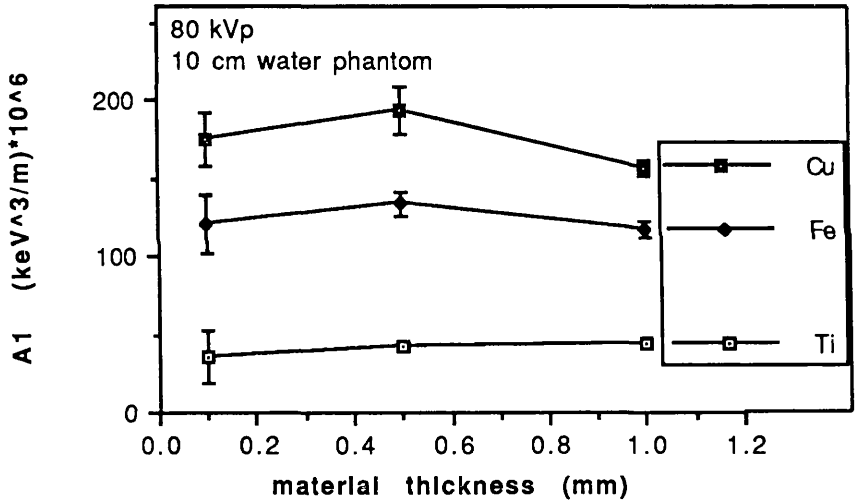

c) PHA scintillator probe

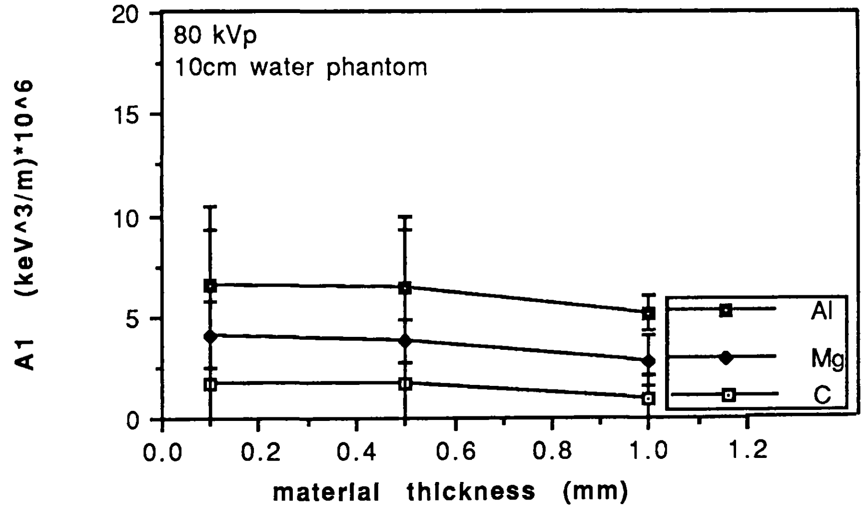

Figure 3.13

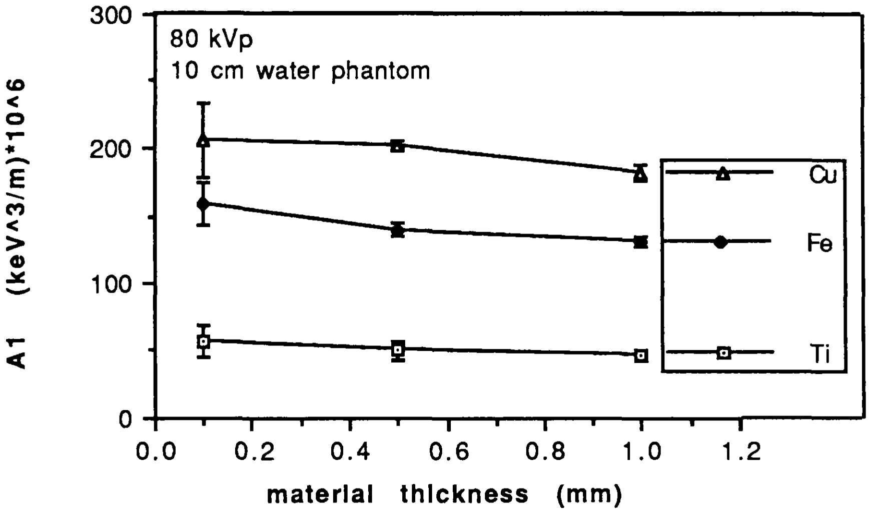
d) PHA scintillation probe

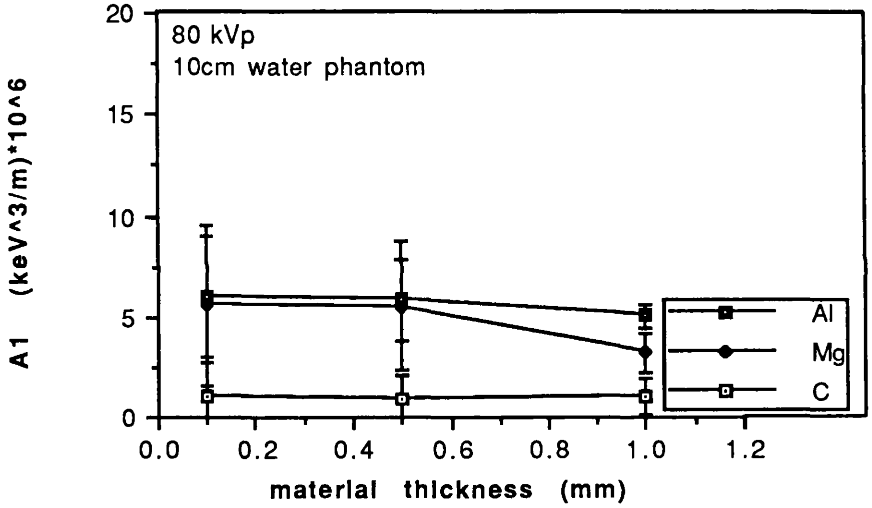
e) PHA semiconductor probe

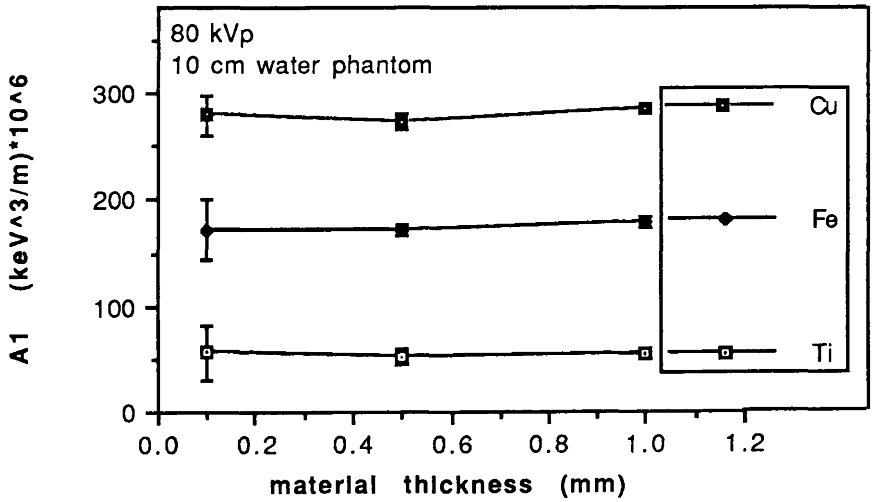
f) PHA semiconductor probe

iii) Effect of Phantom Thickness

The value of A_1 was measured for an 80 kVp incident spectrum and 1 mm material thickness as a function of water phantom thickness using the three dual energy probes. All measurements were corrected using the iterative beam hardening correction and are presented in figure 3.14. This figure shows the consistent fact that in the case of the split detector and the PHA NaI probes the experimental results are lower than the theoretical ones whereas the two sets of results are in agreement for the PHA HPGe case.

As shown in figure 3.14a, the theoretical and experimental results for A_1 decrease with increasing water thickness. This occurs because the dual energy sensitivity of the CsI/Cu/NaI probe decreases with increasing water thickness as shown in table 2.10.

Figures 3.14b and 3.14c show that using the PHA probes the experimental value of A_1 is independent of water thickness (10 to 20 cm) within the limits of experimental error.

Figure 3.14 Dependence of A_1 on water Phantom*

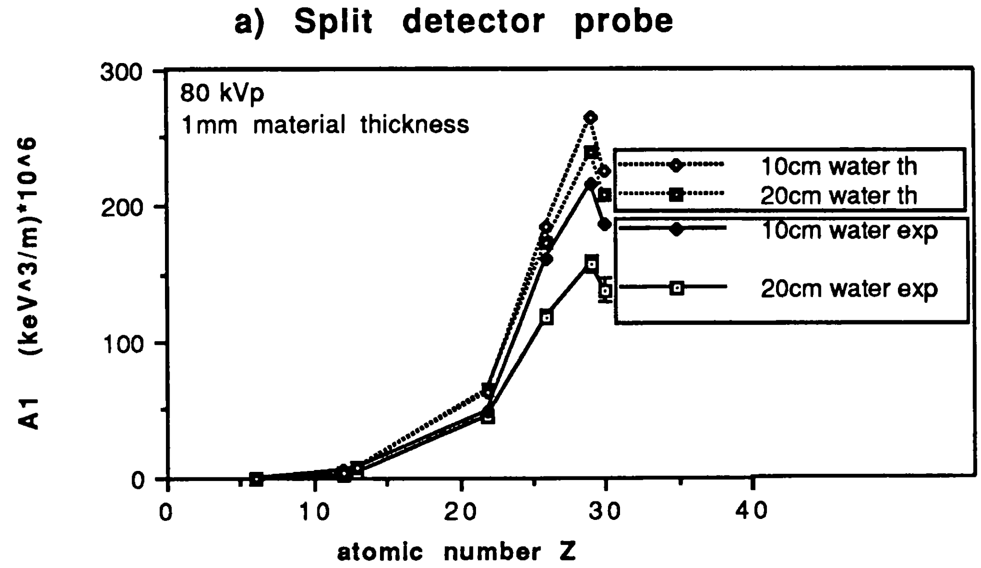

* th - theoretical ; exp - experimental

Figure 3.14

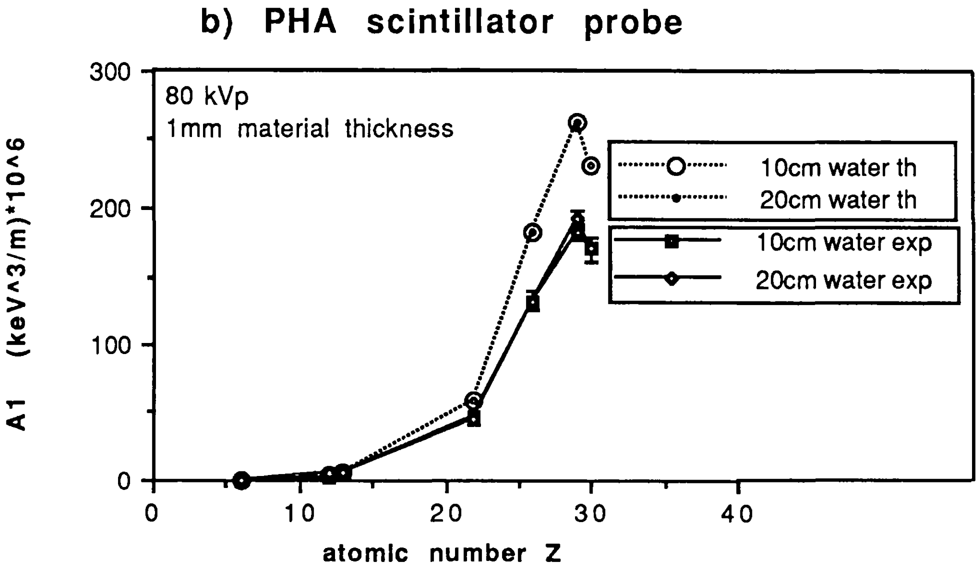
b) PHA scintillator probe
80 kVp
1mm material thickness
10cm water th
20cm water th
10cm water exp
20cm water exp
A1 (keV^3/m)*10^6
300
200
100
0
0
10
20
30
40
atomic number Z

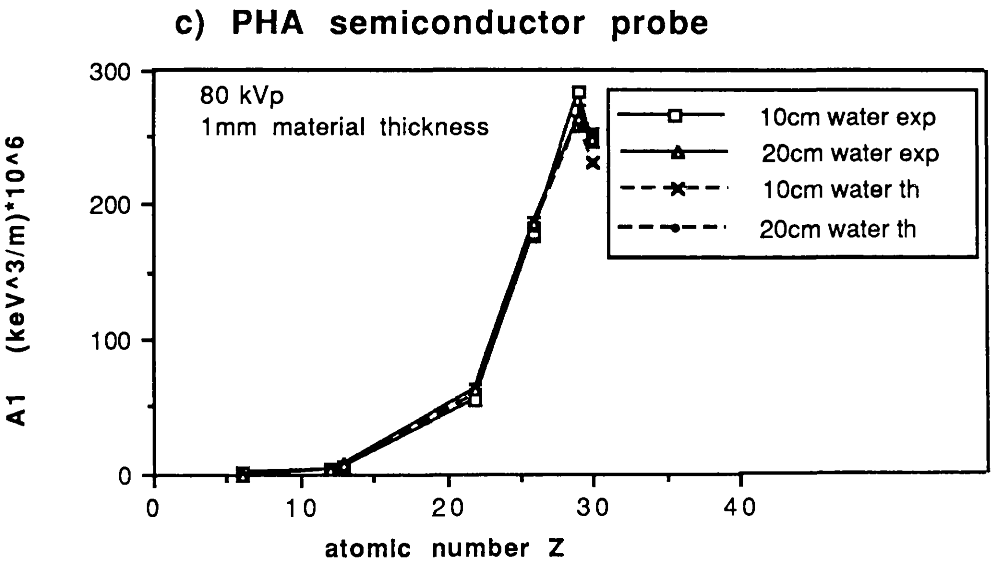
c) PHA semiconductor probe
80 kVp
1mm material thickness
10cm water exp
20cm water exp
10cm water th
20cm water th
A1 (keV^3/m)*10^6
300
200
100
0
0
10
20
30
40
atomic number Z

3.4.6 Comparison of the Dual Energy Probes

Two parameters, sensitivity and probability of success to distinguish between materials of different atomic number, were used for comparison of the dual energy methods. Also the effect of phantom and material thickness and other factors such as time of measurement are included in the comparison.

In order to carry out these comparisons the parameters need to be defined :

i) Sensitivity

The sensitivity which should not be confused with the DES is defined as the ability of the dual energy system to pick up differences in effective atomic numbers of materials. Thus, if a least square polynomial curve fitting is carried out between the value of the dual energy coefficient A_1 and the atomic number Z, the sensitivity is defined as the slope of the fitted curve caused by 1% change in Z at values of Z= 6 (C), 12(Mg), 13(Al), 22(Ti), 26(Fe) and 29(Cu). The results are summarised in table 3.3.

As explained previously, the effect of the increase of the DES with kVp for the split detector probe is reduced due to the rise in the effective energy of the absorbed spectrum by the CsI scintillator. This is confirmed by table 3.3 where 70 kVp gives the largest sensitivity for the split detector probe when high atomic numbers are considered.

Both PHA probes show the highest sensitivity at 80 kVp. This may be due to the selection of energy window sets carried out during dual energy analysis. In general, the HPGe probe proved to be the most sensitive of all the dual energy probes due to its superior energy discrimination.

For low atomic numbers (C, Mg, Al) all sensitivities are very similar. The definition of sensitivity does not take into account the experimental error. To take the latter into consideration another parameter, the probability of success is determined in the following subsection.

Table 3.3 A_1 Sensitivity

Dual energy probe	Incident spectrum	A_1^* sensitivity $(\text{keV}^3/\text{m})\ 10^6$					
		C	Mg	Al	Ti	Fe	Cu
Split detector	70 kVp	0.2	1.2	1.5	**11.6**	**25.9**	**45.5**
	80 kVp	0.1	0.8	1.0	9.9	23.2	43.1
	90 kVp	0.1	0.9	1.2	9.7	23.0	42.0
PHA NaI	70 kVp	0.1	1.1	1.4	7.7	14.1	21.4
	80 kVp	0.2	1.0	1.2	**10.9**	**25.9**	**47.6**
	90 kVp	0.1	0.9	1.1	8.5	18.5	31.9
PHA HPGe	70 kVp	0.2	1.2	1.5	13.5	32.0	58.7
	80 kVp	0.1	1.1	1.3	**15.0**	**39.5**	**78.7**
	90 kVp	0.1	1.1	1.5	15.3	38.1	72.4

* A_1 was measured for 10 cm water phantom and 1 mm material thickness

ii) Probability of Success

An estimation of the probability that one can distinguish between materials of different atomic Z even though experimental errors are present in the system is a very useful parameter in assessing the performance of the dual energy methods. One method of achieving this is to normalise the measured signal to the experimental standard deviation . If a normal distribution of the measured values of A_1 is assumed, a signal S(Z) arising from measuring material M(Z) will have a probability of 68.3% of lying between $S(Z) - \sigma$ and $S(Z) + \sigma$, where σ refers to the standard deviation of the experimental measurement. Similarly, increasing the limits to $S(Z) - 3\sigma$ and $S(Z) + 3\sigma$ interval will give a 99.7% probability of containing the true value of the signal.

Since in practice the choice of the number of calibration materials is limited, a neighbouring material is defined as the next available material with higher atomic number. The signal separation between two neighbouring materials (i.e. C & Mg, Mg & Al, Al & Ti, Ti & Fe and Fe & Cu) normalised to the standard deviation σ (σ being the largest of the two measurements) could be related to the probability of success that two materials can actually be distinguished by the dual energy measurement.

The probability in distinguishing between two neighbouring materials was calculated for the dual energy methods considering a 10 cm water phantom thickness and 1 mm material thickness. The results are shown in table 3.4.

Table 3.4 Probability of Success

Methods	Incident spectrum (kVp)	Probability of success (%)				
		C-Mg	Mg-Al	Al-Ti	Ti-Fe	Fe-Cu
Split detector	70	37.4	35.9	100	100	98.1
	80	39.6	46.2	100	100	99.9
	90	**44.5**	**63.7**	**100**	**100**	**100**
PHA NaI	70	**75.0**	**74.2**	**100**	**100**	**94.3**
	80	43.1	55.2	100	100	100
	90	50.4	40.4	100	100	98.3
PHA HPGe	70	**96.9**	**95.5**	**100**	**100**	**100**
	80	65.3	68.3	100	100	100
	90	57	57.6	100	100	100

The previous subsection revealed that for the split detector system, the x-ray tube high potential of 70 kVp results in the largest sensitivity. Unfortunately, the choice of a low kVp value is limited by the noise present in the system. A reduction in the x-ray tube operating voltage causes a reduction in the intensity and its penetrating power. Consequently, noise, and hence experimental standard deviation, are increased. This can be seen in table 3.4, where the probability of success in distinguishing between materials of low atomic numbers increases with higher kVp.

For low kVp, the PHA probes show higher probability of success than the split detector probe. In general, the probability of success for PHA probes decreases with increasing kVp. This rather surprising result may occur because the x-ray tube output is more stable at lower kVps resulting in smaller experimental error. The standard deviation, which includes not only the time variation of the x-ray tube but also any variation between subsequent exposures, may exceed the error due to the reduction of the intensity penetrating the patient. In contrast to the split detector probe which is operated in DC mode and registers all energies, the PHA probes detect a relatively narrow band of energies and it seems they are less prone to errors due to intensity reduction. At 70 kVp, the PHA HPGe detector shows the highest probability of success of all probes due to its high energy resolution.

For high atomic numbers, all three methods show almost 100% probability of success in distinguishing between different calibration materials.

iii) Summary and conclusions

Table 3.5 summarises the performance of the dual energy probes for the measurement of the dual energy number A_1 corrected for beam hardening. The three incident spectra considered were at 70, 80 and 90 kVp.

Using the PHA HPGe probe proves to be the most effective way to determine the dual energy number A_1 and hence the atomic number Z of the material considered. Not only does it offer the largest sensitivity and probability of success but it also shows little dependence on phantom thickness and only a few percent variation of A_1 with thickness for high atomic numbers materials.

The big advantage of the split detector probe is the speed of measurement.

Measuring one ray path merely takes the time required for A/D conversion and data read-out. For example an assembler routine averaging 100 measurements is finished in less than 100 ms. This method has potential for thickness of material exceeding 1 mm and depending on the accuracy required, a unique value of A_1 exists for atomic numbers up to Z=22 (~8% variation with phantom thickness).

Table 3.5 Performance of the Dual Energy Probes measuring A_1

	Split detector probe	PHA NaI probe	PHA HPGe probe
change in A_1 for material thickness change from 0.1 to 1 mm (80 kVp)	Fe : 2.7% Cu : 10%	Fe : 4% Cu : 11%	Fe : < 1% Cu : 3.5%
change in A_1 for water thickness change from 10 to 20 cm (80 kVp).	Ti : 8% Fe : ~26%	independent of phantom thickness within experimental error	independent of phantom thickness within experimental error
Sensitivity	optimised at 70 kVp	optimised at 80 kVp	greatest sensitivity of of the three methods at 80 kVp
Probability of success	best probability of success at 90 kVp	best probability of success at 70 kVp	largest probability of sucess of the three methods at 70 kVp
Speed (time)	< 100 ms	40 s	40 s
Convenience	Easy to manoeuvre, detector can be mobile	Easy to manoeuvre, detector can be mobile	Bulky, fixed detector

There appears to be little advantage in using the NaI PHA probe and therefore in chapter 4 and chapter 5 only two dual energy probes are considered; the split detector probe CsI/Cu/NaI because of its speed and easy implementation to a dual energy radiography scanner and, as a comparison, the PHA HPGe laboratory system because of its better performance.

CHAPTER 4 EFFECTS OF SCATTER IN A DUAL ENERGY PROCEDURE

X-ray scattered radiation is present in all radiological imaging techniques. It is regarded as an important problem causing degradation of image contrast. Like beam hardening, scatter introduces non-linearity into the logarithmic relationship between apparent transmission and absorber thickness (Vetter and Holden 1988). In dual energy procedures, scattered radiation emerging from a heterogeneous patient increases the detected intensity, which causes lesions or tissue under examination to appear less attenuating than they actually are. Therefore, a study of the effects of scattered radiation in dual energy techniques should be evaluated. Monte Carlo calculation is regarded as the most realistic method for the simulation of photon transport in a scattering medium. The principle aim of this study was to simulate on a computer the passage of x-ray photons through a test phantom, using Monte Carlo techniques, and then to compare the results of the obtained dual energy coefficient A_1 with those obtained experimentally under similar conditions. Unlike the narrow beam geometry computer model, the new approach will include the contribution of scattered radiation to the system.

4.1 Principles of Monte Carlo

4.1.1 Introduction

Monte Carlo techniques draw random numbers from known probability distributions to simulate a particular physical process. The two main sampling methods generally used are described by Raeside (1976) and are known as the direct method or inversion method, and the rejection technique. Monte Carlo methods have been widely applied to problems in the field of medical radiation physics concerning photon and charged particle transport such as dosimetry, detector evaluation and the effects of scattered radiation.

4.1.2 Random Numbers

Random numbers are generated to sample the probability distributions governing given processes. They may be obtained from sources which fall into one of the three main categories; either from specially constructed tables, by recording the output of some randomly fluctuating physical process such as electrical' Johnson' noise, or by calculation from a mathematical algorithm. The last method is the one almost always used. Tables have the disadvantage of requiring large amounts of storage (memory) and if numbers generated from electrical noise are used it is impossible to retrace steps in the calculation should this be necessary.

All Monte Carlo simulations require a supply of a high quality random numbers. The concept of using calculated random numbers needs some justification, as these numbers are often referred to as being "pseudo-random". The justification comes from the fact that mathematical algorithms can produce a series of numbers which pass specific randomness test equally as well as a random number series obtained by physical means. The random number generator used was G05CAF from the Numerical Algorithm Group Ltd library available on the Cray 1S at the University of London Computer Centre. This number generator has a non-repeating cycle of 2^{57} numbers.

4.1.3 Sampling Methods

The idea of direct sampling is simple, requiring only the inversion of the cumulative probability distribution arising from the process under study. If the probability density function for the variable x is f(x), then the cumulative probability F(X), the probability that a value obtained for x is less than X, is given by

$$F(X) = \int_{o}^{X} f(x)\,dx \qquad 4.1$$

A normalisation condition is placed on f(x) by requiring that F(X) lie between zero and unity. Thus

$$\int_{o}^{xm} f(x)\,dx = 1 \qquad 4.2$$

where xm is the maximum possible value of the variable x.

If a random number generated on the unit interval is denoted by r* (i.e. : $0 \leq r^* \leq 1$) then the variable may be randomly sampled from the distribution by inversion, by putting r* = F(X) and inverting to find X.

Although simple in principle, it may not always be easy to apply the direct technique. The cumulative probability distribution may, for example, be a very complicated mathematical function which is difficult if not impossible to invert. An alternative method is the rejection technique, so called because not all of the random samples generated are accepted. The principles underlying this method are described below :

Assume that a number of random samples $x_1, x_2, \ldots..$ are to be drawn from a distribution whose probability density is f(x), such that

i) $f(x) = 0$ for $x < u$ and $x > v$ and

ii) $f(x) < 1$ for $u < x < v$

as shown in figure 4.1.

Figure 4.1 Probability Distribution for Monte Carlo Rejection Sampling

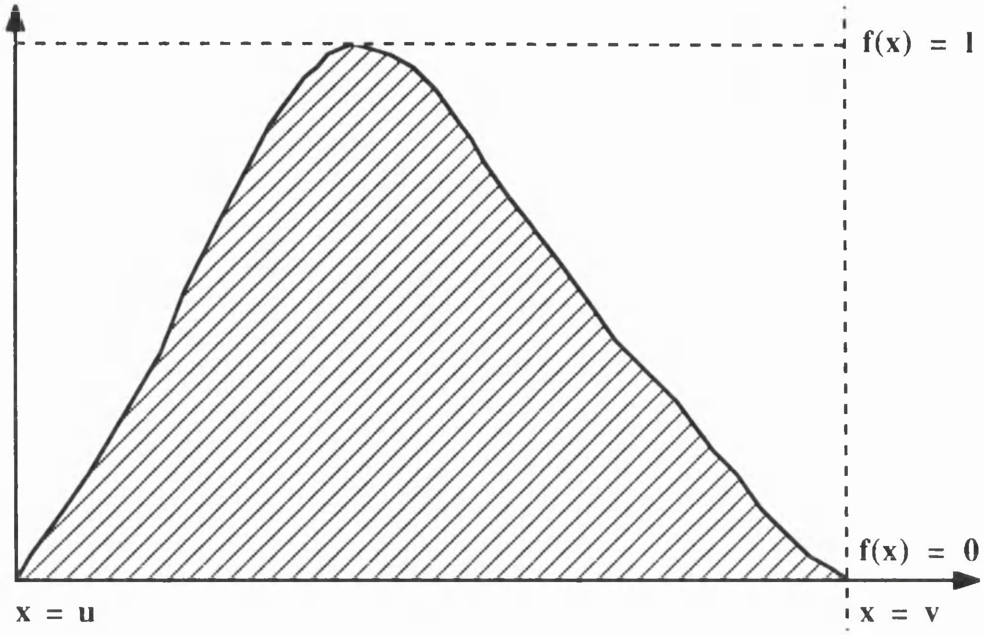

Consider now two uniform density distributions, p(a) = 1 / (v-u) and p(b) = 1 / (1-0). By drawing independent random samples from these, points (u +a_1, b_1), (u +a_2, b_2).... are generated where a_1, a_2.... and b_1, b_2.... are the values obtained from p(a) and p(b) respectively. These points will fall somewhere in the rectangle bounded by the lines x = u, x = v, f(x) = 0, and f(x) = 1, either above or below the curve f(x). Points above the curve are rejected, while those falling below it (i.e. points which for a given value of x have a value of b less than f(x) - shaded area) are used to generate the samples x_1, x_2.... from :

$$x_n = u + a_n \tag{4.3}$$

It is possible to show that this procedure is equivalent to random direct sampling from the probability density f(x) (Raeside 1976).

4.2 Application of Monte Carlo Techniques

Since the dominant photon scattering processes in the diagnostic energy range are Compton and coherent scattering, the following sections discuss Monte Carlo sampling of the energy and angular distribution of Compton scattered photons, and the angular distribution of coherent scattered photons.

4.2.1 Monte Carlo Sampling of Compton Scattered Photons

Pickard (1982) used both the inversion and rejection techniques to describe the photon behaviour following a Compton interaction. It was demonstrated that the rejection technique although more complicated was superior in its performance and so has been chosen in this work. The technique which was originally devised by Khan in 1956 and later used by Horrocks (1987) is described in the following:

The Klein-Nishina electronic angular differential cross-section for Compton scattering is given by

$$d\sigma = 0.5\, r_o^2 (\lambda_o / \lambda_1)^2 \left\{ \lambda_1 / \lambda_o + \lambda_o / \lambda_1 - 1 + \cos^2\theta \right\} d\Omega \qquad 4.4$$

where λ_o is the wavelength of the incident photon, λ_1 is the wavelength of the scattered photon after interacting with an unbound electron and $d\Omega$ is the solid angle. The Khan rejection technique is based on the transformation of equation 4.4 into a form relating to the probability of a scattered photon having a wavelength between λ_1 and $\lambda_1 + d\lambda_1$. This is obtained by evaluating :

$$d\sigma / d\lambda_1 = (d\sigma / d\Omega)\ (d\Omega / d\lambda_1) \qquad 4.5$$

Using Compton 's wavelength shift formula $\lambda_1-\lambda_o = (h/m_oc) (1-\cos\theta)$ and the expression $d\Omega = 2 \pi \sin\theta \, d\theta$, equation 4.5 can be written as

$$d\sigma = \pi r_o^2 (m_oc / h) \left\{\lambda_o / \lambda_1\right\}^2 \left\{\lambda_1 / \lambda_o + \lambda_o / \lambda_1 - 1 + \left[1 - (m_oc / h)(\lambda_1-\lambda_o)\right]^2\right\} d\lambda_1 \qquad 4.6$$

Using the well known scaling convention where Planck's constant h, the rest mass of the electron m_o and the velocity of light c, are all put equal to 1, equation 4.6 can be expressed as the probability density f for a given value of λ_o :

$$f(r \setminus \lambda_o) \propto (1 / r^2) \left[1 / r + r - 1 + (1 - \lambda_o r + \lambda_o)^2 \right] \qquad 4.7$$

where $r = \lambda_1 / \lambda_o$.

Raeside (1976) showed that equation 4.7 can be written as

$$f(r \setminus \lambda_o) \propto \left[(\lambda_o + 2) / (9\lambda_o + 2)\right] g_1(r)\, h_1(r) + \left[8\lambda_o / (9\lambda_o + 2)\right] g_2(r)\, h_2(r) \quad 4.8$$

where $g_1 = \lambda_o / 2$; $\qquad h_1 = 4 (1 / r - 1 / r^2)$

and $\qquad g_2 = (\lambda_o + 2) / (2r^2)$; $\quad h_2 = \left\{(1 - \lambda_o r + \lambda_o)^2 + 1 / r \right\} / 2$

The division of $f(r \setminus \lambda_o)$ is such that g_1 and g_2 are both probability densities where

$$\int_{1}^{(1+2/\lambda o)} g_1(r)\, dr = \int_{1}^{(1+2/\lambda o)} g_2(r)\, dr = 1 \qquad 4.9$$

known as track 1 and track 2 respectively. In scaled units, Compton's wavelength shift formula can be reduced to $\lambda_1 - \lambda_o = 1 - \cos\theta$. Thus λ_1 will clearly range in value from λ_o to $\lambda_o + 2$, i.e., r may take on values from 1 to $1 + 2 / \lambda_o$.

The rejection technique is applied as follows :

Firstly, either track 1 or track 2 is selected by the generation of a random number r*,

if $0 \leq r^* \leq (\lambda_o + 2) / (9\lambda_o + 2)$ track 1 is selected

if $8\lambda_o / (9\lambda_o + 2) \leq r^* \leq 1$ track 2 is selected

Once the track has been determined, the relevant cumulative probability G_1 or G_2 is sampled by inversion where

$$G_1 = \int_{1}^{\rho} g_1(r)\, dr = 0.5\, \lambda_o\, (\rho - 1)$$

$$G_2 = \int_{1}^{\rho} g_1(r)\, dr = [(\lambda_o + 2) / 2]\, (1 - 1 / \rho)$$

to obtain $\rho = 1 + 2r^* / \lambda_o$ for track 1 or $\rho = (\lambda_o + 2) / [\lambda_o + 2(1 - r^*)]$ for track 2.

This value of ρ is then kept or rejected according to the rejection rules :

if $r^* \leq h_1$ accepted for track 1

if $r^* \leq h_2$ accepted for track 2

If ρ is accepted, the scattered photon wavelength is simply given by

$$\lambda_1 = \rho \lambda_o.$$

The photon polar scattering angle is then determined using the Compton wavelength shift formula where λ's are still in scaled units

$$\theta = \cos^{-1} (1 + \lambda_o - \lambda_1)$$

The azimuthal scattering angle δ is determined randomly between $-\pi \leq \delta \leq \pi$ by assuming an isotropic azimuthal distribution.

The scattered photon energy when expressed in keV is given by

$$E_1 = 511.006 / \lambda_1$$

Figure 4.2 Comparison of the Khan Rejection Technique with the Klein-Nishina Distribution at 40 keV

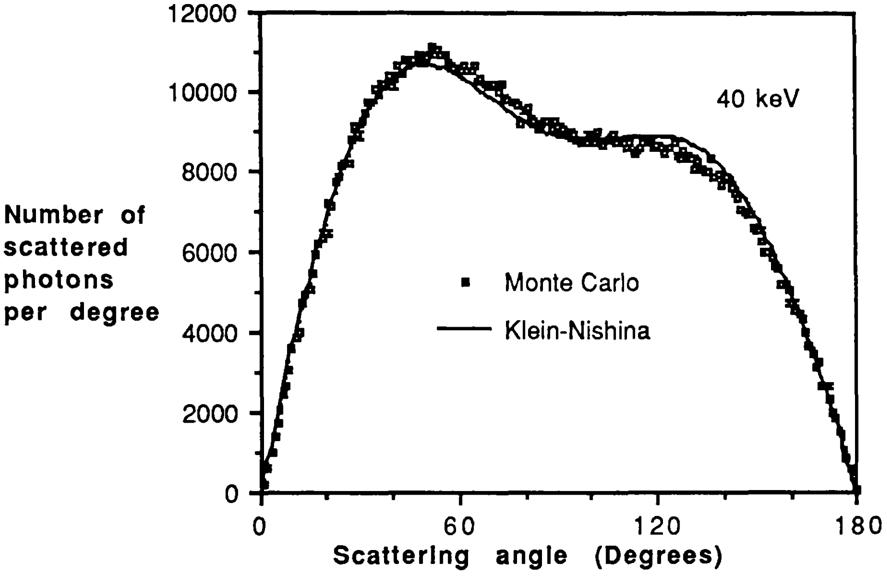

Fourty keV was selected as the maximum number of photons in a diagnostic x-ray spectra occur around this energy. Figure 4.2 shows that the Monte Carlo programs compare adequately with the theoretical angular distribution of Compton scattered photons calculated from the Klein-Nishina equation.

4.2.2 Monte Carlo Sampling of Coherent Scattered Photons

The contribution of coherent scatter to the total scattered radiation is always considered of minor importance due to its low overall intensity (~1% of the total attenuation). However, the scattering of photons of energies < 100 keV at angles of the order of 10° and less is dominated by the coherent process. Due to the collimation of the dual energy probes considered (1 mm or 2 mm pinhole size) which gives a small opening angle, mainly forward scattered radiation will be recorded. Thus, an understanding of coherent scatter especially at very low angles (< 10°) is of prime importance in this situation.

If coherent scattering occurs, the scattered photon retains its original energy and the only parameter of concern in the case of a Monte Carlo simulation will be the photon scattering angle. The differential cross-section per unit solid angle for coherent scattering is given by :

$$d\sigma_{coh}(\theta) / d\Omega = (d\sigma_T(\theta) / d\Omega)\ F^2(x,Z) \qquad 4.10$$

where $d\sigma_T(\theta) / d\Omega = 0.5\, r_o^2\ (1 + \cos^2\theta)$ is the differential Thomson cross-section per electron for elastic scattering from an unpolarised beam, r_o is the classical radius of the electron, θ is the scattering angle of the photon, defined as the angle between the direction of flight before and that after the interaction and $F(x,Z)$ is the atomic form factor (Hubbell *et al* 1975) which accounts for electron binding effects.

Here x is the momentum transfer defined as

$x = (1 / \lambda) \sin\theta/2$ 4.11

where λ is the wavelength of the incident radiation and Z is the atomic number.

i) Form Factors

The form factor squared, $F^2(x,Z)$, represents the probability that the Z electrons of the atom take up a recoil momentum without absorbing any photon energy. If the incident photon momentum is $h.\underline{k}_i$ and scattered photon momentum is $h.\underline{k}_f$ then the momentum transfer expressed in units of inverse length is (Jackson and Hawkes 1981) :

$$\underline{q} = \underline{k}_i - \underline{k}_f \qquad 4.12$$

Since the photon does not change energy in coherent scattering then

$$|ki| = |kf| = 1/\lambda \qquad 4.13$$

so that the change of momentum transfer of the photon corresponds to

$$h.q = 2\ (h/\lambda) \sin\theta/2 = 2\ h.x \qquad 4.14$$

as this not only depends on the energy of the incident photon but also on the scattering angle. Hubbell *et al* (1975) have tabulated the form factors for elements and for coherent scattering as a function of the momentum transfer, x. It has to be noted however, that near absorption edges, resonance effects occur, and the coherent form factor depends explicitly on the energy of the incident photon as well as on x (James 1962). However, since the energies used in diagnostic radiology are far above absorption edges for the materials under consideration, this effect can be ignored.

The atomic form factor F(x,Z) decreases rapidly from a maximum value of Z to zero as x increases from zero to infinity, i.e., F(x,Z) is manifested by a forward peak at

$\theta = 0°$. The molecular form factor squared F^2m can be expressed as follows :

$$F^2m = \Sigma^N n_i F^2i\ (x,Z_i) \qquad 4.15$$

where N, n_i and F_i are the number of different kinds of atoms, the number of atoms of element i in the molecule and the atomic form factor for element i respectively. F^2m is obtained by assuming that the coherent cross-section of individual atoms combine independently. It has been reported however (Johns and Yaffe 1983, Morin and Berroir 1983), that for small scattering angles the differential coherent scattering probability for liquid and solid materials is not peaked at zero as in the case for free atoms (suggested by atomic form factors). They attribute this fact to the intermolecular interference which leads instead to a maximum scattering probability at a non-zero scattering angle (about 4° for 60 keV photons in liquid water (Johns and Yaffe)). Muntz *et al* (1983) showed experimentally that the peak position of scattering is very material dependent and state that this is due to changes in average intermolecular spacing for different materials.

However, at higher values of incident photon energy or momentum transfer x, the molecular form factor Fm approaches to that predicted on the basis of scattering of free atoms as given by equation 4.15 (Johns and Yaffe 1983). This is shown in figure 4.3.

Persliden and Carlsson (1986) have made Monte Carlo calculations of the small angle distribution of scattered photons for diagnostic energies, using the intermolecular form factor from Morin (1982). Comparison with experimental results of Muntz *et al* (1983) for water indicates good agreement with the peak position and shape; a discrepancy is found however, between the ratio of the scattering at the peak of the distribution (~4°) and 2° (approximately the minimum value of the valley). This ratio was found to be 6.5 and 2 for Persliden and Carlsson calculations and Muntz *et al* measurements, respectively. Up to now it is not clear whether these properties of coherent scattering at small angle are of any significance in situations typical for diagnostic radiology, i.e. for angular range 0-180° and for photon energies 20-140 keV.

Figure 4.3 Form Factors for Water

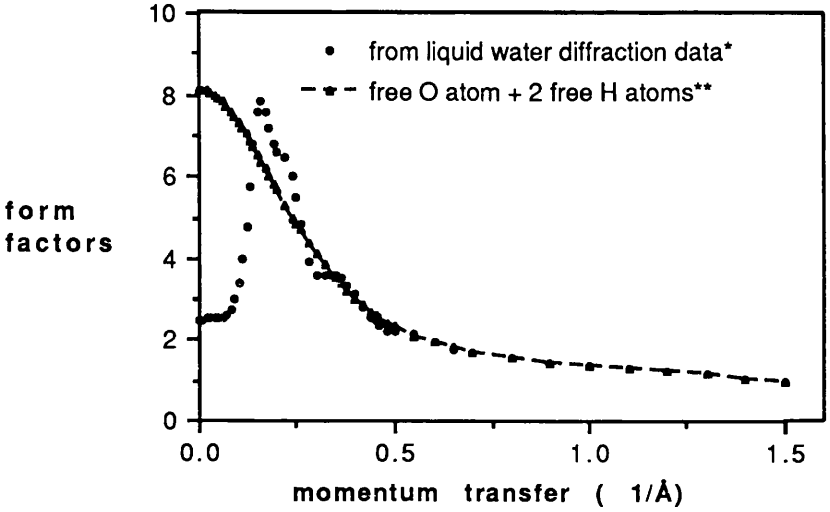

*Form factors for liquid water at 20°C tabulated by Morin (1982).

** Atomic form factors tabulated by Hubbell *et al* (1975).

It should be noted that although the differential cross-section for small θ is quite sensitive to the method used to obtain the coherent form factor (using the atomic sum approximation or molecular one), the integrated cross-section is not. The total coherent cross-section for water assuming independence between the O and H atoms, is within 9% of that tabulated by Morin (Johns and Yaffe), leading to less than 1% difference in the total cross-section.

ii) Coherent Sampling

A Monte Carlo technique that combines inversion and rejection sampling devised by Zerby (1963) was used to describe the photon behaviour following a coherent interaction. A similar method has been described by Chan and Doi (1983) and in this thesis the technique used by Williamson and Morin (1983) was employed as it was more easily adapted to our program. Neitzel *et al* (1985) used a different method where the scattering angles are determined in advance and tabulated for use during the sampling procedure. However, although this procedure avoids the sampling algorithm during Monte Carlo execution, it suffers from the disadvantage of requiring large amounts of computer memory.

In the method employed by Williamson and Morin, $d\sigma_{coh} / d\Omega$ is regarded as the product of two probability density functions such that

$$d\sigma_{coh} / d\Omega \propto g \, . \, h \qquad 4.16$$

where $g = F^2(x,Z)$ and $h = (1+ \cos^2\theta) / 2$

and h is normalised to unity.

Given a random number r* on the unit interval, it is possible to generate a random variate X* distributed according to $d\sigma_{coh} / d\Omega$ by the inversion rejection technique as follows :

i) X* is defined such that

$$r^* = \left(\int_0^{X^*} F^2 \, dx \right) / \left(\int_0^{xm} F^2 \, dx \right) \qquad 4.17$$

where $xm = 1 / \lambda = 0.0801E$ with E expressed in keV and x expressed in Å^{-1}.

As the value of xm depends on the incident energy, this makes it very inconvenient during Monte Carlo execution. However equation 4.17 can be written as :

$$r^* \left\{ \left({}_{o}\int^{xm} F^2 \, dx \right) / \left({}_{o}\int^{\infty} F^2 \, dx \right) \right\} = \left\{ \left({}_{o}\int^{X^*} F^2 \, dx \right) / \left({}_{o}\int^{\infty} F^2 \, dx \right) \right\}$$

4.18

Since the integral of F^2 converges as $X^* \rightarrow \infty$ and monotically approaches unity as X^* tends to xm, the normalisation term $\left({}_{o}\int^{xm} F^2 \, dx \right) / \left({}_{o}\int^{\infty} F^2 \, dx \right)$ takes on values close to unity and its evaluation can be omitted by adding the condition $X^* \leq xm$.

Equation 4.18 was calculated by numerically integrating F^2 using the trapezoidal rule over the momentum transfer x incremented according to Hubbell's tabulation of F(x,Z). The highest value of momentum transfer was set at x = 10 $Å^{-1}$, i.e.

$$r^{*\prime} = \left({}_{o}\int^{X^*} F^2 \, dx \right) / \left({}_{o}\int^{10} F^2 \, dx \right) \qquad 4.19$$

For E = 90 keV (maximum energy used in our study) xm correspond to 7.26 $Å^{-1}$ which is well below the limit set at 10 $Å^{-1}$.

ii) Once the value of X^* is determined, the photon scattering angle is calculated using equation 4.11

$$\sin \theta/2 = X^* \lambda \qquad 4.20$$

and the acceptance criterion is :

if $r^{*\prime\prime} \leq h$ ie $r^{*\prime\prime} \leq (1 + \cos^2\theta) / 2$ then scattering angle is accepted.

If not, generate a new random number and repeat process i) and ii).

It has to be noted that the coherent scattering angle θ corresponds to a polar angle. As in the Compton case, the azimuthal scattering angle δ is determined randomly between $-\pi \leq \delta \leq +\pi$.

Figure 4.4 Comparison of the Inversion Rejection Technique with the Coherent Angular Distribution for Water at 40 keV

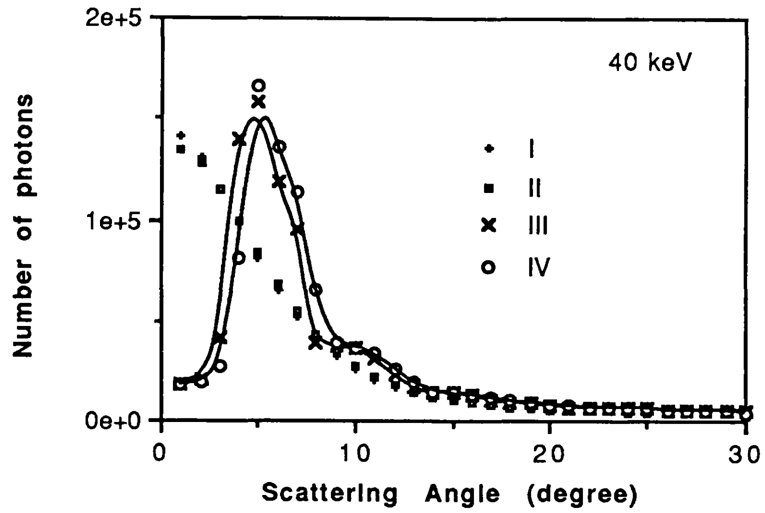

I and II - analytical calculation and Monte Carlo results respectively of coherent angular distribution using atomic form factors.

III and IV - analytical calculation and Monte Carlo results respectively of coherent angular distribution using liquid water form factors.

In figure 4.4, the comparison between the analytical coherent angular scatter distribution of water and that of Monte Carlo results is made at 40 keV. Two types of form factors are considered; the atomic form factors of water using the free atom approximation and liquid water form factors tabulated by Morin (1982).

When atomic form factors of water are employed both the theoretical and Monte Carlo results show good agreement and justify our confidence in the inversion rejection technique. For the method using liquid water form factors, the fit is slightly less good than the free atom approximation but is still adequate, and both the analytical expression and Mont Carlo results show the effect of intermolecular interference. The greatest effect is for scattering near $\theta = 0°$, for which there is almost complete destructive interference. This is a well known effect seen in diffraction studies on amorphous substances such as water (James 1962).

Clearly a significant difference occurs at low angles between the differential cross section calculated using the liquid water from factors and that using the atomic form factors. This emphasises the need for using molecular data when possible to simulate coherent scattering at very low angles. It is important to note however, that for scattering angles higher than 8-10°, the liquid water data converges upon the curve for free atom approximation case.

4.3 Monte Carlo Computer Model

4.3.1 Introduction

The phantom used in the Monte Carlo photon transport routine consists of a large block of perspex to simulate soft tissue and a material (usually metal) to simulate the tissue under examination. Each medium is described by the quantities given in table 4.1.

Attenuation data was obtained from Storm and Israel (1970) and the atomic form factors were taken from the tabulation given by Hubbell *et al* (1975). Perspex form factors were determined in two ways in order to study the difference caused by using the free atom approximation and molecular method into the determination of A_1. These are:

i) the perspex (methyl methacrylate $(C_5H_8O_2)n$) was assumed to be mono-molecular, i.e. $n = 1$, and its molecular form factor factor was calculated using the free atom approximation given by equation 4.15.

ii) As no data would seem to be available for perspex molecular form factors we have utilised the liquid water form factors given by Morin (1982). Although the x-ray diffractometer measurement carried out by Kosanetzky *et al* (1987) showed that the cross-section peaks in water and perspex are different, it is the fact that both maximum peaks are at a non-zero scattering angle which is of prime importance to our investigation. Thus, although it might not mimic the situation exactly, it does include the important feature of less coherent scatter at small angles.

Table 4.1 Physical Properties of Each Medium

Physical parameter	Units
Total linear attenuation coefficient	m-1
Relative photoelectric interaction probability (τ / μ)	
Relative coherent interaction probability (σ_{coh} / μ)	
Momentum transfer	$Å^{-1}$
Form factor squared	
Density	kg/m^3
Thickness	m

The Monte Carlo model is described in figure 4.5. The material was positioned at the two extremities of the phantom (position 1 and position 2) to look at the maximum effect that material positioning can cause to the system under scatter investigation.

Figure 4.5 Monte Carlo Computer Model

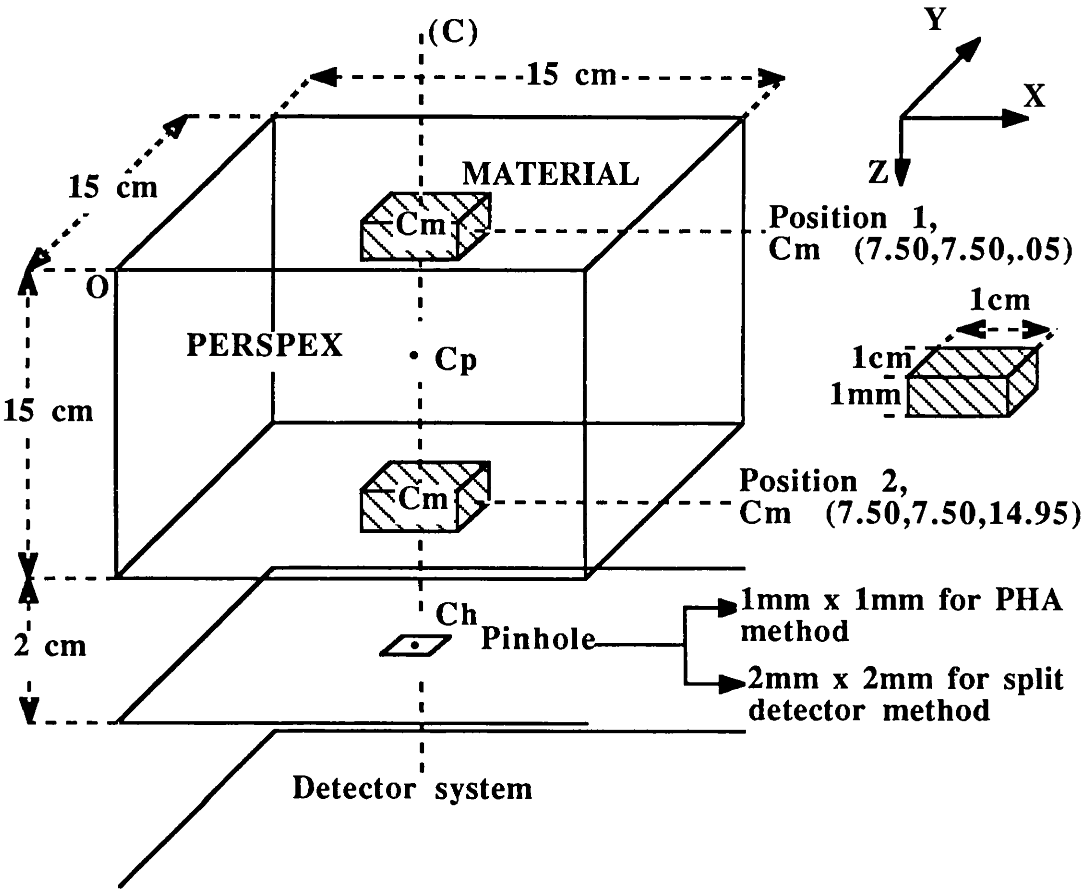

It has to be noted that the centre of the calibration material medium Cm, the centre of perspex medium Cp and the centre of the pinhole Ch are all aligned.

4.3.2 Photon Life Histories

The important aspects of the methods used to trace the photon interactions and the recorded data are given in the following subsections.

i) Initial Photon Conditions

In a clinical application for localised tissue characterization during fluoroscopy, the position of the detector probe would be accomplished by visualising the movement of the probe on the TV monitor of the image intensifier system. Therefore a large incident x-ray field is needed and this must be considered in the Monte Carlo model. This will simulate a more realistic approach to the clinical situation and will demonstrate the full contribution of scattered radiation to the system.

The program considers a polyenergetic x-ray spectrum. The spectral data was taken from Birch *et al* (1979).

Figure 4.6 Incident radiation

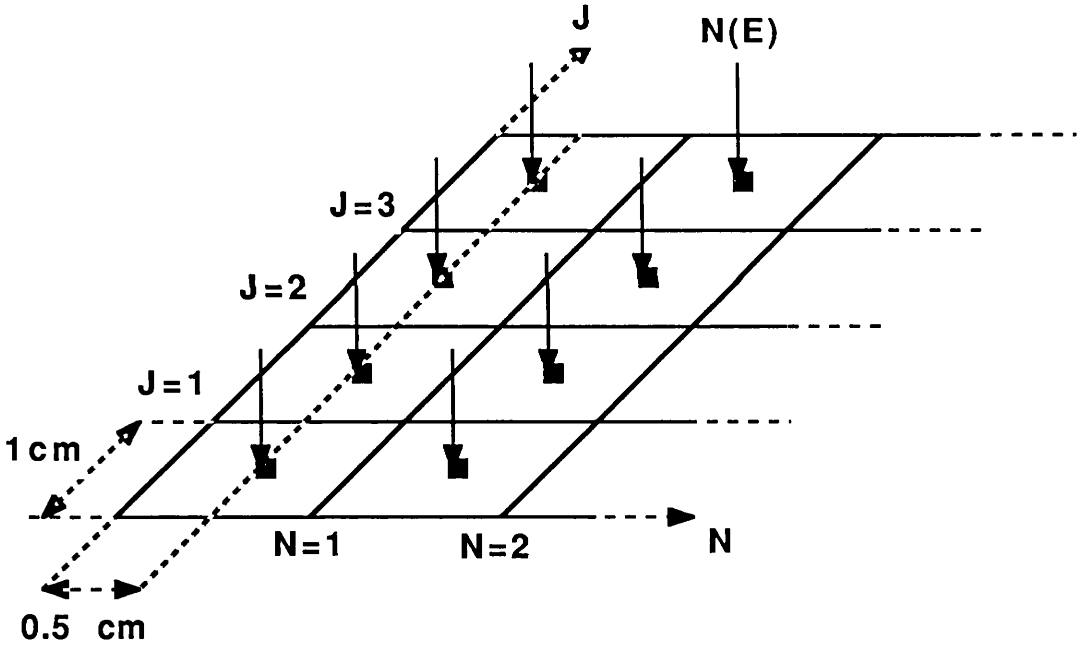

N(E) is the incident spectrum.

Total number of incident photons = 13 x 13 x N(E) ≅ 16 million photons.

A large x-ray field is simulated by dividing the phantom top surface into a (13 x 13) matrix of pixels 1 cm^2 each. The incident photon is normal to the phantom surface and enters at the centre of each pixel, as shown in figure 4.6.

ii) Interaction site

The distance d to the next interaction site in a homogeneous medium is given by Monte Carlo inversion sampling of the exponential photon attenuation law (Cashwell and Everett 1959) :

$$d = - [\ 1/\mu(E)\ ] \ln r^*$$

where $\mu(E)$ is the linear attenuation coefficient of the medium for a photon energy E and r* is a random number uniformly distributed between 0 and 1. However, the model under consideration is inhomogeneous, consisting of two different media with different attenuating properties. To tackle the problem of inhomogeneity the following procedure is adopted :

The first computed distance to the interaction in a medium i will be given by

$$d_1 = - [\ 1 / \mu_i(E)\ ] \ln r^*$$

The coordinates of the new interaction site are then given by

$$X_1 = X_o + U\, d_1$$

$$Y_1 = Y_o + V\, d_1$$

$$Z_1 = Z_o + W\, d_1$$

where X_o, Y_o and Z_o are the initial co-ordinates.

These coordinates are then tested to determine whether the interaction has occured within the medium i of dimension $[X_i]\text{x}[Y_i]\text{x}[Z_i]$. If $X_1 \neq [X_i]$ or $Y_1 \neq [Y_i]$ or $Z_1 \neq [Z_i]$ then the photon has crossed medium i without interacting and therefore its co-ordinates has to be recomputed. The photon is taken back along its path to the borderline position $P(X_b,Y_b,Z_b)$ where the photon had passed from medium i to another medium i +1. Then a new interaction distance is computed starting from $P(X_b,Y_b,Z_b)$ according to the following equation

$$d_2 = - [\ 1/\mu_{i+1}(E)\ ] \ln r^{**}$$

where r** is a different random number. So the new co-ordinates of the interaction site are :

$$X_1 = X_b + U\, d_2$$

$$Y_1 = Y_b + V\, d_2$$

$$Z_1 = Z_b + W\, d_2$$

These steps are carried out until an interaction occurs within the phantom or until the photon exits the phantom. The above procedure for treating media interfaces was validated by Horrocks (1987) by comparing the transmitted photons through two medium, one consisting of a homogeneous medium of material m and one containing two identical materials m with an interface. The transmitted photons in both cases showed the same distribution.

iii) Direction Cosines

As shown by Cashwell and Everett (1959), if the direction cosines of the photon before an interaction at point P(X, Y, Z) were U, V, W (figure 4.7), then after interaction the new direction cosines are given by

$$U_1 = \Big[\ (W\, U \sin\theta \cos\delta) - (V \sin\theta \sin\delta)\ \Big] / (1 - W^2)^{1/2} + U \cos\theta$$

$$V_1 = \left[(W\, U \sin\theta \cos\delta) + (U \sin\theta \sin\delta) \right] / (1 - W^2)^{1/2} + V \cos\theta$$

$$W_1 = - \sin\theta \cos\delta\, (1 - W^2)^{1/2} + W \cos\theta \qquad 4.21$$

where θ is the polar scattering angle and δ is the azimuthal scattering angle. If abs(W) = 1 the equations in 4.21 cannot be solved. Therefore in cases abs (W) > .99 they were replaced by the following equations

$$U_1 = \sin\theta \cos\delta$$

$$V_1 = \sin\theta \sin\delta$$

$$W_1 = W \cos\theta \qquad 4.22$$

Figure 4.7 Direction Cosines

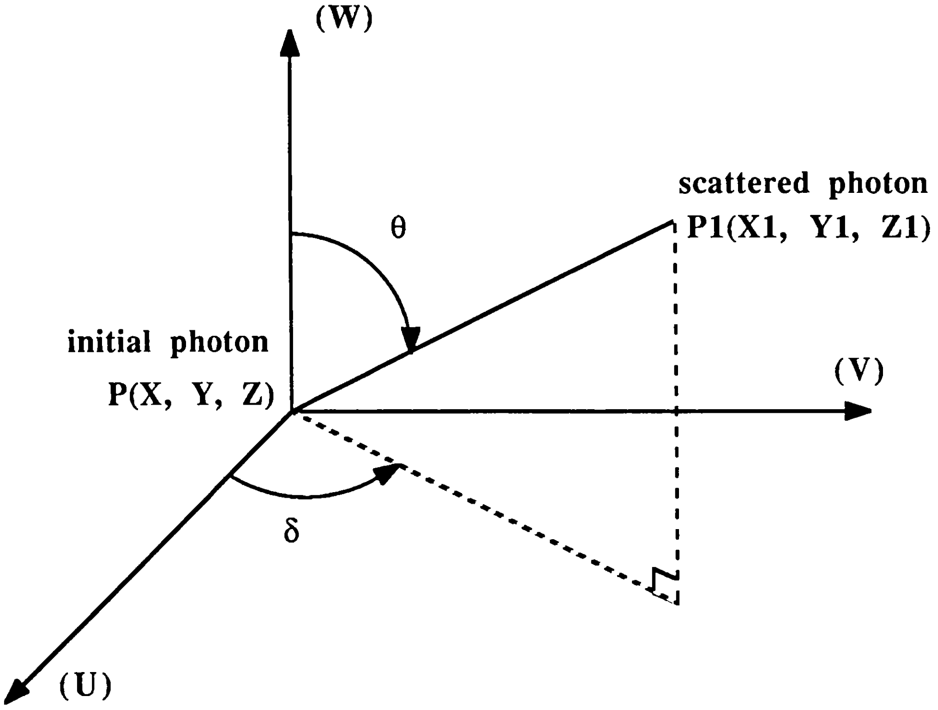

The coordinates P_1 (X_1, Y_1, Z_1) of the next interaction are then given by

$$X_1 = X + U\,d$$

$$Y_1 = Y + V\,d$$

$$Z_1 = Z + W\,d$$

where d is the distance to the next interaction.

iv) Type of Interaction

Having determined the interaction site, it is necessary to select the type of photon interaction. In the energy range considered, three different types of photon interaction are dominant namely photoelectric effect, Compton scattering scattering and coherent scattering.

a) Photoelectric Interaction

For the purpose of this study, the photoelectric interaction is regarded as a total absorption process, i.e. characteristic x rays are neglected because these energies are low for materials such as perspex. Even for the highest atomic number considered (Z=29) the energy of the fluorescence x rays is below 20 keV which was chosen to be the cut-off energy in our calculation of photon histories. Therefore, a photon history ends after the first photoelectric event.

b) Compton scattering

The Klein-Nishina formula was derived for the interaction of a photon with a free electron. In order to take into account the effect of electron binding on the differential cross-section of incoherent scattering, the Klein-Nishina formula should be corrected by the incoherent scattering function. The incoherent scattering function of an atom represents the probability that an atom will be raised to any excited or ionised state when a photon imparts a recoil momentum to an atomic electron. Chan and Doi utilised a rejection technique for sampling the angular distribution of Compton scattered photons including the incoherent scattering function. However, since the efficiency of their technique decreases with increasing energy (51% at 80 keV for perspex) the Khan sampling method was more preferable. Furthermore, due to lack of data on the incoherent scattering functions for a molecule (only atomic incoherent scattering functions are available (Hubbell *et al* (1975)) the final choice was to use the Khan rejection technique and so omit the above correction. As already described in section 4.2.1, the Compton scattering angle and the energy of the scattered photon are determined with this technique.

c) Coherent Scattering

Using the inversion rejection technique devised by Zerby in 1963 (cf. section 4.2.2b), the coherent scattering photon is determined.

A Monte Carlo decision on the nature of the interaction is made by looking at the relative probability of the photoelectric event (τ / μ) and the relative probability of the coherent scattering (σ_{coh} / μ) according to :

if $r^* \leq \sigma_{coh} / \mu$ then coherent scattering event occurs,

if $\sigma_{coh} / \mu < r^* \leq \sigma_{coh} / \mu + \tau / \mu$ then photoelectric absorption occurs and

if $r^* > \sigma_{coh} / \mu + \tau / \mu$ Compton scattering occurs.

where r^* is a random number uniformly distributed between 0 and 1.

v) The Recorded Events

If no photoelectric interaction occurs, the transmitted or scattered photon is traced till it exits the phantom. Once the photon is collected by the appropriate detector system (semi-conductor or split detector), i.e. the photon goes through the pinhole as represented in figure 4.8, narrow beam geometry is assumed. Once the photon goes through the pinhole, it is followed to see if it intersepts with the face of each detector.

Figure 4.8 Opening Angle Correction

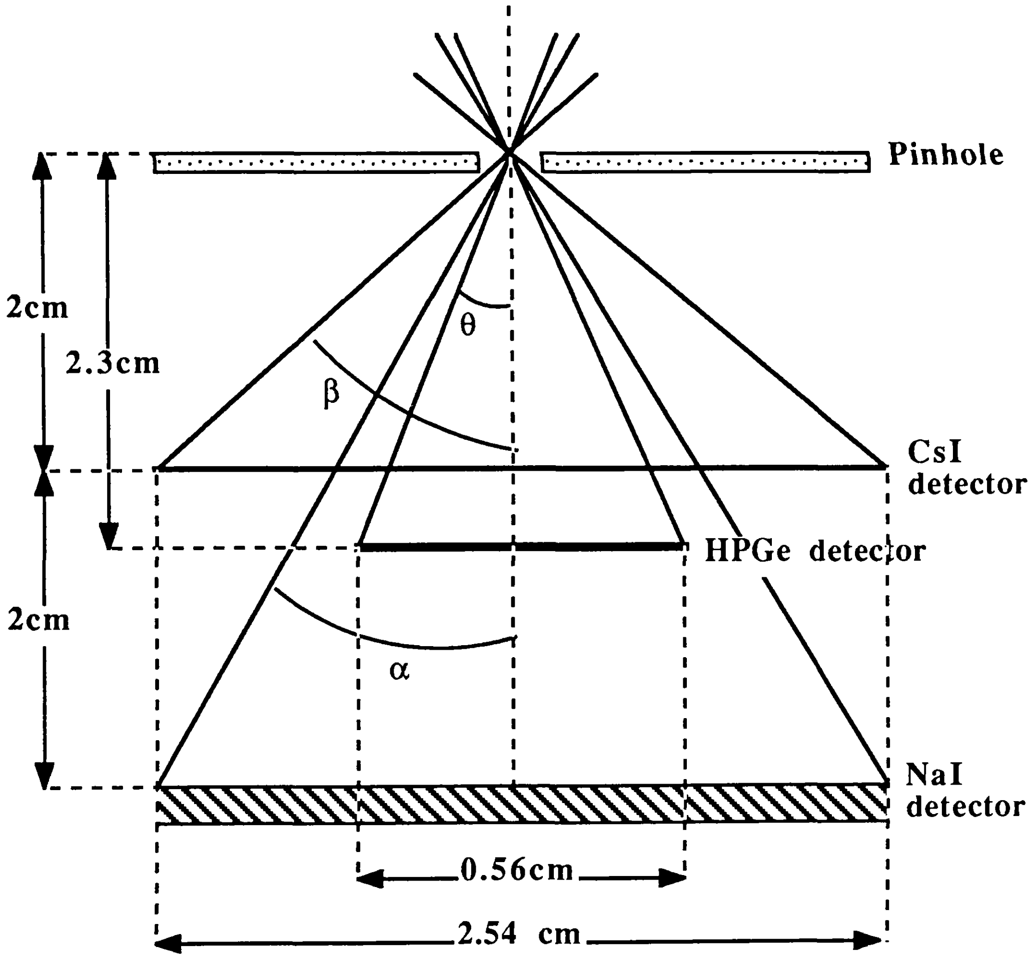

θ, α and β correspond to the half opening angle for HPGe detector, NaI scintillator and CsI scintillator respectively. The pinhole size is 1 mm for the semiconductor and 2 mm for the split detector probe.

The opening angle correction was carried out as follows :

i) 2θ opening angle correction for PHA probes. The HPGe detector was assumed to be 100% efficient.

ii) - 2β opening angle correction for the top CsI scintillator and

- 2α opening angle correction for the bottom NaI scintillator after being filtered by the CsI scintillator and the copper filter.

4.4 Results from the Monte Carlo Simulation

The flow chart of the Monte Carlo computer program is presented in figure 4.9.

4.4.1 Program Output

The following parameters were obtained from the Monte Carlo program :

a)- The recorded total number of multiple scatter photons compared to single scatter photons. This data was recorded to study the contribution that multiple scatter makes to the signal. If single scatter is the predominant effect, a simpler analytical model might be adequate to assess the scatter contribution to the detectors.

- The recorded total number of each type of interaction namely single coherent scattering and single Compton scattering are compared.

These are discussed in section 4.4.2.

Figure 4.9 Flow Chart of the Monte Carlo Program

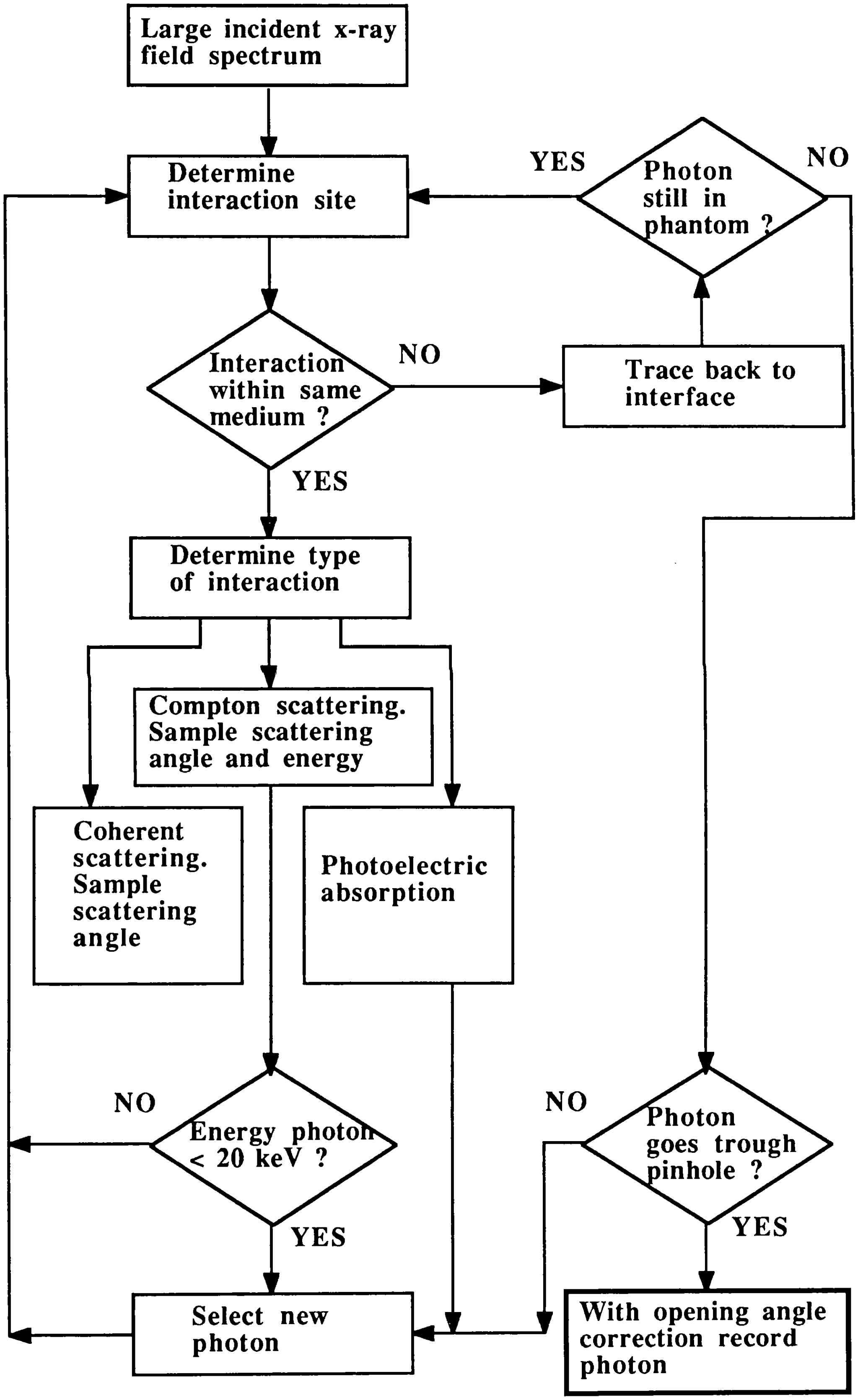

b) The dual energy number A_1 was computed considering

i) The PHA probe : the calibration material was positioned at the top and bottom surface of the Monte Carlo model. In both cases, the atomic form factors and liquid water form factors were incorporated during the execution of the program.

ii) A similar study was performed for the split detector probe.

All these results are given in section 4.4.3.

c) The dependence of scattered radiation on incident spectra was evaluated by considering both the PHA probe and the split detector probe. The results for A_1 are shown in section 4.4.4.

d) The contribution of scattered radiation to the detected signal and its dependence on phantom and examined material thickness changes was investigated. The values of A_1 which were determined under these conditions are given in section 4.4.5.

Following the theoretical consideration of the dual energy analysis procedure (cf. section 1.5) two paths were needed; one path corresponded to background measurement and the other one included material under investigation. For case b), c) and d) background calculations were made by shifting the detector system from the central axis C (figure 4.6) by 2 cm to make sure that the primary beam went through soft tissue only.

In the following discussion the top position of the calibration material is referred as position 1 and bottom position as position 2.

4.4.2 Multiple Scatter and Type of Interaction

In tables 4.2 and 4.3 the following notations were adopted :

PHA-f, for PHA method with free atom approximation, PHA-l, for PHA method using liquid water form factors,

SDM-f, for split detector method with free atom approximation and

SDM-l, for split detector method using liquid water form factors.

Table 4.2 Multiple Scattering Compared to Single Scattering (MS/S)

				(MS/S)*			
	mode	C	Mg	Al	Ti	Fe	Cu
calibration material position 1	PHA-f	2.5	2.0	3.0	4.5	2.7	2.4
	PHA-l	2.0	2.7	1.7	1.8	3.7	1.2
calibration material position 2	PHA-f	1.1	1.1	1.1	1.2	1.3	1.3
	PHA-l	1.3	1.2	1.5	1.2	1.4	1.2
calibration material position 1	SDM-f	2.1	2.6	2.1	2.3	2.3	2.1
	SDM-l	1.8	1.9	1.8	1.8	1.9	1.7
calibration material position 2	SDM-f	1.3	1.3	1.2	1.4	1.5	1.7
	SDM-l	1.7	1.4	1.6	1.5	1.5	1.5

*Only the recorded photons which fall within the corresponding opening angle are accepted.

From table 4.2 we can see that the predominant scattering in the Monte Carlo computer model is multiple scattering. However, when the calibration material is situated at position 2, multiple scatter is reduced considerably. This can be explained by the fact that multiple scatter is predominantly multiple Compton scatter. Multiple coherent scatter is negligible since the mean free path of 60 keV photons between elastic scatter events is approximately 50 cm in water (Harding *et al* 1987). Since the Compton scattered photons carry less energy than the original photons and have larger scattering angles, this results in a longer path length for the photon to travel in the phantom. Thus, these reduced energy photons are stopped more easily by the calibration material situated in position 2.

In general terms, for calibration materials placed in position 1, use of the liquid water form factors produces less scatter than the free atom approximation. This is true for both PHA and split detector methods. For position 2, multiple scatter is of the same order regardless of the way the form factors are calculated.

Table 4.3 Single Coherent Scattering Compared to Single Compton Scattering (coh/Comp)

		(coh/Comp)					
	mode	C	Mg	Al	Ti	Fe	Cu
calibration material position 1	PHA-f	3.	3.	4.	>20	>20	>20
	PHA-l	>20	5.	7.	>20	>20	5.
calibration material position 2	SDM-f	2.2	2.	1.8	2.4	1.8	1.8
	SDM-l	1.6	1.8	1.1	1.	1.6	1.3

Table 4.3 shows the ratio of first coherent scattering over first Compton scattering for the Monte Carlo computer model (represented in figure 4.6) taking into account the opening angle correction. As expected the predominant process in this situation is coherent scattering due to the strongly peaked coherent scatter distribution for small angles and due to collimation of detector probes. In all cases, the free atom approximation produces more coherent scattered radiation as a consequence of the

maximum scattering probability at 0° scattering angle. The PHA method shows that virtually all single scattered radiation corresponds to coherent scatter as the pinhole size (1 mm) is smaller and also because not all the photon energies are recorded. For the split detector method the number of single Compton scatter is considerably increased due mainly to the bigger pinhole size.

4.4.3 Determination of A_1 and its Dependence on Examined Material Position

In the following figures (4.10 to 4.13), an 80 kVp incident spectrum was considered along with 15 cm perspex thickness and 1 mm calibration material thickness. In each figure, curve I represents the calculated value of A_1 for primary incident x-rays, curves II and III represent the value of A_1 calculated for large field incident x rays with and without opening angle correction respectively.

i) PHA Method

Figure 4.10 presents the value of A_1 as a function of Z in the Monte Carlo model, where the position of the calibration material is at the top surface (position 1) and the size of the pinhole is 1 mm corresponding to the PHA method. All figures show a decrease in the value of A_1 when the contribution of scattered radiation to the system is incorporated in the dual energy analysis. Furthermore, when the opening angle correction is omitted, the value of A_1 is even smaller. All these results are due to the fact that when the scattered photons are added to the transmitted photons, the total number of photons reaching the detector system is increased, as if there was less attenuation in the calibration material, resulting in a decrease in A_1. The more scattered radiation that reaches the detector system, the lower the value of A_1 becomes.

Figure 4.10 Effect of Scatter. PHA Method. Material at Top surface*

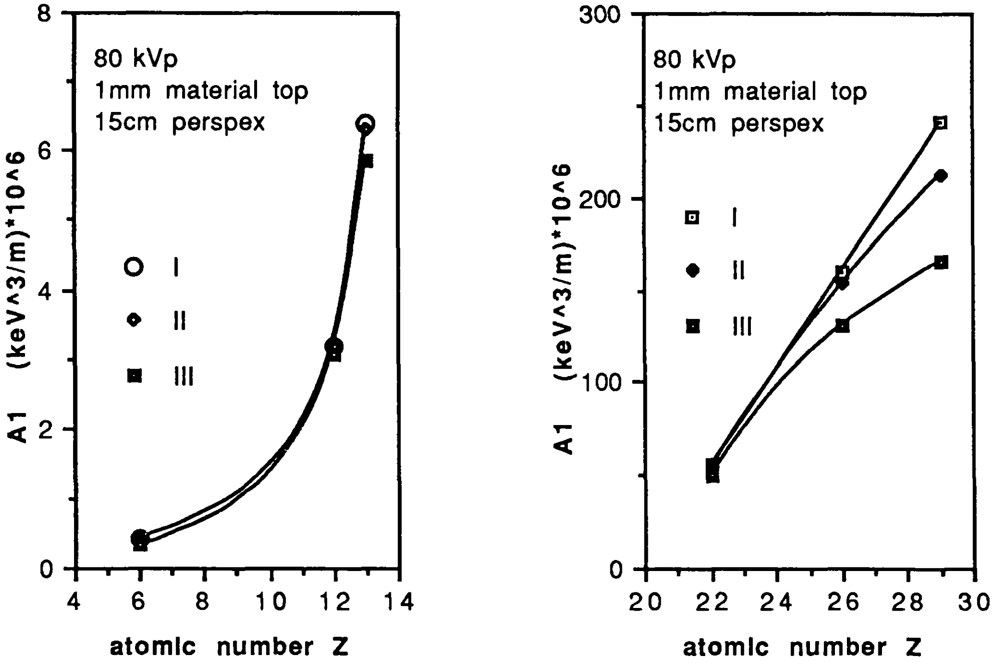

a)Free atom approximation

b)Free atom approximation

c)Liquid water form factor

d)Liquid water form factor

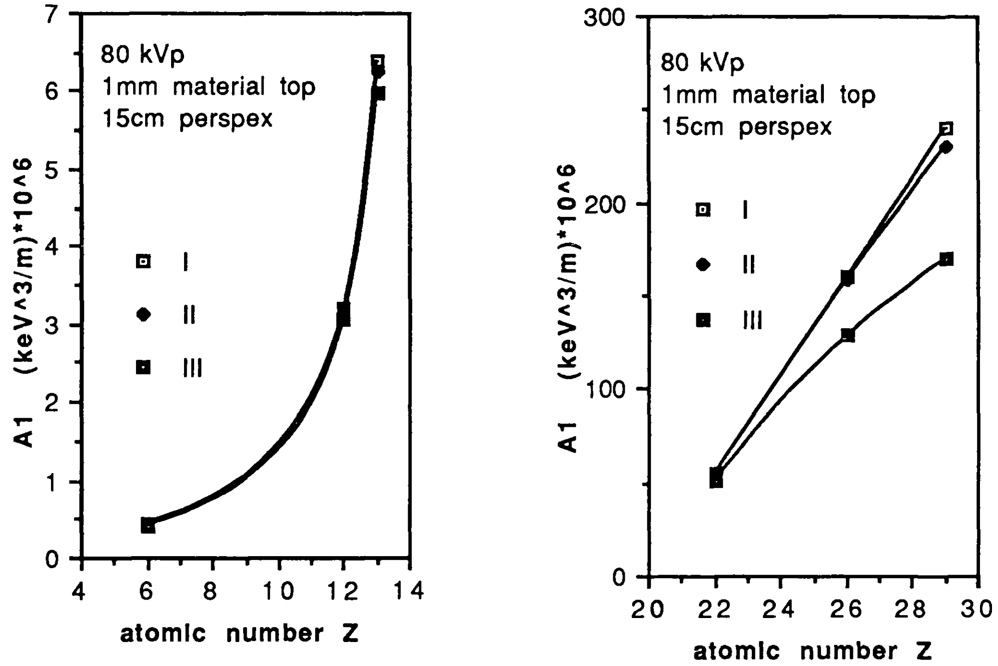

***Note 4.1**: curve I- Primary A_1, i.e. pencil beam incident x-rays.

curve II- Total calculated A_1 using large field incident x-rays with opening angle correction.

curve III- Same as II but with no opening angle correction.

Figure 4.11 Effect of Scatter. PHA Method. Material at Bottom surface.*

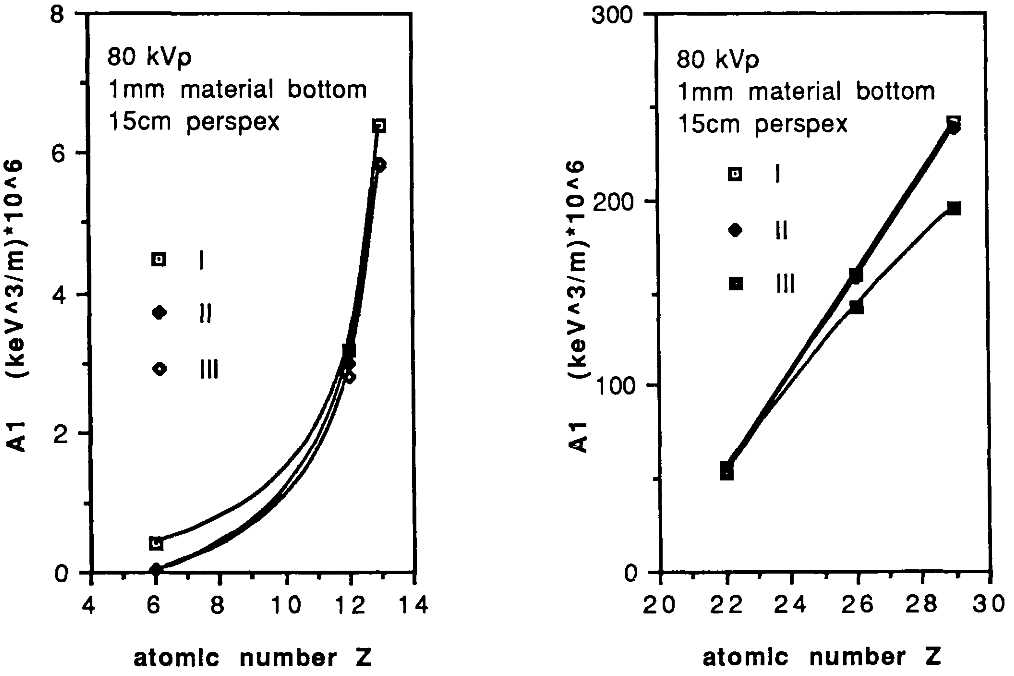

a) Free atom approximation b) Free atom approximation

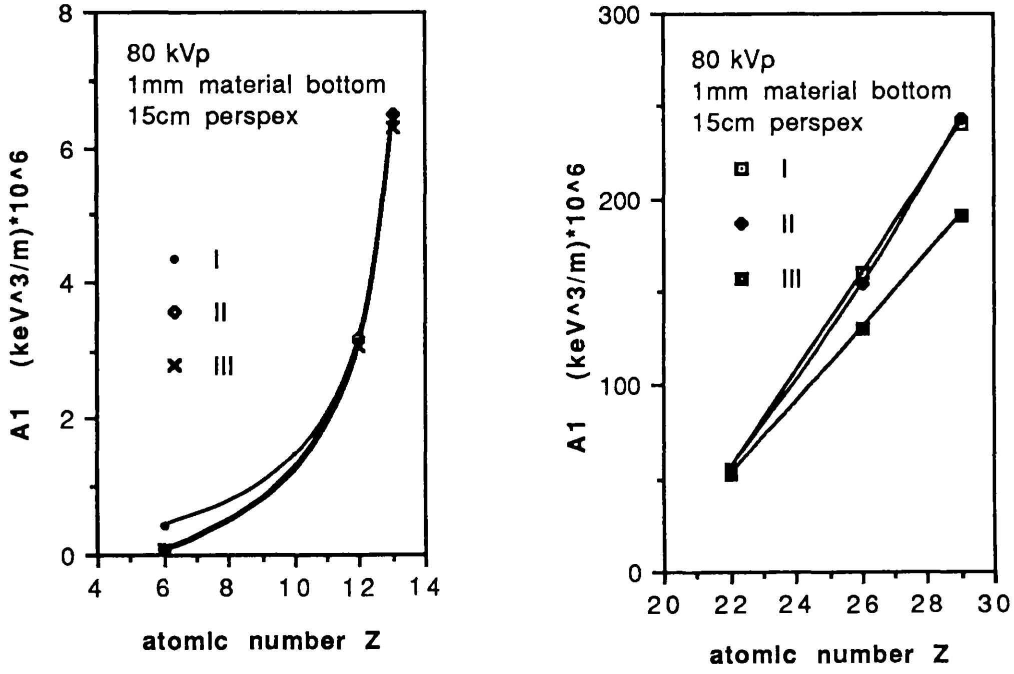

c) Liquid water form factor d) Liquid water form factor

* see note 4.1 for I, II and III.

It is clearly seen (figure 4.10b and figure 4.10d) that there is more scattered radiation reaching the detector system when the atomic form factors are used (free atom approximation), especially for high atomic numbers. This fact can be explained by the coherent scattering angular distribution (figure 4.4) and by the collimation of the detectors. Figure 4.4 shows the maximum coherent peak for the free atom approximation is at 0° angle whereas that of liquid water is at a non-zero scattering angle. Therefore when the free atom approximation is used in the computer model, the small collimator opening angle will collect a larger proportion of forward scattered radiation. As a result, when the opening angle correction is applied, the value A_1 for copper is decreased by 11% (figure 4.10b) compared to only 4% (figure 4.10d) from the "free" scattered radiation case.

For low atomic numbers however, the effect of scattered radiation is very small (figure 4.10a and figure 4.10c). Both the free atom approximation and "liquid water" approximation methods are comparable.

In figure 4.11, the values of A_1 are computed in the same way as that in figures 4.10 except that the calibration material was positioned at the bottom surface of the Monte Carlo model. Both figures (4.11 and 4.10) show similar behaviour, i.e. there is a decrease of A_1 when scattered radiation is included in the analysis, and the free atom approximation results in slightly more scattered radiation. One important factor can be seen however, the scattered radiation generated by this model is less in comparison to that generated when the calibration material is placed at the top surface (apart from C). For example the primary value of A_1 for copper is decreased by 1.1% in figure 4.11b (curve II) compared to 11% in figure 4.10b (curve II). The calibration material placed in position 2 acts like a filter and stops a large proportion of the scattered photons produced by the perspex phantom.This results in a slight variation of A_1 from the "free" scattered radiation case.

ii) Split Detector Probe

For the Monte Carlo computer model with 2 mm pinhole size, the results are presented in figures 4.12 and 4.13, which show the dual energy number A_1 as a function of Z with calibration materials placed in position 1 and position 2 respectively. In this case the model includes the split detector system comprising the two scintillation detectors (CsI, NaI) separated by the copper filter.

Similarly to the previous analysis (PHA method) the value of A_1 shows a decrease when scattered radiation is included, but this time the effect is larger. This occurs because the split detector method records all photon energies and has a larger pinhole, resulting in higher counts of scattered radiation. The value of A_1 calculated with all photons is clearly separated from the value of A_1 calculated without scatter, for all calibration materials.

Both figures 4.12a , 4.12b and figures 4.12c, 4.12d show similar behaviour, i.e. the scattered radiation produced is independent of the way the form factors were calculated. This can be explained by table 4.3 (mode SDM-f and SDM-l) which shows an increase of single Compton scattered radiation masking any effects from form factor calculations.

Similarly to figures 4.11, figures 4.13 show an increase of the total A_1 value when the calibration material is placed at position 2. When the opening angle correction is applied the form factor effect is not significant, except for Mg.

Figure 4.12 Effect of Scatter. Split Detector Method. Material at Top Surface*

a) Free atom approximation b) Free atom approximation

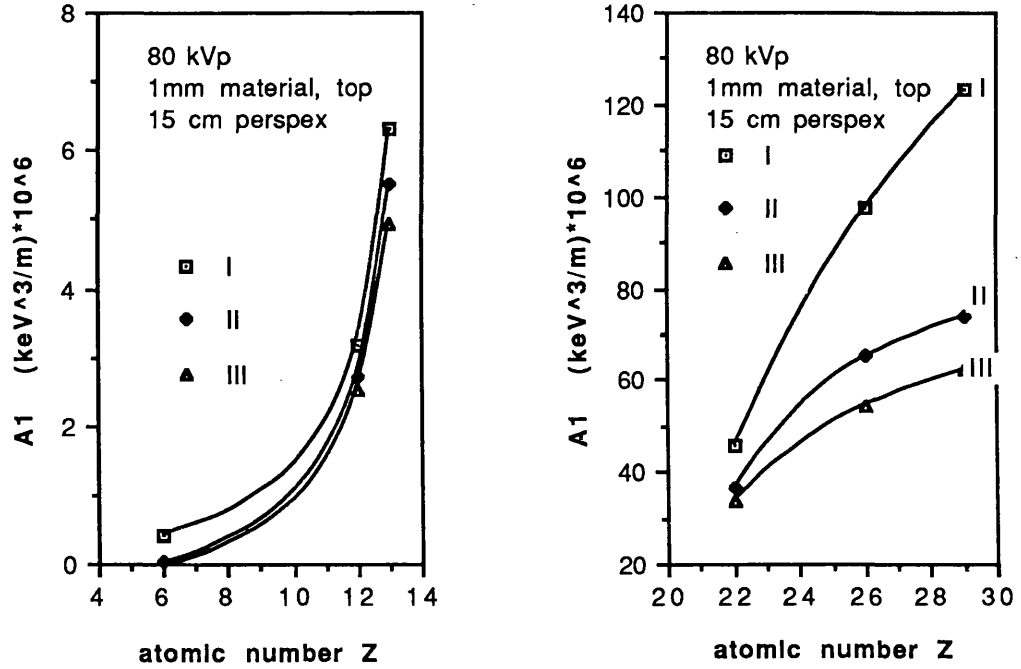

c) Liquid water form factor d) Liquid water form factor

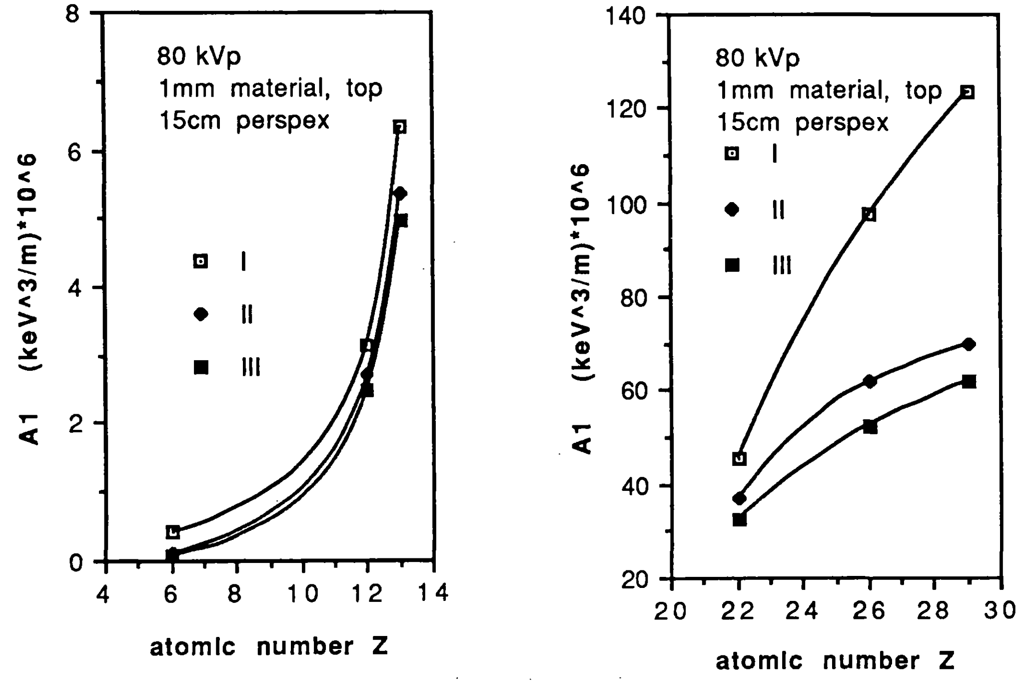

* see note 4.1 for I, II and III.

Figure 4.13 Effect of Scatter. Split detector Method. Material at Bottom Surface*

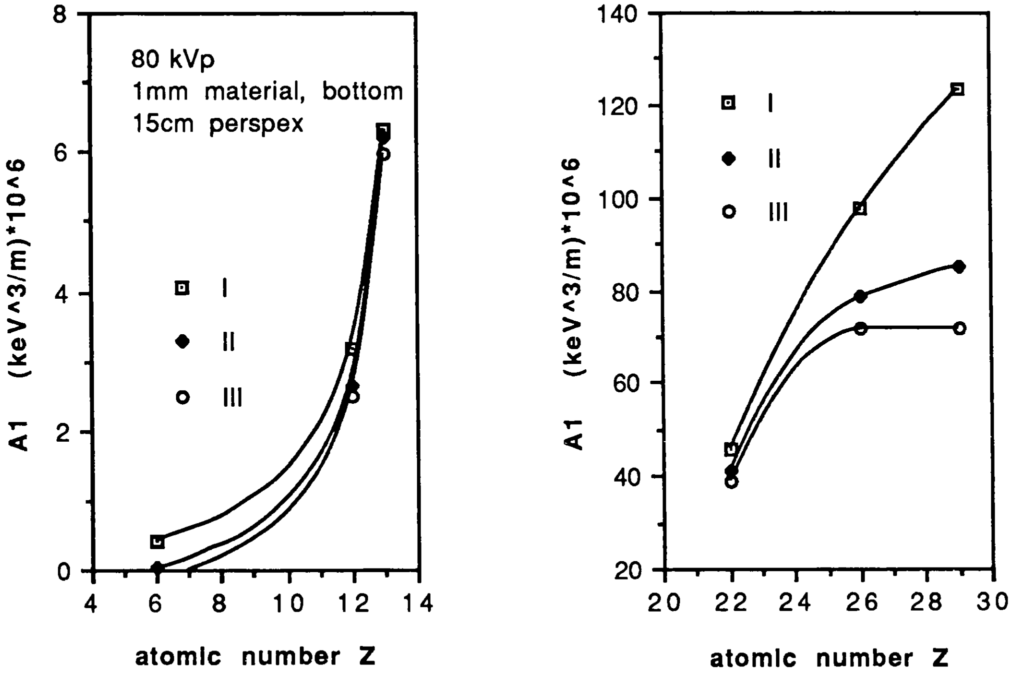
a) Free atom approximation b) Free atom approximation

c) Liquid water form factor d) Liquid water form factor

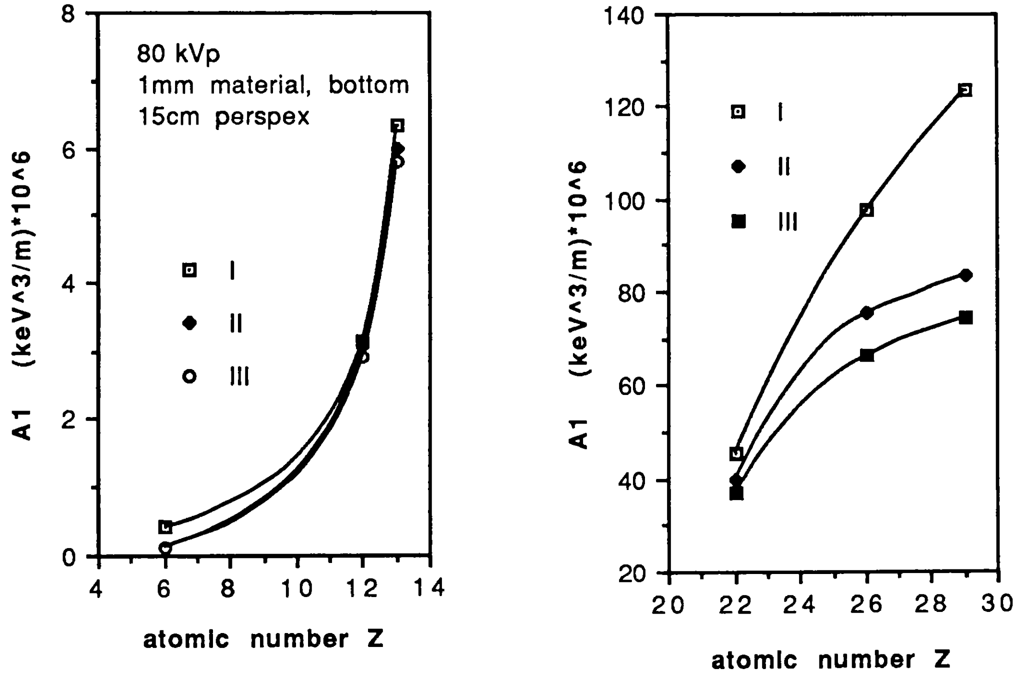

---

* see note 4.1 for I, II and III.

4.4.4 Dependence of Scattered radiation on Incident Spectra

Results of our calculations for a 70 kVp and an 80 kVp large field incident beams are shown in figures 4.14. The Monte Carlo computer model with its calibration material at the top surface of the phantom was adopted. Also the perspex form factors using the free atom approximation were applied due to the non availability of molecular data.

i) PHA Probe

In figures 4.14a and 4.14b, curve I represents the calculated value of A_1 for an 80 kVp incident spectrum on a curve II is for a 70 kVp incident spectrum (in both cases the opening angle correction was applied). The value of A_1 are lower at 70 kVp because a reduction in the energy of the x rays reduces the intensity penetrating the phantom. Consequently, although the Compton scattering probability is lower at 70 kVp producing less scattered radiation (the main process being multiple scatter), the decrease of primary photons reaching the detector system leads to a lower signal to noise ratio, i.e. the total scattered radiation over primary radiation ratio is increased. Therefore, a 70 kVp spectrum appears to produce relatively more scattered radiation when compared to primary photons.

For low atomic number, the PHA method shows that A_1 is independent of the incident spectra considered (figure 4.14a). However as the atomic number increases, the value of A_1 decreases with lower kVp (figure 4.14b) as a result of decreasing transmitted radiation.

ii) Split Detector Probe

The results are similar to the PHA mode; for low atomic numbers the value of A_1 is independent of the incident spectra considered (figure 4.14c). For high atomic

Figure 4.14 Dependence of Scatter on Incident Polyenergetic Beam*

a) PHA method

b) PHA method

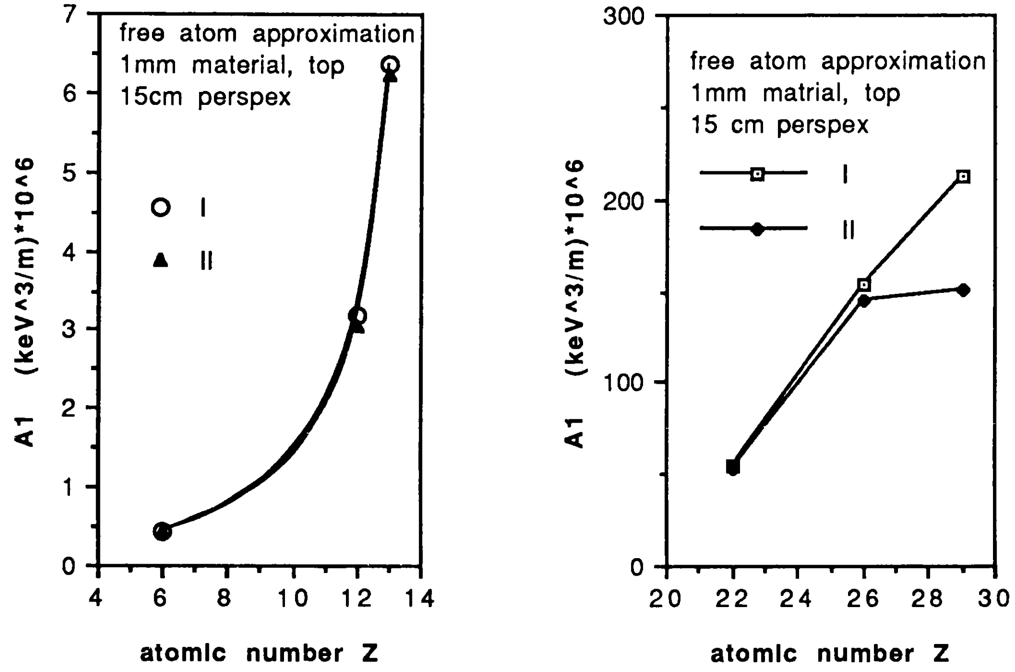

c) Split detector method

d) Split detector method

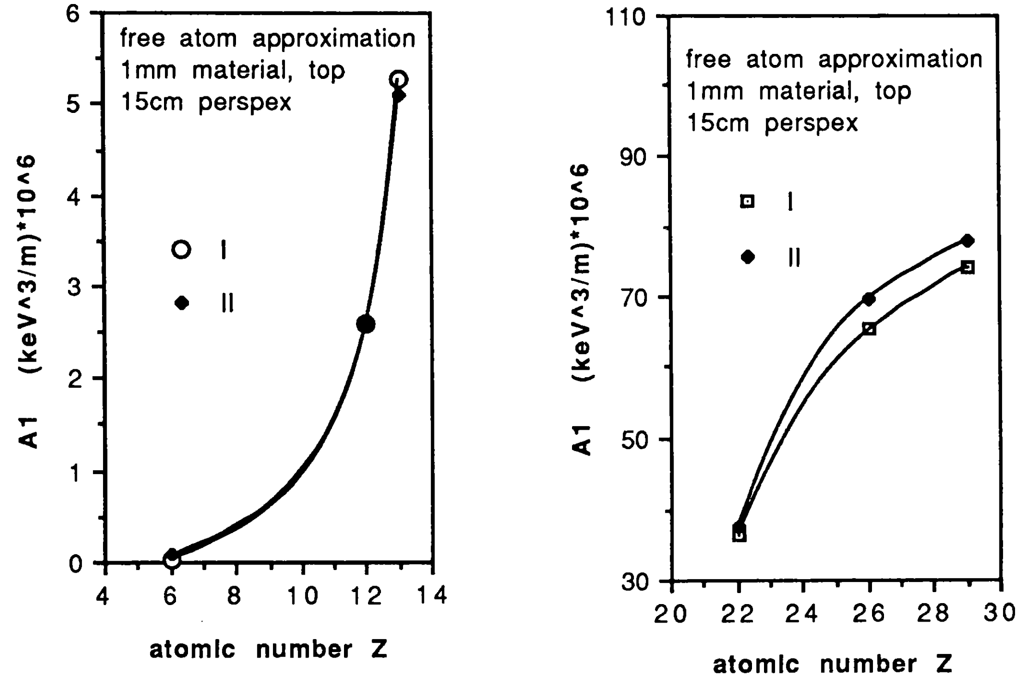

* curve I- Monte Carlo calculation of A_1 at 80 kVp.

curve II- Monte Carlo calculation of A_1 at 70 kVp.

numbers however, the split detector method shows a different response. In this case the values of A_1 at 70 kVp are higher. This fact was already observed experimentally using narrow beam geometry (cf. 3.4.5).

4.4.5 Dependence of Scattered Radiation on Phantom and Examined Material Thickness

The calibration "tissue" was positioned at the top surface of the Monte Carlo model and the perspex atomic form factors were used. In all cases, large field incident beams are considered and the opening angles are corrected.

i) Effect of Phantom Thickness

The dependence on phantom thickness is shown in figures 4.15. In each figure, curve I represents the calculated value of A_1 for 10 cm of perspex. Since the probability that a photon will escape a thicker phantom is smaller, the photon can undergo a large number of scattering events. Hence multiple scatter and total scatter will increase with thicker objects. Table 4.2 showed that for 15 cm of perspex the predominant process in the Monte Carlo computer model was multiple scatter. As scatter is reduced in thinner objects, the value of A_1 for 10 cm of perspex will be higher.

Figure 4.15a (PHA method) shows that the value of A_1 for low atomic numbers is essentially independent of the phantom thickness between 10 and 15 cm. However the effect of phantom thickness variation becomes quite apparent at higher atomic numbers (Fe and Cu in figure 4.15b) due to the decrease of transmitted radiation, while the amount of scattered radiation remains basically the same.

The split detector method shows a stronger dependence on phantom thickness (figures 4.15c and 4.16d). This is due to several reasons. First, the split detector method records all photon energies, and second, the pinhole size is larger, resulting in an

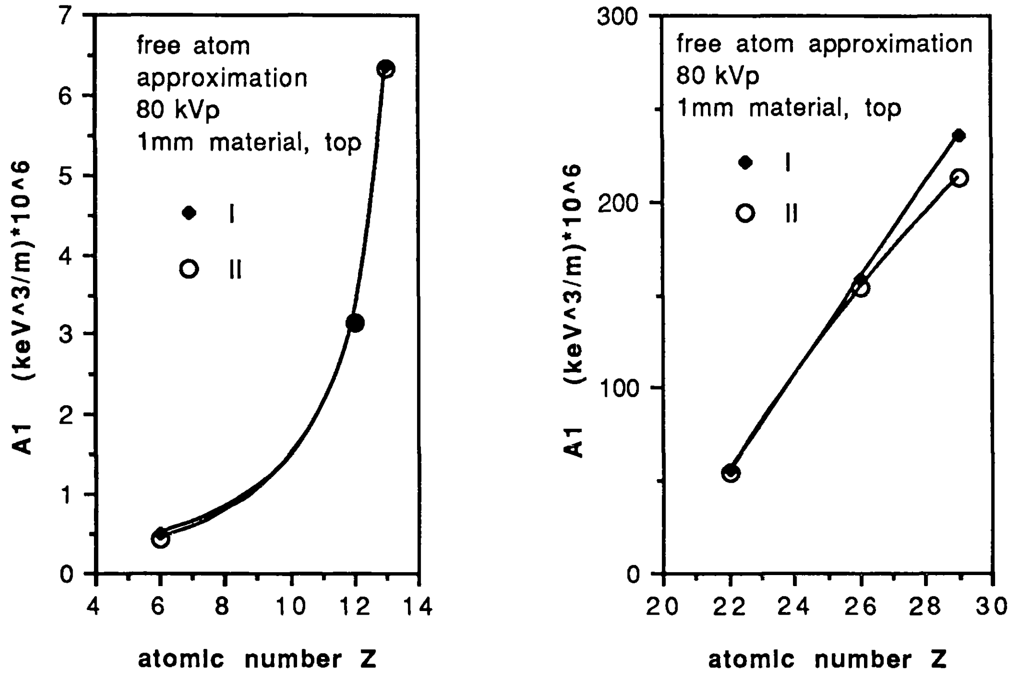

a) PHA method

b) PHA method

c) Split detector method

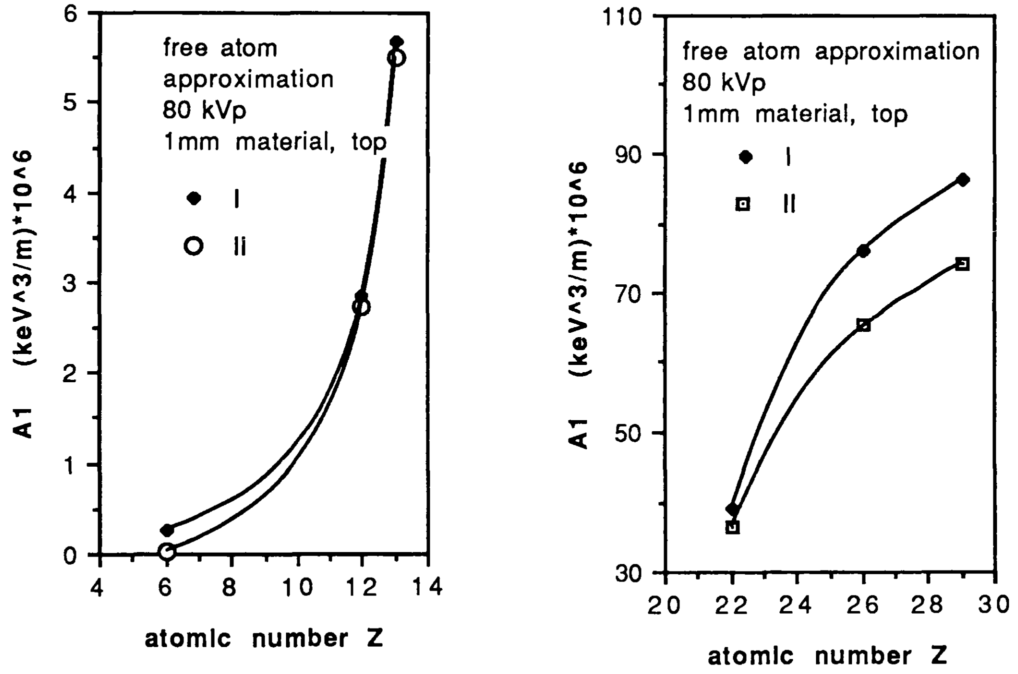

d) Split detector method

* curve I - Monte carlo caluclation of A_1 for 10 cm perspex thickness.

curve II - Monte Carlo calculation of A_1 for 15 cm perspex thickness.

increase of the recorded scattered radiation. Finally, the effect of beam hardening is larger as the two broad beam absorbed spectra detected by the split detector probe are represented by two effective energies.

ii) Effect of Examined Material Thickness

In figures 4.16, the examined material thickness was varied from 1 mm to 2 mm. Both of the calculated values of A_1 for the PHA method and split detector method reduce with increasing material thickness. While the scattered radiation produced by the Monte Carlo model remains essentially the same, the transmitted radiation reaching the detector system is reduced considerably (depending on the atomic number) as the material thickness increases. So at 2 mm material thickness, the Monte Carlo model seems to produce relatively more scattered radiation, resulting in lower values of A_1(these values are even smaller than if just the beam hardening effect was considered).

Figure 4.16a and figure 4.16c show that the value of A_1 is independent of the calibration material thickness in the low atomic number range. However, the effect of calibration material thickness is very apparent in the case of the split detector method for high atomic numbers, even leading to a drop of A_1 in the range Z=26 to Z=29 (figure 4.16d). This occurs because of the beam hardening effect and scattered radiation. The effect of scattered radiation can be observed by comparing the results from a narrow beam geometry situation (4.16d, curves III and IV) with those obtained from a broad beam geometry case (figure 4.16d, curves I and II).

Figure 4.16 Dependence of Scatter on Material Thickness*

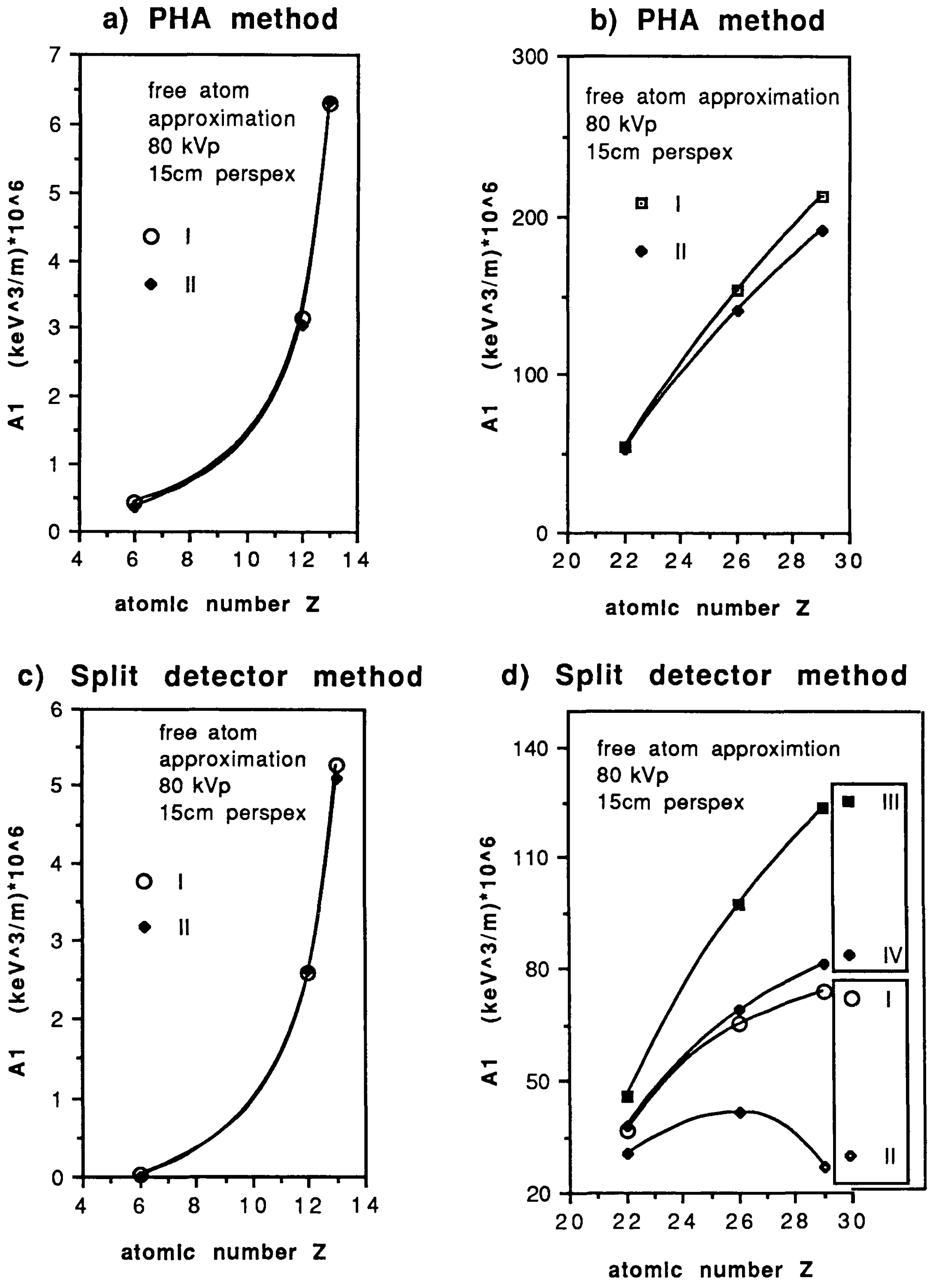

* curve I and II - Monte Carlo calculation of A_1 for 1mm and 2mm material thickness respectively.

curve III and IV - A_1 calculated for 1mm and 2mm material thickness respectively using narrow beam geometry computer model.

4.4.6 Conclusions from the Monte Carlo Simulation

The Monte Carlo simulation was carried out to investigate the capabilities of a detector system used in a dual energy mode, and because of its ability to follow individual photon histories, it can be used to study the effects that scattered radiation have on the recorded signal A_1. The conclusions are :

i) The Monte Carlo computer model has shown that the predominant process is multiple scattering.

ii) - PHA method : for low atomic numbers the effect of scattered radiation is small. For high atomic numbers, A_1 depends on the way the form factors are calculated. The free atom approximation produces more detected scatter leading to lower values of A_1.

- Split detector method : the larger proportion of scattered radiation produces a lower A_1 value even at low Z. However, the scatter signal produced was independent of the way the form factors were evaluated.

iii) The scattered radiation contribution to the system depends on the position of the calibration material within the model.

iv) For low atomic numbers both PHA and split detector methods are almost independent of the incident polyenergetic beam. As Z increases then

- PHA method : A_1 decreases with decreasing kVps (80 to 70 kVp)
- Split detector method : A_1 increases with decreasing kVps.

v) The PHA method is independent of phantom thickness for the low Z range whereas the split detector method shows a stronger dependence in the 6-29 atomic number range.

vi) The effect of calibration thickness on A_1 is almost absent for both the PHA and split detector methods for low atomic numbers. However, as Z increases the split detector method shows a stronger dependence of A_1 on material thickness resulting in a drop of A_1 between the Fe and Cu calibration materials.

4.5 Measurements of A_1 in Presence of Scattered Radiation

4.5.1 Experimental Procedure

The measurements of the dual energy coefficient A_1 in chapter 3 were conducted under narrow beam conditions. In the current situation large fields of incident x rays are considered. To compare the Monte Carlo calculated values of A_1 in the presence of scattered radiation with experimental values, the latter were determined using the experimental configuration shown in figure 4.17. The incident square field was 13 cm^2. A perspex block 15 cm square was positioned with its surface 50 cm from the focal spot of the Siemens Ergophos 4 operated in fluorescence mode. Calibration materials (Z=6 to 29) with 1 mm thickness were positioned alternatively at top and bottom of phantom. Both detector systems, the CsI/Cu/NaI and the HPGe detectors, were located in turn beneath the phantom. The air gap between the phantom exit and the detector system was 2 cm.

The experimental configuration was based upon the Monte Carlo computer model represented in figure 4.5.

One stepping motor together with a suitable driver and interface circuit was included into the measurement system. The stepping motor was used to move the perspex block with its calibration materials in a horizontal translation. The sequence of measurements followed those required by the theoretical considerations of equation 1.42 (cf. section 1.5) and experimental evaluation from the split detector probe and the PHA probe described in chapter 3. The required signals $D_m(E)$ and $D_w(E)$ were obtained from three measurements in a single uninterrupted exposure.

Figure 4.17 Experimental Set-Up in Presence of Scatter*

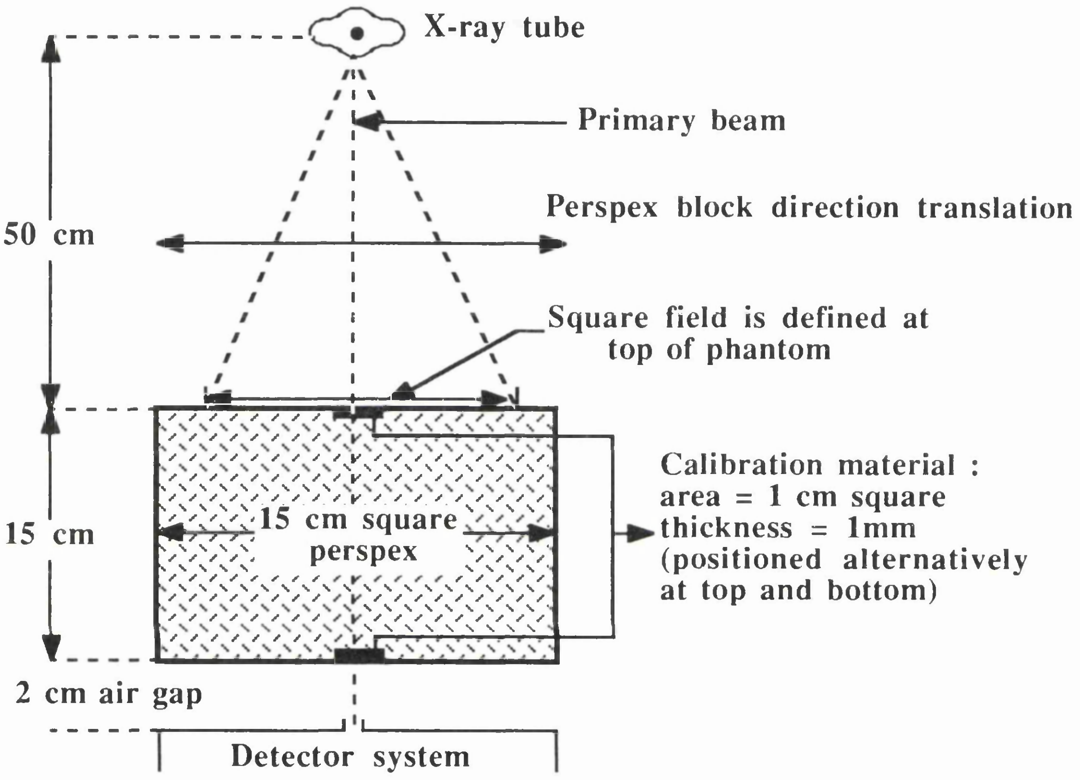

* Support of perspex block not shown

$D_W(E)$, the signal arising without the presence of calibration material was found by taking two measurements, before and after measuring the Dm(E) signal through the calibration material, and by shifting the perspex block horizontally by 2 cm each time. This is illustrated in figure 4.18.

Figure 4.18 Sequence of Measurement with Large Incident X-ray Field

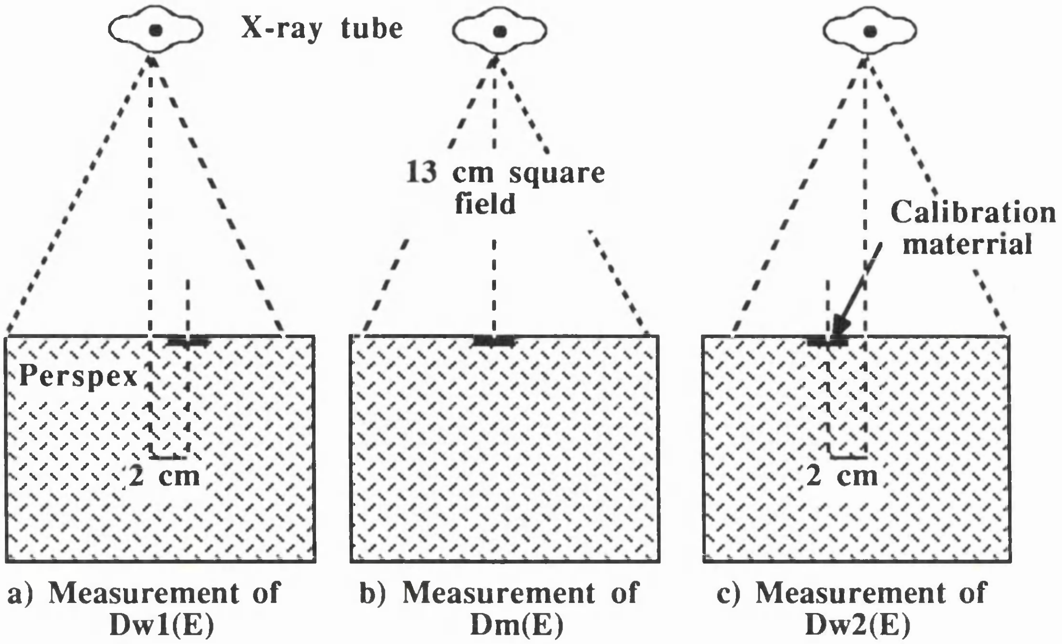

The background measurement $D_w(E)$ corresponds to $(D_{w1}(E) + D_{w2}(E))/2$. This process was carried out for recalibration of x-ray tube output intensity with time. The experimental values of A_1 for each calibration material was evaluated for both the PHA method and split detector method. Each set of measurements was repeated several times to account for fluctuations in x-ray tube output.

4.5.2 Results

In all the experiments, each measurement of A_1 has been repeated at least five times. The errors were calculated using the standard deviation of these repeated measurements.

i) Position of Examined Material

The experimental results at 80 kVp and for two positions of the calibration material are compared with the Monte Carlo results in figure 4.22. In each figure, the experimental or the calculated values of A_1 are represented by curve I for the case where the calibration materials are at the bottom of the perspex phantom, and by curve II for the second case.

The general behaviour of the curves in figure 4.19a is similar to that of the corresponding curves for the Monte Carlo model (figure 4.19b). Both the experimentally determined values of A_1 and the calculated values are higher for materials positioned at the bottom of the phantom. However, the PHA method shows some discrepancies between the experimental and Monte Carlo calculations for high atomic numbers (Fe and Cu). The reasons for this are given in section 4.5.3.

The split detector method (figures 4.19c and 4.19d) shows good agreement between experimental and Monte Carlo results within the experimental error.

ii) Dependence on Incident Spectra

The dependence on incident spectrum is shown in figures 4.20 both experimentally and by Monte Carlo calculations. Figures 4.20a and 4.20b show that although the experimental values are lower for high atomic numbers, the general pattern of both figures is similar , i.e. the value of A_1 decreases with decreasing kVp.

For the split detector method, figure 4.20c shows that not only do the experimental values of A_1 agree with the Monte Carlo results (figure 4.20d) within the experimental error, but also emphasise the fact that A_1 decreases with increasing kVp for high atomic numbers. At low atomic numbers it is difficult to distinguish between A_1 at 70 and 80 kVp because of the relatively large error bars.

Figure 4.19 Comparison of Experimental and Monte Carlo Results when Material Position is Changed*

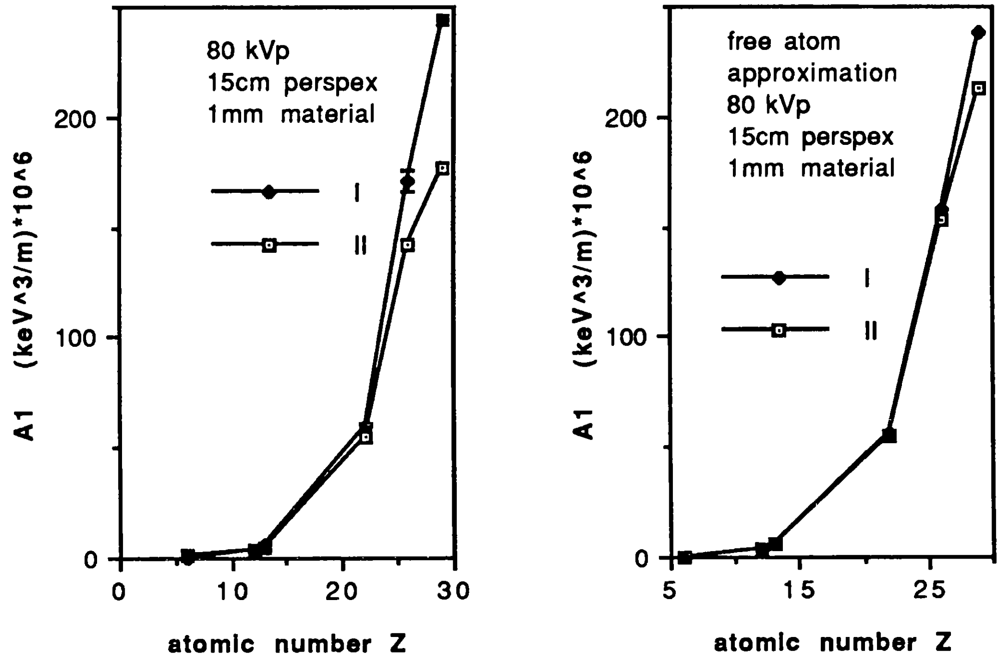

a) PHA method. Experimental results

b) PHA method. Monte Carlo results.

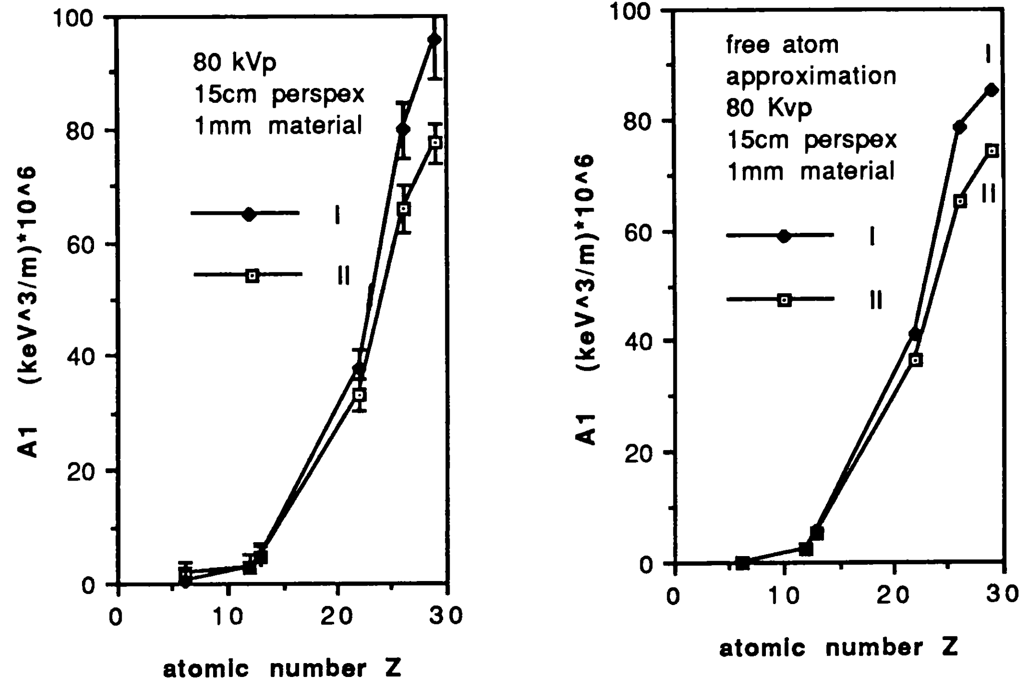

c) Split detector method. Experimental results.

d) Split detector method. Monte Carlo Results.

* curve I -calculated or experimental value of A_1 with material positioned at bottom surface of phantom.

curve II -calculated or experimental value of A_1 with material positioned at top surface of phantom.

Figure 4.20 Comparison of Experimental and Monte Carlo Results for Various Incident Spectra*

a) PHA method. Experimental results.

b) PHA method. Monte Carlo results.

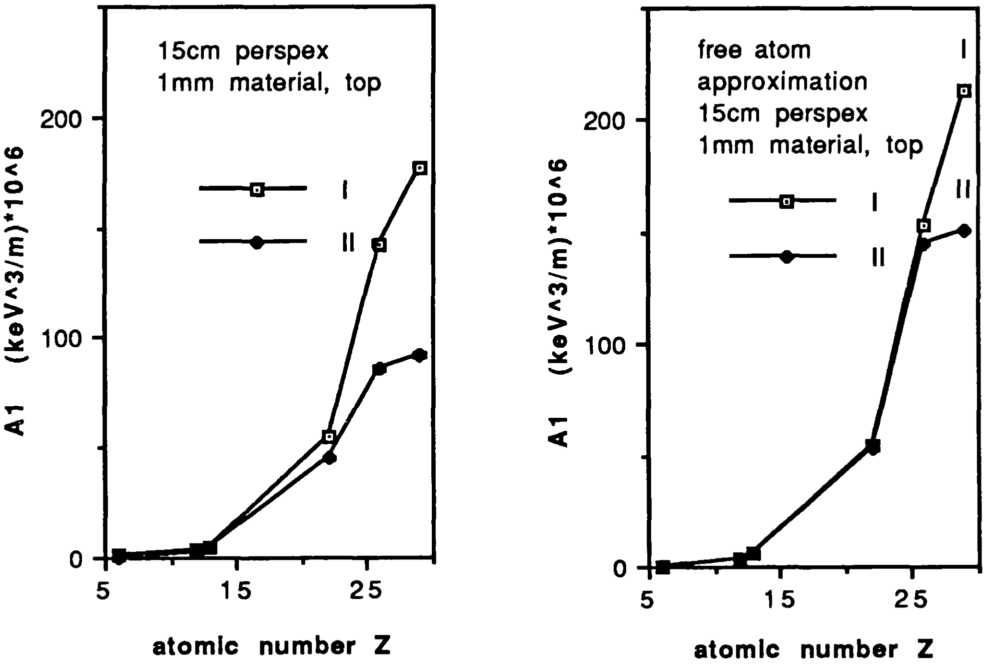

c) Split detector method. Experimental results

d) Split detector method. Monte Carlo results.

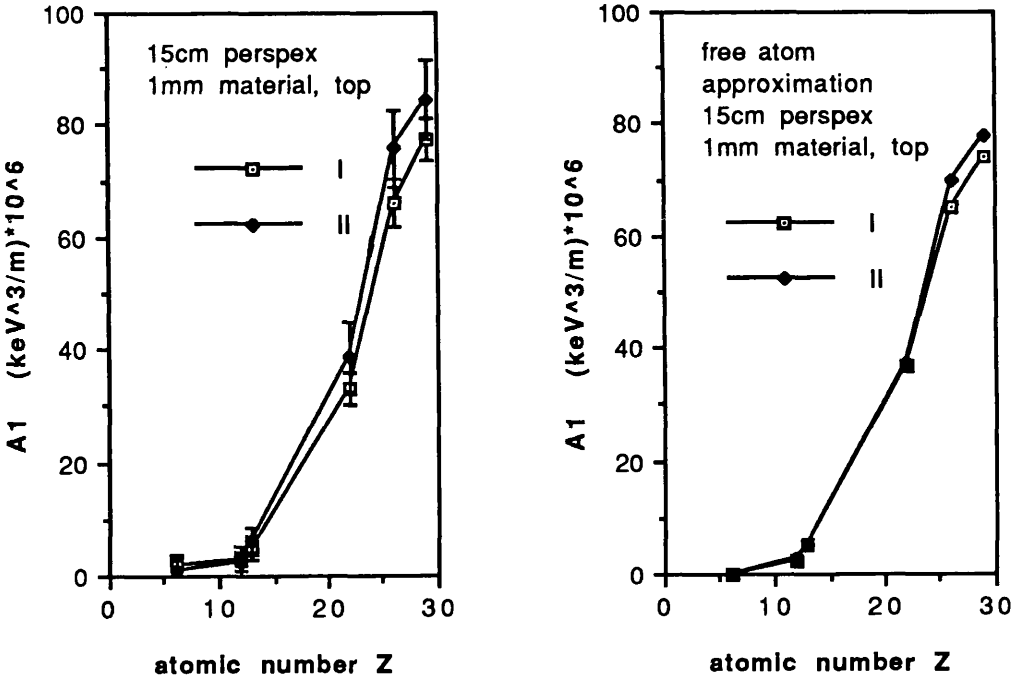

* curve I - calculated or experimental value of A_1 at 80 kVp.

curve II - calculated or experimental value of A_1 at 70 kVp.

The error bars associated with the split detector method are higher than those from the PHA method for several reasons. First, due to the large pinhole size more scattered radiation is recorded and hence the noise in the system is increased. Second, the poor resolution of the split detector probe leads to variation of the effective energies and hence of A_1. Finally, the assumption that two effective energies can represent two broad spectra, which is in contrast to the PHA method where only a narrow band of energies are used.

4.5.3 Conclusion

The results obtained from Monte Carlo calculations contain statistical uncertainties caused by the probabilistic nature of the method. In this study, all values of A_1 were calculated for approximately 16 million incident photons represented either by 80 kVp or 70 kVp spectrum. The energy distribution of these spectra being provided by Birch *et al* (1979). Only a small portion (about 100 000) has a direct contribution to the formation of transmitted photons due to the collimation of the detectors. For discussion, the statistical uncertainty is estimated as the standard deviation (SD) of the primary recorded photons (assuming Poisson statistics).

The uncertainty depends on the incident spectrum, the type and thickness of calibration material, the phantom thickness, and the mode of dual energy analysis. Typically, for the PHA method, the SD ranged from 1% to about 8% (worst case : 80 kVp, 2 mm Cu and 15 cm perspex). For the split detector, the SD varied from about 0.8% to 4%. The latter presents lower statistical uncertainty because all photon energies are recorded, resulting in a higher number of transmitted photons. Furthermore, even if scattered radiation is taken into account, the statistical uncertainty will decrease in favour of the split detector method.

This analysis of the errors involved in the Monte Carlo model shows that the PHA method has lower precision for the calculated A_1s. This partly explains the discrepancies observed between the experimental results and Monte Carlo calculations for the PHA method especially at high atomic numbers where the SD is considerably increased.

Other factors can contribute to these discrepancies and in general to the difference between experimental and Monte Carlo results. These are:

i) In our calculation parallel beam geometry for the incident radiation was assumed. It has been shown that results obtained for a parallel beam geometry are good approximations to results obtained from a diverging beam geometry, provided that the intensity of the primary radiation and the irradiated area at the depth of interest are kept the same in both cases (Johns *et al* 1958). Chan and Doi (1983) have found close agreement between the two cases for a source to detector distance (SDD) of 100 cm. Further study will be needed so that differences in scattered radiation between a parallel beam and a diverging beam with a short SDD can be quantified (in our case the SDD was equal to 50 cm).

ii) The Monte Carlo results may contain, not only statistical uncertainties, but also systematic errors caused by uncertainties in the input data (incident spectrum, attenuation, form factors) and by uncertainties in the physical models of photon interactions such as the lack of characteristic x-ray histories.

iii) Once the incident photons had reached the detector system, narrow beam geometry was assumed. The effect of the energy resolution of the detector systems was not accounted for in the Monte Carlo model.

The purpose of the Monte Carlo model was to assess the behaviour of A_1 in the presence of scattered radiation in all different kind of situations. In general terms, the Monte Carlo simulation gave acceptable results for the split detector method. An increase in the number of incident photons for the PHA case at high atomic numbers would improve the statistical uncertainties and by that means reduce the difference between Monte Carlo and experimental results.

CHAPTER 5 APPLICATION *IN VITRO* OF DUAL ENERGY ANALYSIS

After the development of the dual energy probes, an investigation of the sensitivity of these detectors to excised clinical materials was carried out. To that effect, gallstones were selected in order to determine whether the dual energy probes can differentiate between different types of gallstones. This information is useful in the treatment of gallstone disease as it would help to determine the choice of the treatment course (chemical therapy, surgery or lithotripsy) during a clinical procedure.

5.1 Gallstone Analysis *In Vitro*

Some excised gallstones provided by St Thomas' Hospital London were subjected to dual energy analysis. Stones from different patients were analysed according to the experimental set up shown in figure 5.2. The set up was aimed to simulate the real clinical situation where not only is a large incident polyenergetic beam used but also the gallstones are situated inside the body. Figure 5.1 shows a section through the abdomen where the gallstones are likely to be present (Romanes 1981). At the right hand side of this section where the gallbladder is situated a more uniform structure than the left hand side is observed due mainly to the large liver. Thus, using a uniform phantom is a good approximation to the real clinical situation.

The same x-ray tube, perspex block and detector system as shown in figure 4.20 were used. The centre piece of the perspex block is removable such that gallstones with different thicknesses can be inserted inside the phantom (figure 5.3). Two positions were selected situated at 4 cm and 11 cm from the top surface of the perspex block to mimic the clinical situation as observed in figure 5.1. In this way both the ventricular or

Figure 5.1 Section Through the Abdomen Region*

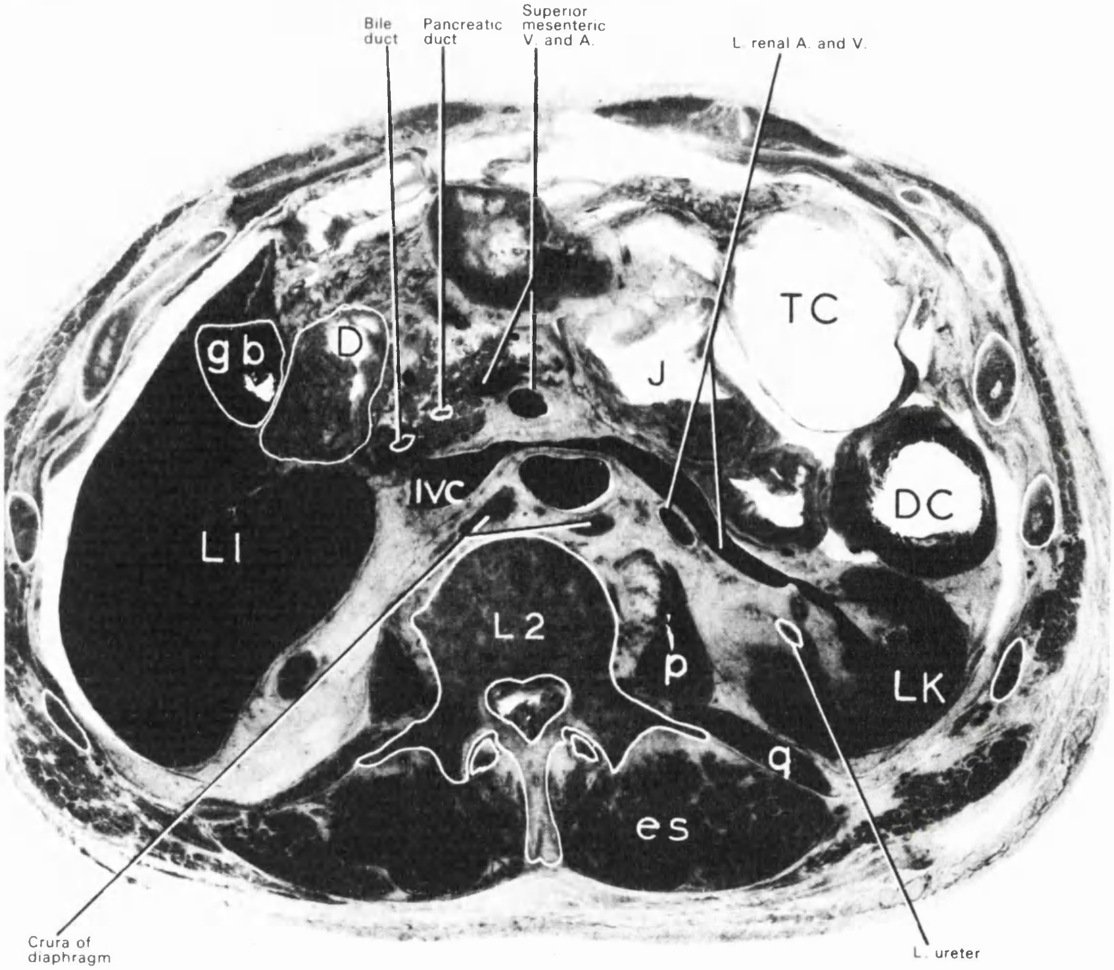

*gb, gallbladder; Li, liver; D, duodenum; TC and DC transverse and descending colon; LK, left kidney.

Figure 5.2 Gallstone Analysis *In Vitro* Experiment

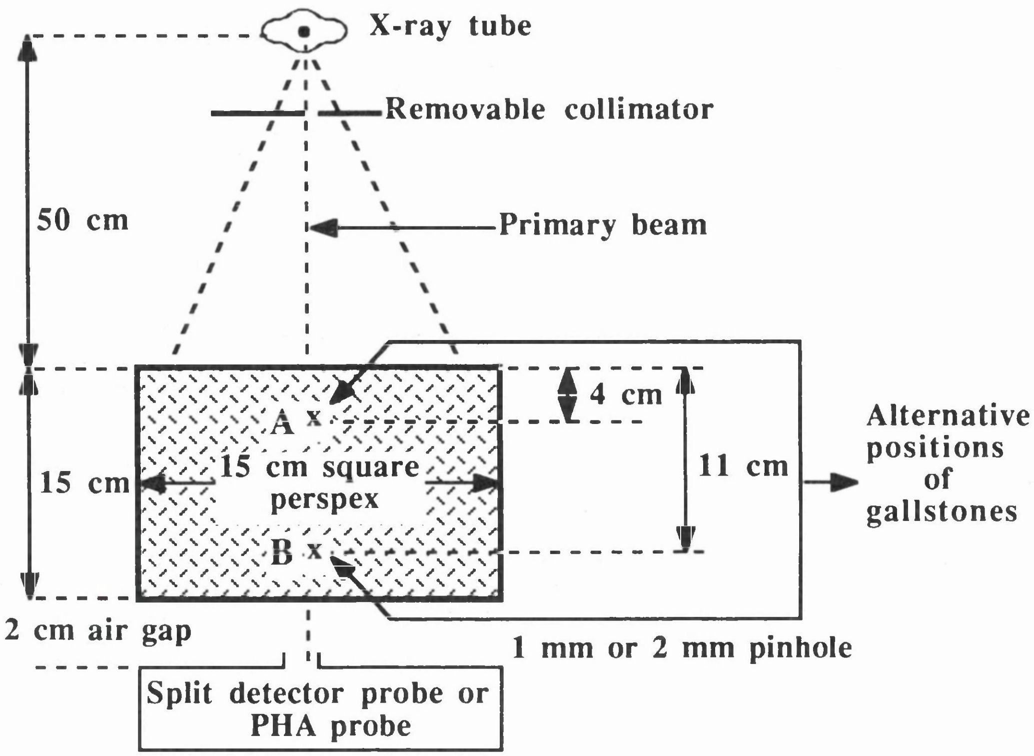

dorsal position of the patient are considered and also the effect of gallstone positioning is investigated. A pencil beam of primary radiation was also produced by collimating the output of the Siemens Ergophos 4 with 1 cm Pb pinhole 5 mm thick (figure 5.2).

The experiments were treated in the same manner as described in chapter 3 and section 4.5.1. The dual energy coefficient A_1 was derived from experiments with and without collimated incident beam.

Figure 5.3 Perspex Block

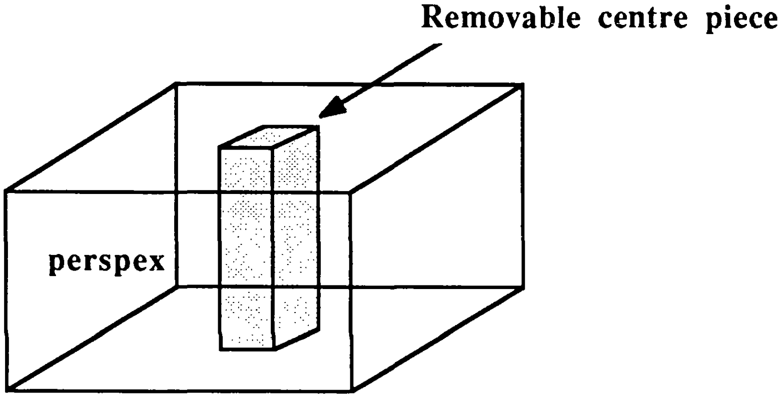

Centre piece

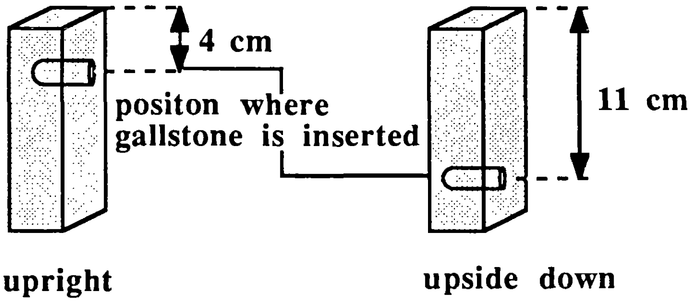

In figure 5.4, the dual energy number A_1 is measured for five gallstones obtained from different patients. Each gallstone was analysed under four separate conditions. The values of point I (figure 5.4) correspond to the measurement of primary A_1, i.e., when the collimator was placed to produce a pencil beam of primary radiation. The values of point II are the measured values of primary A_1 corrected for beam hardening using the iterative procedure (cf section 3.4.4). The values of point III and IV correspond to the measurement of A_1 with a 13 cm square field incident radiation and with the gallstones positioned at A and B respectively (figure 5.2). The error in the measurement of A_1 was evaluated as the standard deviation of ten repeated measurements.

In figure 5.4a, a 70 kVp incident polyenergetic beam was selected because, it provides the best probability of success for the determination of A_1 when using the HPGe PHA probe, as described in section 3.4.6. Gallstones g_1, g_2 and g_3 (figure 5.4) show approximately similar values of A_1 within the limits of the experimental error. Furthermore, the errors in measurements introduced by the effect of scattered radiation are low in comparison to the experimental errors. It is clearly seen that gallstones g_4 and g_5, belong to another type of gallstone classification with higher atomic numbers. Although the effect of beam hardening is well within the experimental error in this case, the values of A_1 are slightly lower when measured with a large field incident beam. Thus, a correction for scattered radiation might prove advantageous for the type of gallstones such as g_4 and g_5. In the event of scattered radiation being present however, the experimental values of A_1 are independent of the position of gallstones within the limits of the experimental error.

For the split detector probe (figure 5.4b), the x-ray tube operating voltage was set at 80 kVp. This was chosen as a compromise between the largest sensitivity of the method obtained at 70 kVp, and the largest probability of success to distinguish between materials of different atomic number obtained at 90 kVp (cf. section 3.4.6). As in the PHA mode results, g_1, g_2, g_3 and g_4, g_5 fall into two separate groups, showing two different types of gallstones. This time however, the experimental errors are much higher. Figure 5.4b shows that both the errors due to the beam hardening effect (values of point II) and the errors due to the inclusion of scattered radiation (values of point III and IV) have no apparent effect when compared to the experimental errors.

Figure 5.4 Gallstone Analysis*

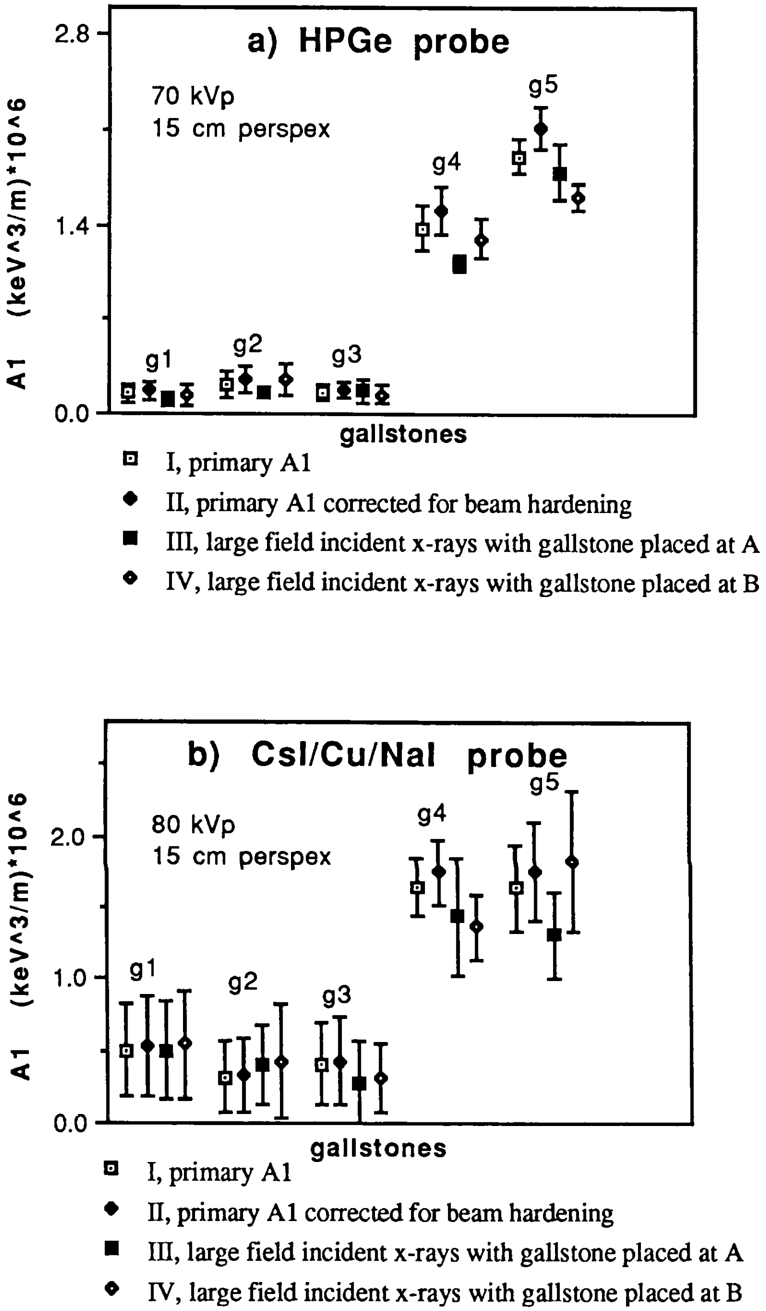

* g_1, g_2, g_3, g_4 and g_5 are gallstones from different patients with 5.8 mm, 4.5 mm, 7.0 mm, 5.5 mm and 5.8 mm thickness respectively.

In chapter 2, 3 and 4, all calculations and measurements were made on well known calibration materials. In chapter 5 the gallstones excised were of unknown compositions. As a verification of the dual energy analysis, the results are compared with those from x-ray diffraction analysis.

5.2 X-ray Diffraction Analysis

The x-ray diffraction technique has a definite advantage over chemical analysis. Chemical methods can determine the presence of elements but cannot always identify a compound. Crystallographic methods provide a rapid mode of identification of crystalline samples of pure compounds or the components of a mixture as long as a minimum quantity ($\sim$ 2% in weight of the total) is present (Sutor and Wooley 1969).

The crystallised compounds under investigation are formed of lattice planes. In x-ray diffraction the electronic density in each lattice plane will produce a certain diffraction pattern. Even if two different compounds have the same lattice, they will have different diffraction patterns because of the electronic density in each lattice. The lattices are not necessarily parallel, they can have all different orientations. When the diffraction patterns are being recorded the angle of the incident radiation is varied so that all kinds of lattices are sampled. The intensity of the diffraction pattern is related to the d spacing, i.e., the distance between two lattices. The recorded photons which form the diffraction patterns are coherent photons but occasionally some inelastic photons will be present. A monochromator is used, set at a specific wavelength which corresponds to the incident radiation wavelength so that only coherent photons are recorded.

The x-ray powder diffraction analysis of gallstones was undertaken at the Department of Crystallography, Birkbeck College. Four gallstones g_1, g_2, g_3 and g_5 were selected. Each one of them was carefully ground to a powder and placed on a rotating sample stage. The powder was assumed to adopt a perfectly random orientation (the powder in effect contains a mass of lattices all jumbled together in different orientations). For the diffraction work a Siemens K710 generator was used, producing 40 kV/30 mA, with a Cu target providing K_α radiation of wavelength 1.542 Å. The resulting diffraction patterns were recorded by a mobile NaI scintillation detector, counting for 2 min at each 0.5 ° interval. The 2θ angular range was 60° where θ is the Bragg diffraction angle. For each gallstone sample the number of coherently scattered photons per second were plotted against the Bragg diffraction angle. These are given in figures 5.5, 5.6, 5.7 and 5.8 for g_1, g_2, g_3 and g_5 respectively. For each compound a pattern of lines was produced. This pattern is characteristic of a particular crystalline substance and usually the first three or four lines are sufficient for identification purposes because the coherent scatter is predominant at low angles (Suttor and Wooley 1969). The diffraction patterns resulting from each gallstone were then matched by computer against the standard patterns of constituents that have been identified in gallstones (cf. table 1.5). The main constituent found in each of these gallstones was cholesterol. Crystallised cholesterol occurs in different shapes and orientations and so produces different diffraction patterns, as can be seen in figures 5.5 to 5.8. Three types of cholesterol were identified, namely Cholesterol Mono, Cholesterol Mono B&L and Cholesterol. The constituent calcium vaterite was found only in g_5, thus identifying the gallstone as a pigment stone. The results are summarised in table 5.1.

Table 5.1 X-ray Diffraction Analysis Results

Constituents of gallstones			
g_1	g_2	g_3	g_5
Cholesterol Mono	Cholesterol Mono	Cholesterol Mono	Cholesterol
Cholesterol Mono B&L	Cholesterol	Cholesterol Mono B&L	Calcium vaterite

It can be clearly seen from table 5.1 that g_1, g_2 and g_3 are cholesterol stones and g_5 is a pigment stone.

Figure 5.5 Gallstone g_1

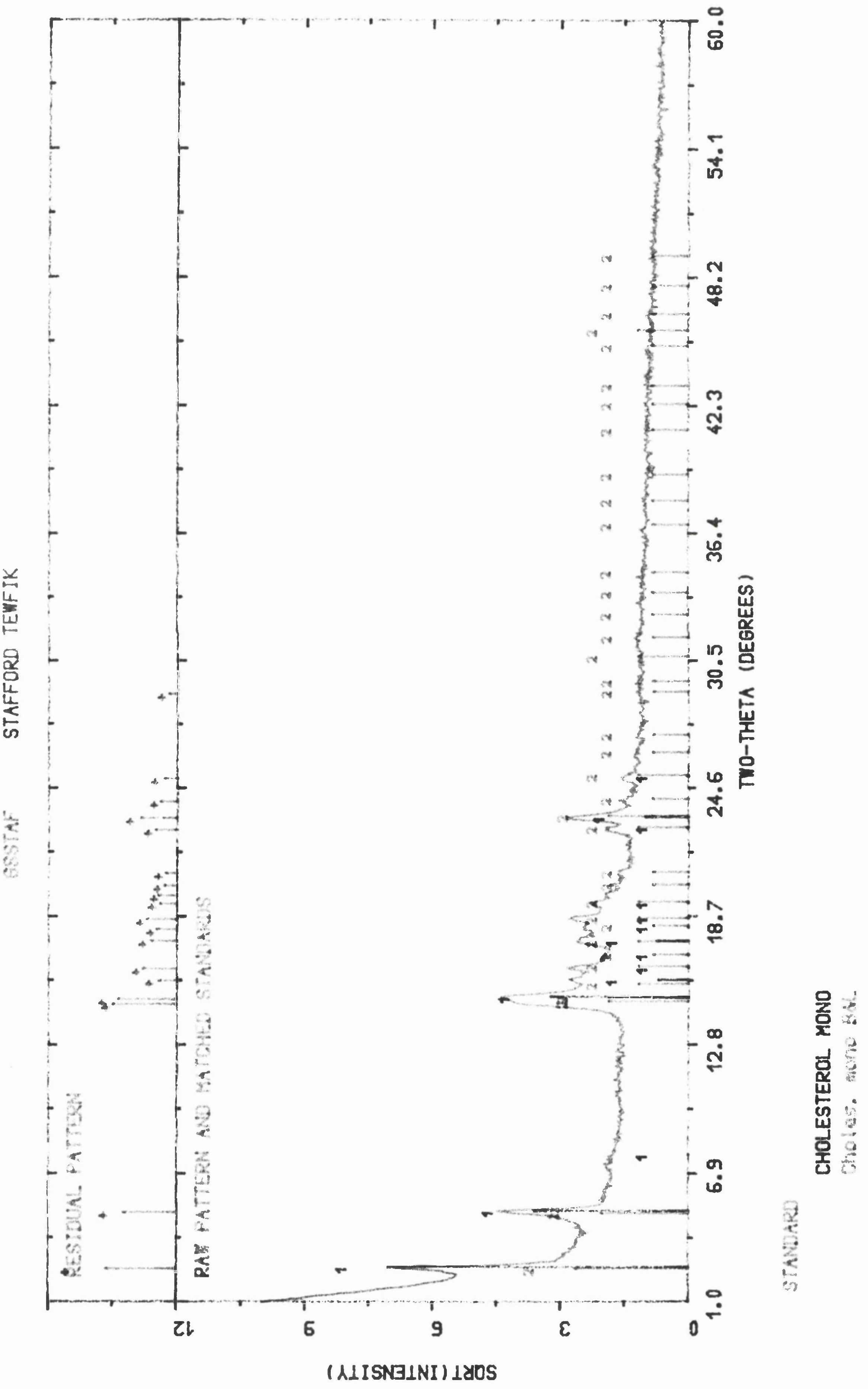

Figure 5.6 Gallstone g2

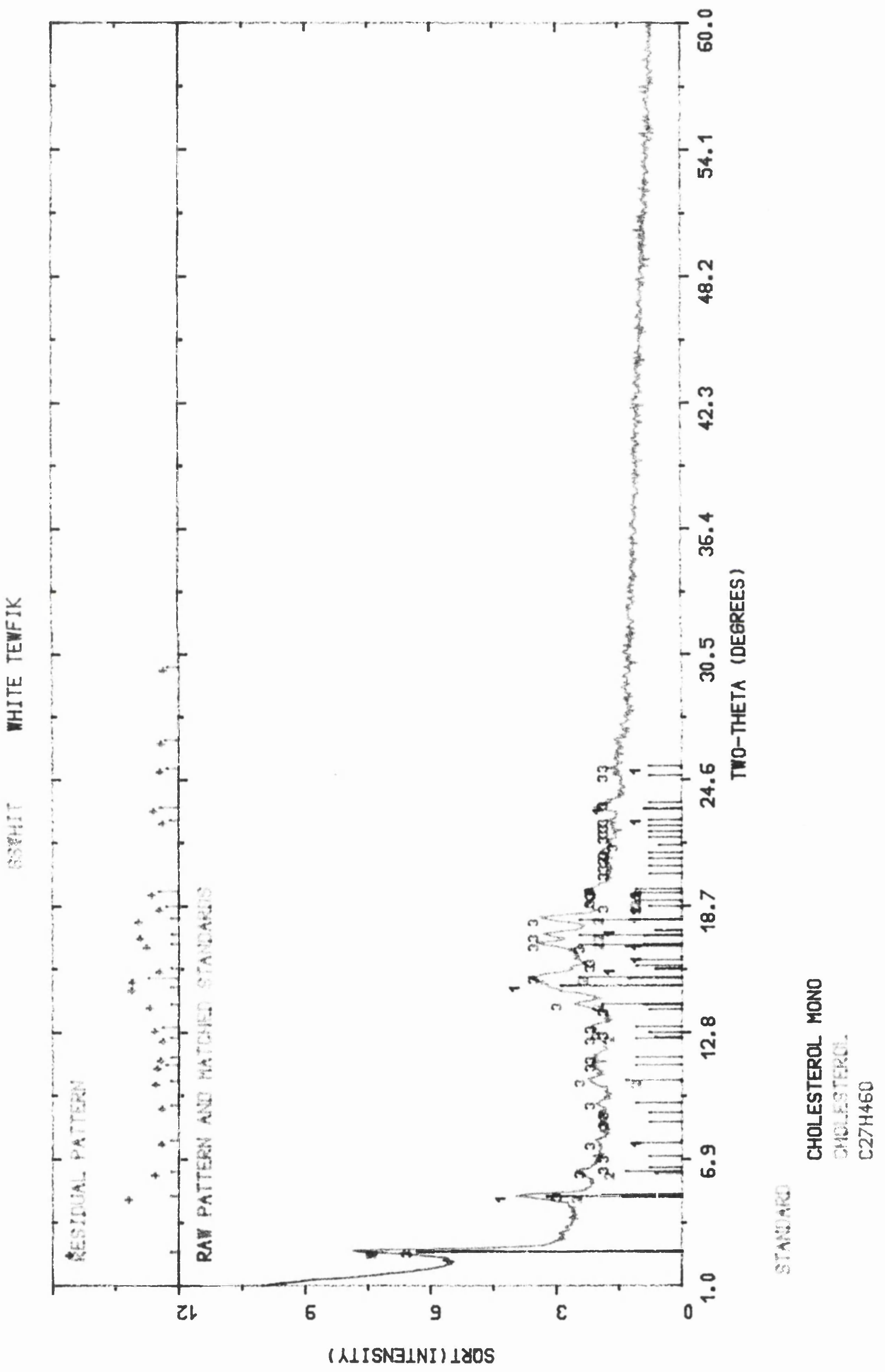

Figure 5.7 Gallstone g3

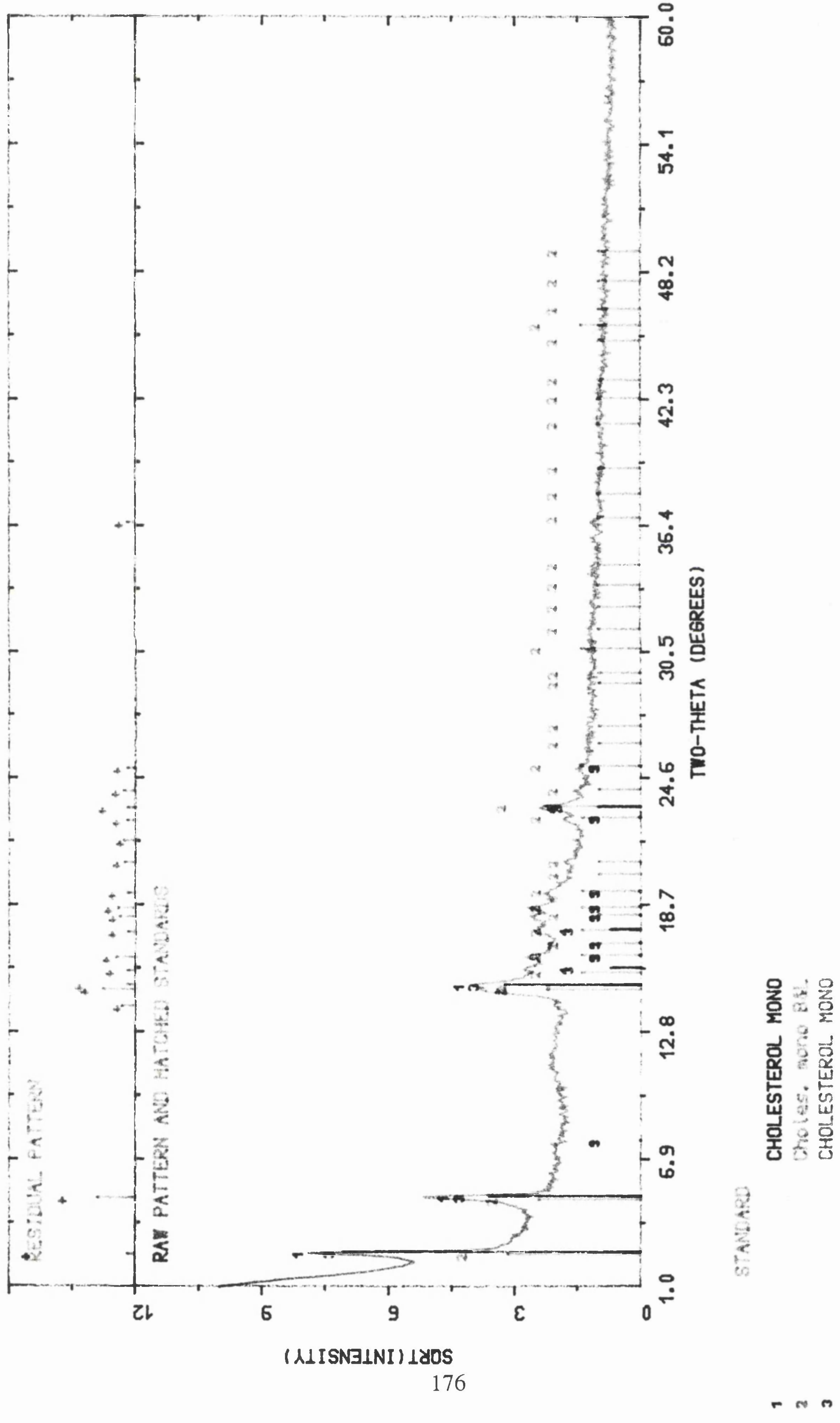

Figure 5.8 Gallstone g5

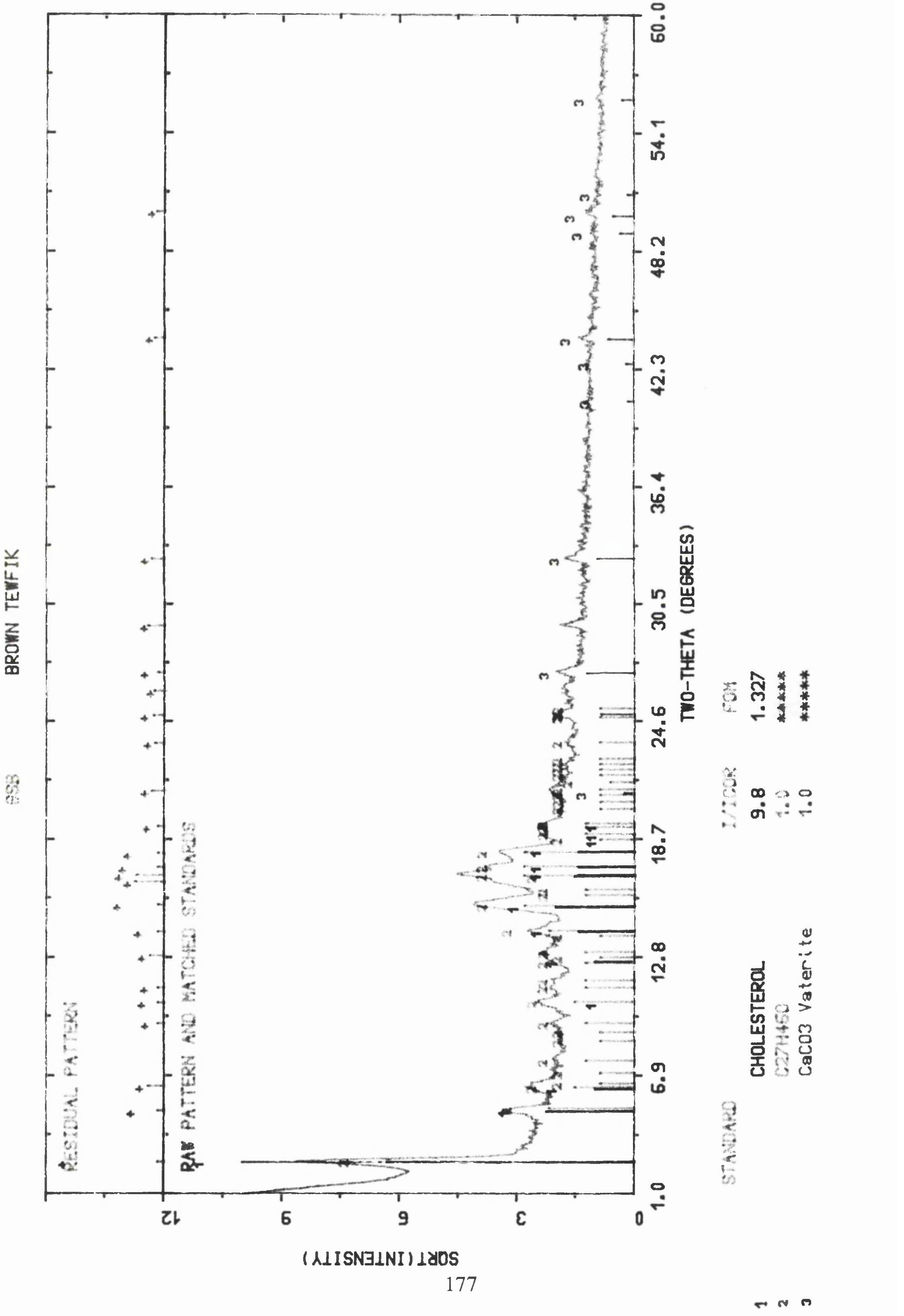

From the intensity of the diffraction patterns, a quantitative estimate of the relative amount of compound present in mixed samples such as g_5 is difficult. The increase in intensity of the lines can be either due to an increase of the quantity of the compound or due to preference in orientation of lattices. The preference in orientation of lattices of certain compounds cannot be entirely suppressed even with the use of the rotating sample stage. The resulting intensity in this case will give misleading information about the compound quantity. Furthermore, if the minimum compound quantity is not reached ($\sim$2%) it will not be registered by the x-ray diffraction analysis. For these reasons, and in order to evaluate the effective atomic number of the gallstones studied, another method has to be considered. From table 5.1, the gallstones g_1, g_2 and g_3 are composed of almost 100% cholesterol and so no further analysis is required. Gallstone g_5 contains two constituents of which one is calcium vaterite. If the amount of calcium could be determined, this would give a good approximation towards the calculation of the effective atomic number of g_5. For that reason the amount of calcium present was measured in both type of gallstones; the pigment stone g_5 and for comparison the cholesterol stone g_1. This was carried out using atomic absorption spectrometry within the department of Geology at University College London. Atomic absorption spectrometry is an analytical method for the determination of elements, based upon the absorption of radiation by free atoms. For quantitative analysis an atomic flame method is used where the sample is dissolved into water and a flame is used to produce an atomic vapour that contains free atoms of the element of interest.

Sixty mg of each gallstone sample was dissolved in hydrochloric acid and diluted in water after being heated to 700°C in a furnace to remove all organic compounds. The light source was provided by a calcium lamp that generates a sharp line spectrum of 422.7 nm which is characteristic of calcium, the desired element to be quantified. The radiation passes through a nitrous oxide flame into which the sample solution of gallstone is sprayed in a fine mist to produce free atoms. The resonance radiation line is isolated with a monochromator and detected by a Varian 475 atomic absorption spectrophotometer. The intensity of the resonance radiation line was measured with and without the sample passing into the flame. The difference between these readings gave a measure of the absorption and therefore of the amount of calcium element present in the sample. The results showed that g_5 contained 6.9% by weight of calcium and g_1 contained approximately 1%.

5.5 Comparison of Dual Energy Analysis with Crystallographic Methods

Dual energy analysis : A least square polynomial curve fitting of the atomic number Z versus the primary calculated A_1 with beam hardening correction (using the narrow beam geometry computer model) was undertaken for both the PHA and split detector methods. As a result of this fitting, the corresponding effective atomic numbers from the measured value of A_1 in figure 5.4 (corrected for beam hardening) were deduced taking into account the experimental error.

For crystallographic methods it was considered that g_1, g_2 and g_3 contain 100% cholesterol and that g_5 has a composition by weight of 93.1% cholesterol and 6.9% calcium. Their corresponding effective atomic numbers were then calculated according to equation 1.23.

The results for both methods are summarised in table 5.2.

For the split detector method a good agreement is shown between the results of the dual energy analysis and the crystallographic methods, within the experimental error. With the PHA method the effective atomic numbers for cholesterol stones are slightly lower than that predicted by x-ray diffraction technique which may be due to the fact that the full chemical composition of gallstones is not known.

Table 5.2 Comparison of Dual Energy Analysis with Crystallographic Methods

	gallstones			
Methods	g_1	g_2	g_3	g_5
PHA method	$3.5 \leq Z \leq 4.9$	$4.1 \leq Z \leq 5.6$	$3.8 \leq Z \leq 4.9$	$9.8 \leq Z \leq 10.2$
Split detector method	$4.6 \leq Z \leq 7.7$	$3.2 \leq Z \leq 6.8$	$3.9 \leq Z \leq 7.3$	$8.9 \leq Z \leq 10.0$
Combination of X-ray diffraction + atomic absorption spectrometry	$5.3 \leq Z^* \leq 5.7$	$5.3 \leq Z^* \leq 5.7$	$5.3 \leq Z^* \leq 5.7$	$6.7 \leq Z^* \leq 10.0$

As a conclusion, the dual energy analysis proved to be an efficient way of distinguishing between these types of gallstones. Although a relatively large error exists in the evaluation of A_1, and hence in the effective atomic number, the fact that a clear distinction is seen (taking into account the errors) between cholesterol and pigment stones makes the dual energy analysis a valuable method for gallstone identification. It provides not only a faster and cheaper way of gallstone analysis than the crystallographic methods but also the results can be obtained *in vivo* prior to treatment.

CHAPTER 6 CONCLUSIONS AND DISCUSSIONS

6.1 Dual Energy Procedures

The dual energy detectors employed in this study were capable of providing quantitative information about the chemical composition of the examined tissues. The dual energy measurements of A_1, the coefficient proportional to the material atomic number cubed, were obtained from a single projection and during a single exposure. Thus, the problems associated with patient movement are avoided and the dose given to the patient is minimised. These detectors are capable of real-time localised tissue characterization during a fluoroscopic procedure making them a valuable tool in a clinical environment where prompt results and quick decision making are essential. Furthermore, these detectors can be used in any radiology department where conventional diagnostic x-ray apparatus is available.

In chapter 2, the narrow beam geometry computer model was shown to be capable of selecting the optimum detector combination for the split detector probe by considering the absorption efficiencies of the two detectors and the dual energy sensitivity. This model was also successful in finding the required energy windows for the optimum PHA probe response.

The dual energy analysis was based on an assumption that the spectra absorbed by the two detectors in the case of the split detector probe or the absorbed spectra arising from the single PHA probe can be represented by two effective energies. The effect of beam hardening caused by introducing the material under investigation was considered to be small and, therefore, the dual energies were not assumed to be changed significantly. In practice, however, this is not the case and in order to tackle this problem an iterative correction procedure for beam hardening was developed using the computer model. This was achieved by making a preliminary estimate of the dual energy coefficients from a 'measurement'; these values were then used to compute the linear attenuation coefficient of the absorber. By comparing this result with the 'measured' values, the iterative correction leads to a convergent result for the dual energy coefficients A_1. Unlike other algorithms developed for beam hardening correction which require lengthy calibration measurements, the only requirement of this procedure was a knowledge of the incident spectrum. The iterative procedure was found to be very successful at correcting the variation in A_1 with patient thickness, especially for the PHA method. Although the variation in A_1 with the examined material thickness was considerably reduced, there was still a relatively significant variation for high atomic number materials (Z>13), especially for the split detector method. Thus in summary, from the computer model, unique experimental values of A_1, independent of patient thickness (10-20 cm) and material thickness (0.1-1 mm) were found for atomic numbers up to Z=22 for the split detector method with a precision of ~ 8% and up to Z=29 for the PHA method with a precision of ~ 3%.

Chapter 3 involved the construction of the split detector probe and the experimental evaluation of all three dual energy probes. The experimentally measured values of the dual energy coefficients A_1, although slightly lower, show similar behaviour to the theoretical values. The differences between the theoretical and experimental values were mainly due to the signal loss in the detectors and associated electronics which were not taken into account by the narrow beam geometry computer model. Using the split detector probe, the highest sensitivity for the experimental value of A_1 was obtained at 70 kVp. For the PHA probe, the highest sensitivity was obtained at 80 kVp due to the choice of energy window sets selected during the dual energy analysis.

The choice of a low kVp value is limited by the noise present in the system. A reduction in the x-ray tube operating voltage will cause a reduction in its intensity. Consequently, noise, and, hence, experimental standard deviation are increased. It was found that the probability of success in distinguishing between materials increases with higher kVps in the case of the split detector system. Therefore, a compromise between the largest sensitivity and probability of success has to be considered when choosing the incident spectrum. The final incident spectrum selected for the split detector was at 80 kVp. In case of the PHA probes, the probability of success shows a different result. The standard deviation, which includes not only the time variation of the x-ray tube but also any variation between subsequent exposures, seems to exceed the error due to the reduction of the intensity penetrating the patient. Thus, the best probability of success which was found at 70 kVp may occur because the x-ray tube output is more stable at lower kVps resulting in smaller experimental error.

The experimental errors associated with the values of A_2 were so large that any distinction between materials under investigation could not be made. This occurred because the variation in the Compton component of the attenuation coefficient, from which A_2 is derived, is smaller than that caused by the experimental error. Thus, the dual energy probes were limited to the determination of A_1 only. However, this coefficient would still provide valuable information about the effective atomic number of a lesion once it has been detected.

Out of the three dual energy probes considered, the PHA semiconductor probe proved to be the most effective in the accurate determination of A_1. This was mainly due to the better energy resolution of the solid state detector which enabled more accurate energy separation during dual energy procedures. The big advantage of the split detector probe was the speed of measurement which took on average less than 100 ms. Due to the experimental error, a limit of 1 mm in tissue thickness was imposed on the detection of low atomic number tissues ($Z \leq 13$). All dual energy probes showed potential for differentiating between materials of low atomic number exceeding 1 mm thickness.

6.2 Effects of Scattered Radiation

A Monte Carlo model was used to study the effects that scattered radiation have on the recorded signal of the dual energy coefficient A_1. The contribution of coherent scatter was included in the model since the collimation of the dual energy probes resulted in primarily forward scattered radiation being recorded. Recently, several authors have demonstrated that due to intermolecular interference the differential coherent scattering probability for liquid and solid materials was not peaked at zero degree scattering angle as suggested by atomic form factors. Therefore, data on the liquid or solid state form factors were required where possible to study the small angle behaviour of coherent scatter. The effect of scattered radiation increases the detected intensity in any dual energy procedure, making lesions or tissues under examination appear less attenuating than they actually are. This leads to an underestimation of the dual energy coefficient A_1. It was found that for the PHA method, the effect of scattered radiation was small for materials with low atomic numbers ($Z \leq 13$). However, for high atomic number materials, the computed value of A_1 depended on the way the form factors were calculated. Using the atomic form factors more coherent scattered radiation was detected by the Monte Carlo model resulting in a reduction of A_1. Due to the large proportion of scattered radiation detected by the split detector probe, the recorded value of A_1 was lower than the "free" scatter case and that from the PHA probe. However, due to the increase of the recorded Compton scattered radiation, the total scatter produced was independent of the way the form factors were evaluated. Thus, for the split detector method the requirement of molecular form factor data was not necessary. In general terms, the PHA method proved to be affected less by material and phantom thickness variation than the split detector method in the presence of scattered radiation. Also the effect that scattered radiation has on the recorded signal, A_1, was higher for high atomic number materials (Z=22 to 29) compared to low atomic number materials (Z=6 to 13). This occurs because of the decrease in the signal to noise ratio for increasing atomic number material.

The results from the Monte Carlo computer model for assessing the value of A_1 were compared to that obtained experimentally under similar conditions. Both experimental and Monte Carlo results showed acceptable agreement for the split detector method. Thus, the Monte Carlo model can be used to investigate scattered radiation during dual energy procedures.

From the Monte Carlo study, it was found that the amount of scattered radiation varied with the incident spectrum, the patient thickness, the thickness of the material under investigation and its position within the patient -phantom. Thus, the recorded value of A_1 was shown to be dependent upon the conditions of irradiation. To resolve this problem, the scattered radiation component should be removed from the recorded signal during a dual energy procedure. Two approaches are possible, (i) rejection of scattered radiation or (ii) correction of detected signals;

i) with the first approach, antiscatter grids, large air gaps and collimation of the incident x-ray beam after the patient can be used. Antiscatter grids can be placed between the patient and the dual energy probes to suppress scatter. However, antiscatter grids do not completely eliminate the scatter and have the problem of significantly attenuating the primary beam. A large air gap between the patient and dual energy probes can be used to allow the scatter to diverge from the primary beam and miss the detectors. However, since coherent scatter does not diverge as far from the primary beam as incoherent and multiple scatter, in particular at high energies, it is more difficult to remove from the recorded signal. It has been reported by Johns and Yaffe (1983) that the maximum coherent scattering probability of liquid water is at 11° for 20 keV and at 2° for 100 keV. Therefore, grids and large air gaps will be less effective in reducing coherent scatter than they will be in reducing other types of scatter. The use of a fan-beam line scanning system has been successfully implemented in a virtually scatter free dual energy imaging system (Brody *et al* 1981). This system would be impractical when using the dual energy probes. The positioning of the probes for tissue characterization requires a large area incident beam to visualise the region of interest in an image intensifier. One of the other possibilities of reducing scatter is to finely collimate the entrance window of the dual energy probes.

ii) Using the previous method for scatter rejection will inevitably attenuate the primary beam and, therefore, will decrease the sensitivity of the dual energy probes. An alternative approach is to estimate, by measurement, modelling or combination of the two, the scattered radiation and subtract it from the raw data to obtain the corrected recorded signal (Shaw and Plewes 1985). Measurement of scattered radiation can be carried out in the same manner as described in section 4.5, i.e. by subtracting the measurement of A_1 with large incident beam from the second measurement of A_1 with collimation of the incident beam before and after the patient. Other investigators have placed a small lead beam stop between the source and the object so as to determine the scatter component. This measurement of scatter is very unlikely to be successful in a routine clinical application. Correction factors for the scattered radiation could be determined by modelling. The Monte Carlo model can be used to obtain the factors that would correct the recorded signal using dual energy probes. These correction factors should be derived for a variety of conditions such as patient thickness, material tissue thickness, air gap distance and incident x-ray beam. They would be tabulated for each set of parameters and directly used to correct for scattered radiation in the dual energy coefficient A_1.

6.3 Gallstone Analysis

Both the split detector probe and the PHA semiconductor probe were capable of distinguishing between cholesterol and pigment stones and hence of tissue characterization. This information is extremely useful and has potential in the treatment of gallstone disease. Cholesterol stones can be dispersed by using drugs whereas pigment stones, in most cases, need surgery or lithotripsy.

For low effective atomic number materials, such as gallstone tissues, the errors in the measurement introduced by the effect of beam hardening and those introduced by the effect of scattered radiation were found to be low in comparison to the dual energy experimental errors. The only exception was for pigment stones (e.g. g_4 and g_5) when using the PHA semiconductor probe. In this case the values of A_1, measured with a large field incident beam, were slightly lower than the primary values. When the position of the same gallstone was changed within the patient the experimental values of A_1 were similar within the limits of the experimental error.

A larger sample of gallstones would be desirable to have a better understanding of the capability of the dual energy probes to distinguish between each of the different types of gallstones. If a gallstone type falls in the region between cholesterol and pigment types which cannot be identified by the dual energy probes, other methods can be used to provide additional information, such as radiography - most cholesterol stones are radiolucent. If the measured effective atomic number of such a gallstone is close to that of a well established cholesterol stone and radiography showed it to be radiolucent, it would be a good approximation to classify this type of gallstone as a cholesterol stone.

The capabilities of the dual energy probes in distinguishing between cholesterol and pigment stones were confirmed with x-ray diffraction analysis and absorption spectrometry methods, justifying our confidence in the use of these probes for tissue characterization.

In order to assess the application of this method *in vivo* some further points should be considered in order to take into account the practical difficulties that would be present in a clinical examination. First, accurate positioning of the probe would need to be achieved. This could be done by watching the movement of the dual energy probe across the patient's body on the TV monitor of the image intensifier system, such that both the probe and the region of interest are superimposed. Furthermore, as the majority of gallstones are radiolucent, contrast media such as iodine are sometimes needed in order to visualise them in the image intensifier. To identify the type of gallstone under investigation two x-ray paths must be considered. The first path will pass through the gallstone and the second path will pass through its immediate surrounding. Thus, the iodine will be present in both regions and the only difference between the two paths would be the tissue under examination. Also one of the major requirements of using this technique *in vivo* is the knowledge of the thickness of the gallstones. As most gallstones tend to be symmetrical round stones, an estimate of the thickness could be made by measuring the diameter of the stones visualised on the image intensifier. It should be noted that an accurate measurement of the material thickness is not necessary since the errors due to the beam hardening effect caused by low effective atomic number tissues, such as gallstones, are lower than the experimental errors. Finally, scattered radiation should be minimised. A fine collimator used at the opening window of the dual energy probe would effectively reduce this problem.

6.4 Future Work

A simple theoretical dual energy analysis was used during the dual energy procedures. In order to take into account the non-linear relationship between the integral of the linear attenuation coefficient and the absorber thickness, i.e. the beam hardening effect, an iterative correction procedure was adapted. Although this method was relatively successful it fails to eliminate the beam hardening effect entirely, especially in the case of high atomic numbers (Z>13). Other algorithms for beam hardening correction, such as the direct approximation method, are worthy of consideration.

The relatively large errors associated with experimental measurements are partly due to the x-ray output fluctuations, as the complete investigation during dual energy procedures takes at least several seconds. Immediate improvement in the performance of the x-ray tube could be achieved by the installation of a 'state of the art' high voltage generator such as the MG163D (Harding *et al* 1987) which stabilises both voltage and tube current to 0.2%. It might then be possible to analyse even thinner tissue samples.

The computer models set up for this work can be extended to investigate other imaging systems. The Monte Carlo model would be improved by the inclusion of the incoherent scattering function to the Klein-Nishina cross-section to take into account the effect of electron binding. The statistical uncertainty could be improved by increasing the number of incident photons. The model could be extended further to include the effect of scattered radiation within the dual energy probes, and to correct for energy resolution for the split detector probe and energy efficiency for the PHA probe.

The focus of this thesis was based upon the potential clinical application of dual energy probes to gallstone analysis. This technique may prove useful in, for example

i) application to lithotripsy of gallstones, i.e. find a correlation between the type of gallstone and the number of pulses needed for its fragmentation.

ii) the measurement of blood volume via contrast enhancement examination, i.e. if the material under investigation is known, its size can be determined since the dual energy coefficient A_1 of the material is dependent upon the material thickness (c.f. equation 1.42). Thus, any contrast enhanced examination could be used for volumetric or dimensional studies.

REFERENCES

Alvarez R.E. & Macovski A. *Phys.Med.Biol.* **21(2)**, 733, 1976.
"Energy-selective Reconstructions in X-ray Computerized Tomography".

Barnes G.T., Sones R.A., Tesic M.M., Morgan D.R. & Sanders J.N. *Radiology* **156**, 537, 1985.
"Detector for dual-energy digital radiography".

Birch R., Marshall M. & Ardran G.M. HPA *Scientific Report Series*-**30**, 1979.
"Catalogue of spectral data for diagnostic x-rays".

Brody W.R., Butt G., Hall A. & Macovski A. *Med.Phys.* **8(3)**, 353, 1981.
"A method for selective tissue and bone visualisation using dual energy scanned projection radiography".

Brooks R.A. & Di Chiro G. *Phys.Med.Biol.* **21(3)**, 1976.
"Beam hardening in x-ray reconstructive tomography".

Brooks R.A. *J.Comput.Assist.Tomogr.* **1**, 487, 1977.
"A quantitative Theory of the Hounsfiled Units and Its Application to Dual Energy Scanning".

Brooks R.A. *United states Patent* **no. 4,247,774** 1981.
"Simultaneous Dual-Energy Computer Assisted Tomography".

Cardinal H.N. & Fenster A. *Med.Phys.* **15(2)**, 167, 1988.
"Theoretical optimization of a split septaless xenon ionization detector for dual-energy chest radiography".

Cashwell E.D. & Everett C.J. *Pergamon Press*, New York, 1959.
"A practical Manual on the Monte Carlo method for Random Walk problems".

Chan H.P. & Doi K. *Phys.Med.Biol.* **28(2)**, 109, 1983.
"The validity of Monte Carlo simulation in studies of scattered radiation in diagnostic radiology".

Chan J., Alvarez R.E. & Macovski A. *IEEE Trans.Nuc.Sci.* NS **23(1)**, 1976.
"Measurement of soft tissue overlying bone utilizing broad band energy spectrum techniques".

Christ G. *Phys.Med.Biol.* **29(2)**, 1501, 1984.
"Exact treatment of the dual-energy method in CT using polyenergetic x-ray spectra".

Chuang K.S. & Huang H.K. *Med.Phys.* **14(2)**, 186, 1987.
"A fast dual-energy computational method using isotransmission lines and table lookup".

Chuang K.S. & Huang H.K. *Phys.Med.Biol.* **33(4)**, 455, 1988.
"Comparison of four dual energy image decomposition methods".

Edwin L. & Prien JR. *Year Book Medical Publishers*, Chicago, 1989.
"Biliary lithotripsy"

Evans R.D. *Mc Graw-Hill*, New York, 1955.
"The Atomic Nucleus".

Fenster A. *J.Comput.Assist.Tomogr.* **2(3)**, 1978.
"Split-xenon detector for tomochemistry in computed tomography".

Fraser R.G. et al *Radiology* **160**, 595, 1986.
"Calcification in Pulmonary Nodules: Detection with Dual-Energy DigitalRadiography".

Harding G., Kosanetzky J. & Neitzel U. *Med.Phys.* **14(4)**, 515, 1987.
"X-ray diffraction computed tomography".

Hawkes D.J. & Jackson D.F. *Phys.Med.Biol.* **25**, 1167, 1980.
"An Accurate parametrisation of the x-ray attenuation coefficient".

Hawkes D.J., Jackson D.F. & Parker R.P. *British.J.Radiol.* **59**, 537, 1986.
"Tissue analysis by dual-energy computed tomography".

Horrocks J.A. & Speller R.D. *Proc.Vth European Congress of Radiology*, 1983.
"Dual energy ionography for tissue characterisation".

Horrocks J.A. *PhD thesis*, Middlesex Hospital Medical School, University of London, 1987.
"The application of dual energy techniques to digital ionography".

Hubbell J.H. *NSRDS-NBS* **29**, 1969.
"Photons Cross-sections, Attenuation Coefficients and Energy Absorption Coefficients from 10 keV to 100 GeV".

Hubbell J.H. et al *J.Phys.Chem.Ref.Data* **4**, 471, 1975.
"Atomic Form Factors, Incoherent Scattering Functions, and Photon Scattering Cross Sections".

Jackson D.F. & Hawkes D.J. *Physics Reports (Physics Letters C)* **70**, 169, 1981.
"X-ray attenuation coefficients of elements and mixtures".

Jacobson B. *Acta Radiol.* **39**, 437, 1953.
"Dichromatic Absorption Radiography".

James R.W. *L.Bragg edition*, Bell, London, 1962.
"The Crystalline State.Vol.II. The Optical Principles of the Diffraction of X-rays".

Johns H.E., Bruce W.R. & Reid W.B. *British J.Radiol.* **31**, 254, 1958.
"The dependence of depth dose on focal skin distance".

Johns P.C. & Yaffe M.J. *Med.Phys.* **10(1)**, 40, 1983.
"Coherent scatter in diagnostic radiology".

Johns P.C., Drost D.J., Yaffe M.J. & Fenster A. *Med.Phys.* **12(3)**, 1985.
"Dual-energy mammography : Initial experimental results".

Kahn H. *RAND*, Santa Monica, CA, 1956.
"Applications of Monte Carlo".

Kalender W.A., Perman W.H., Vetter J.R. & Klotz E. *Med.Phys.* **13**, 1986.
"Evaluation of a prototype dual-energy computed tomographic apparatus".

Kelcz F., Joseph P.M. & Sadek K.H. *Med.Phys.* **6(5)**, 1979.
"Noise considerations in dual energy CT scanning".

Kosanetzky J., Knoerr B., Harding G. & Neitzel U. *Med.Phys.* **14(4)**, 526, 1987.
"X-ray diffraction measurements of some plastic materials and body tissues".

Kouris K., Spyrou N.M. & Jackson D.F. *Surrey University Press / Blackie & son*, Glascow, 1982.
"Imaging with ionizing radiations".

Lehmann L.A., Alvarez R.E., Macovski A. & Brody W.R. *Med.Phys.* **8(5)**, 659, 1981.
"Generalized image combinations in dual KVP digital radiography".

Morin L.R.M. & Berroir A. *Phys.Med.Biol.* **28(7)**, 789, 1983.
"Calculation of x-ray single scattering in diagnostic radiology".

Morin L.R.M. *J.Phys.Chem.Ref.Data* **11(4)**, 1091, 1982.
"Molecular Form Factors and Photon Coherent Scattering Cross Sections of Water".

Muntz E.P., Fewell T., Jennings R. & Bernstein H. *Med.Phys.* **10(6)**, 819, 1983.
"On the significance of very small angle scattered radiation to radiographic imaging at low energies".

Neitzel U., Kosanetzky J. & Harding G. *Phys.Med.Biol.* **30(2)**, 1289, 1985.
"Coherent scatter in radiographic imaging : a Monte Carlo simulation study".

Persliden J. & Carlsson G.A. *Med.Phys.* **13(1)**, 19, 1986.
"Calculation of the small-angle distribution of scattered photons in diagnostic radiology using a Monte Carlo collision density estimator".

Pickard M. *MSc Report*, Middlesex Hospital Medical School, University of London, 1982.
"An investigation into the information content of the scattered radiological beam".

Raeside D.E. *Phys.Med.Biol.* **21(2)**, 1976.
"Monte Carlo principles and applications".

Ritchings R.T. & Pullan B.R. *J.Comput.Assist.Tomogr.* **3(6)**, 842, 1979.
"A Technique for Simultaneous Dual Energy Scanning".

Romanes G.J. *Oxford University Press*, 1981.
"Cunningham's Textbook of Anatomy".

Ruckdeschel F.R. *Mac Graw-Hill Publications Co.*, New York, 1981.
"BASIC scientific subroutines vol.II".

Rutherford R.A., Pullan B.R. & Isherwood I. *Neuroradiology* **11**, 15, 1976.
"Measurement of effective atomic number and electron density using an EMI scanner".

Rutt B. & Fenster A. *J.Comput.Assist.Tomogr.* **4(4)**, 501, 1980.
"Split-filter Computed Tomography : A Simple Technique for Dual Energy Scanning".

Shaw C.G. & Plewes D.B. *Radiology* **157**, 247, 1985.
"Quantitative Digital Subtraction Angiography: Two Scanning Techniques for Correction of Scattered Radiation and Veiling Glare".

Speller R.D., Ensell G.J. & Wallis C. *British J.Radiol.* **58(688)**, 461, 1983.
"A system for dual energy radiography".

Storm E. & Israel I.H. *Nuclear Data Tables* **A7**, 565, 1970.
"Photon cross sections from 1 keV to 100 meV for elements Z=1 to Z=100".

Suttor D.J. & Wooley S.E. *Gut* **10**, 681, 1969.
"X-ray diffraction studies of the composition of gallstones from English and Australian patients".

Trotman B.W. et al *Gastroenterology* **72**, 495, 1977.
"Pigment versus cholesterol cholelithiasis : Identification and quantification by Infrared spectroscopy".

Vetter J.R. & Holden J.E. *Med.Phys.* **15(5)**, 726, 1988.
"Correction for scattered radiation and other background signals in dual-energy computed tomography material thickness measurements".

Vetter J.R., Perman W.H., Kalender W.A., Mazess R.B. & Holden J.E. *Med.Phys.* **13**, 340, 1986.
"Evaluation of a prototype dual-energy computed tomographic apparatus.II. Determination of vertebral bone mineral content".

Weissburger M.A., Zamenhof R.G., Aronow S. & Neer R.M.
J.Comput.Assist.Tomogr. **2**, 253, 1978.
"Computed Tomography Scanning for the Measurement of Bone Mineral in the Human Spine".

White D.R. *Phys.Med.Biol.* **22**, 219, 1977.
"An Analysis of the Z-dependence of Photon and Electron Interactions".

Williamson J.F. & Morin R.L. *Phys.Med.Biol.* **28(1)**, 57, 1983.
"An efficient method of randomly sampling the coherent angular scatter distribution".

Yang N.C., Leichner P.K. & Hawkins W.G. *Med.Phys.* **14(5)**, 759, 1987.
"Effective atomic numbers for low-energy total photon interactions in human tissues".

Zerby C.D. *Edition Alder B., Fernbach S. & Rotenburg M.*, New York, 1963.
"Methods of Computational Physics Vol.I".